University of Maribor

UNIVERSITY OF MARIBOR
FACULTY OF NATURAL SCIENCES AND MATHEMATICS

DOCTORAL THESIS

THE ANALYSIS OF CELL-BIOMATERIAL INTERACTION BY ADVANCED EXPERIMENTAL TECHNIQUES AS THE BASIS FOR BIOCOMPATIBILITY STUDIES OF POLYMERS

DOKTORSKA DISERTACIJA

RAZISKAVE INTERAKCIJ MED CELICAMI IN BIOPOLIMERNIMI MATERIALI Z NAPREDNIMI EKSPERIMENTALNIMI METODAMI KOT OSNOVA ZA ŠTUDIJ BIOKOMPATIBILNOSTI POLIMEROV

Rok Podlipec

Mentor: prof. dr. Janez Štrancar

Co-mentor: prof. dr. Gianluca Ciardelli

September, 2015

Table of contents

The analysis of cell-biomaterial interaction by advanced experimental techniques as the basis for biocompatibility studies of polymers

Abstract

The last two decades have been determined by the development in the field of tissue engineering. Beside the constant progress in new biomaterials and scaffold fabrication methods, currently the main focus is to understand scaffolds biocompatibility. Various cell responses to a wide range of different scaffolds properties are studied, like morphology, mechanical properties, physical surface properties and biochemical surface properties on a molecular scale. Due to the complexity of biomaterials composition as well as the cell response during the attachment and the following growth, many unresolved issues remain. In order to better understand the biological interface, new breakthroughs in the understanding of the of material-cell interaction are necessary.

In our thesis, physical aspects of scaffold biocompatibility were studied by correlating molecular to macro scale physical properties of scaffolds with cell attachment and cell growth. In order to focus on scaffold physical properties, scaffolds were prepared by the same chemical composition of natural polymer gelatin excluding biochemical effects on the cell response. Scaffold with different physical properties were obtained by changing the temperature, pH and crosslinker degree during the cryogelation and populated by the fibroblast cells. Advanced experimental biophysical methods were applied to determine the polymer mobility via electron paramagnetic resonance (EPR) with spin labelling, the scaffold mechanical properties via rheometry, dynamic mechanical analysis (DMA) and nanoindentation using atomic force microscope (AFM) and the scaffold porosity via confocal fluorescence microscopy (CFM). The anisotropy of the molecular mobility of the side chains of polymers in the crosslinked gelatin structure was found to correlate with the initial cell growth (throughout the first week) the best of all the physical properties measured. About five times less efficient cell growth was measured on the scaffolds with highly mobile, spatially nonrestricted dynamics of the polymer side chains, in comparison with cell growth on the scaffolds with the restricted rotational motion of polymers. The result indicates that cells identify and respond to the degree of polymer mobility, where partially immobile phase is necessary for efficient cell attachment and efficient cell growth. So far, the molecular mobility of polymers constituting tissue engineering materials has never been studied thoroughly with respect to its influence on cell response, and therefore may represent a new experimental approach in understanding biocompatibility.

To further understand cell-scaffold interaction, the study focused also on the first events during cell attachment - bond formation between the cell surface proteins and the specific binding sites on the material. Unfortunately, there are very few experimental analytical methods that enable accurate, real-time measurements of the individual molecular processes on the interface or adhesion dynamics of individual cells with good spatial and temporal resolution. The development of new methods and new concepts is definitely required.

In our thesis, cell adhesion dynamics was investigated in real-time on the surfaces of gelatin scaffolds with different physical properties using spatially-controlled cell

manipulation by the optical tweezers and the confocal fluorescence microscopy detection. Our goal was to elucidate, if the adhesion dynamics can be correlated with cell growth and if it can be dependent on the scaffold polymer molecular mobility.

Quantitative characterization of the optical tweezers force applied during cell-scaffold adhesion analysis was done by viscous drag force calibration and dynamic cell sequential trapping of individual cells. The maximal force on a trapped cell not causing the thermal damage was measured up to 200 pN, with nearly linearly increasing force profile across the cell towards the plasma membrane. By submicron spatial resolution of cell manipulation, we managed to quantify probability of cell adhesion, cell adhesion strength and mechanism of cell attachment, including the formation of the membrane tethers, which slow down the adhesion process. Adhesion strength was classified according to the displacement of the attached cell under the force of optical tweezers measured in the direction of the scaffold surface. At high strength, several tens or up to hundreds of binding sites were formed in the first seconds. Cell adhesion was shown to significantly correlate with cell growth in the first days of culture, while the adhesion itself seems to be dependent on the molecular mobility of surface polymers. The result indicates that the interactions during the first seconds may markedly direct further cell response. The developed methodology for cell adhesion analysis on the surfaces of 3D scaffolds serves as a good tool to forecast scaffold biocompatibility.

Raziskave interakcij med celicami in biopolimernimi materiali z naprednimi eksperimentalnimi metodami kot osnova za študij biokompatibilnosti polimerov

Povzetek

Obdobje zadnjih dvajsetih let zaznamuje velik napredek na področju raziskav tkivnoinženirskih nosilcev za uporabo v regenerativni medicini. Poleg raziskav novih biomaterialov in načinov priprave nosilcev se daje velik pomen razumevanju biokompatibilnosti. V literaturi najdemo mnogo študij vpliva različnih lastnosti nosilcev na različen odziv celic, med katerimi so najpogostejši, morfologija, mehanske lastnosti, in fizikalne ter biokemijske lastnosti na površini na molekularni skali. Zaradi kompleksnosti sestave nosilcev in kompleksnosti celičnega odziva tekom pritrjevanja in nadaljnje rasti pa obstaja še mnogo vprašanj odprtih. Da bi odgovorili na marsikatera med njimi so potrebna nova odkritja v razumevanju interakcije material-celica.

V doktorski študiji smo proučevali vplive različnih fizikalnih lastnosti polimernih nosilcev iz želatine na molekularni kot tudi makroskopski skali na pritrjevanje in rast celic. Biokemijski vpliv na odziv celic smo izločili z uporabo enake kemijske sestave pri pripravi nosilcev. Porozne nosilce z različnimi fizikalnimi lastnostmi smo uspeli pripraviti s spreminjanjem temperature, pH in stopnje premreženja tekom sočasnega zamrzovanja in premreževanja. Za karakterizacijo fizikalnih lastnosti smo uporabili napredne biofizikalne eksperimentalne metode: elektronsko paramagnetno resonanco (EPR) s spinskim označevanjem molekul za analizo molekularne mobilnosti stranskih verig polimerov, reometrijo, dinamično mehansko analizo (DMA) in nanoindentacijo z mikroskopom na atomsko silo (AFM) za analizo mehanskih lastnosti nosilcev na makroskopski in mikroskopski skali ter konfokalno fluorescenčno mikroskopijo (CFM) za analizo poroznosti nosilcev na mikroskopski skali. Ugotovili smo, da med merjenimi lastnostmi anizotropija molekularne mobilnosti stranskih verig polimerov v premreženi želatinski strukturi najbolj korelira z rastjo celic v prvih dneh. Izmerili smo približno petkrat slabšo rast celic na nosilcih z izrazito, neomejeno prostorsko mobilnostjo stranskih verig polimerov v primerjavi z rastjo celic na nosilcih z omejeno mobilnostjo le teh. Rezultat nakazuje na to, da celice prepoznajo in se odzovejo na stopnjo molekularne mobilnosti polimerov, kjer je za uspešno pritrditev in uspešno rast le teh potrebna delno nemobilna faza polimerov v sami strukturi. Te fizikalne lastnosti v dosedanjih raziskavah vpliva lastnosti tkivno inženirskih materialov na odziv celic še niso natančno raziskovali in bi lahko predstavljala nov eksperimentalni pristop za boljše razumevanje biokompatibilnosti.

Za nadaljnje razumevanje interakcije nosilec-celica, smo se v doktorski študiji posvetili analizi dinamike pritrjevanja celic − nastanek prvih vezi med celičnimi transmembranskimi proteini in specifičnimi ligandi na površini materiala. Na tem področju žal ne obstaja veliko eksperimentalnih analitičnih metod, s katerimi bi lahko v realnem času raziskovali posamezne molekularne dogodke na stiku ali dinamiko pritrjevanja posameznih celic z dobro prostorsko in časovno resolucijo. Potrebujemo razvoj novih metod in novih konceptov.

V doktorski študiji smo proučevali dinamiko pritrjevanja posameznih celic v realnem času na površinah želatinskih nosilcev z različnimi fizikalnimi lastnostmi s prostorsko nadzorovano manipulacijo celic s pomočjo optične pincete in detekcije s konfokalno fluorescenčno mikroskopijo. Želeli smo pojasniti ali dinamika pritrjevanja korelira z rastjo celic in ali na dinamiko lahko vpliva molekularna mobilnost polimerov.

Silo tekom analize pritrjevanja smo kvantitativno določili s predhodno umeritvijo z viskozno silo okoliške tekočine in umeritvijo s sekvenčno dinamično manipulacijo posameznih celic. Izmerjena največja sila optične pincete na celico pri kateri še nismo zaznali termične poškodbe je bila 200 pN, pri čemer sila pada v približku linearno iz lege pincete na robu celice radialno v smeri proti težišču, centru celice. S podmikronsko prostorsko ločljivostjo manipulacije celic na stiku s površino nosilca smo natančno določili verjetnost za pritrditev celic, moč pritrditve celic in mehanizme pritrditve celic, med katerimi je tudi takšen preko nastalih membranskih izrastkov, ki upočasni proces pritrjevanja. Moč pritrditve celic smo razvrstili glede na premik pritrjene celice v smeri tangencialno na površino nosilca pod vplivom sile optične pincete. Pri najmočnejših pritrditvah je nastalo več deset, tudi sto in več vezi v le nekaj sekundah stika. Pokazali smo, da dinamika pritrjevanja celic res korelira z rastjo celic v prvih dneh, medtem ko kaže, da je pritrjevanje res odvisno od molekularne mobilnosti polimerov na površini nosilca. Interakcije v prvih sekundah stika tako lahko zelo vplivajo oz. usmerjajo nadaljnji odziv celic. Razvito metoda analize pritrjevanja celic na površine 3D nosilcev lahko služi kot dobro orodje za določitev biokompatibilnosti nosilcev.

List of commonly used abbreviations

Chemicals and cells

3-Maleimido PROXYL	Spin probe, 3-Maleimido-2,2,5,5-tetramethyl-1-pyrrolidinyloxy
FITC	Fluorescent probe, fluorescein isothiocyanate isomer I
SPP 158	Membrane fluorescent probe
SPP 268	Environmental sensitive membrane fluorescent probe (2R,3S,4R,5R,6R)-2-(hidroxymethyl)-5-((7-nitrobenzo [c][1,2,5]oksadiazol-4-il)amino)-6-((1-tetradecyl-1H-1,2,3-triazol-4-il)metoxy)tetrahydro-2H-piran-3,4-diol)
PURs	Polyurethanes
L929	Mouse fibroblasts cell line

Experimental methods

EPR	Electron paramagnetic resonance
CFM	Confocal fluorescence microscopy
FMS	Fluorescence microspectroscopy
DMA	Dynamic mechanical analysis
AFM	Atomic force microscopy
OT	Optical tweezers

Physical quantities, constants and measured observables

T	Temperature
c	Concentration
(w/v)	Weight/volume
θ, φ	Cone angles of restricted rotational motion
Ω	Free rotational space
Ω_{AVG}	Average free rotational space
d	Weight of the spectral component
l	Scaffold wall thickness
d	Scaffold pore size
G'	Shear storage modulus
G''	Shear loss modulus
ν	Frequency
τ	Relaxation time
E_c'	Compressive storage modulus
E_c''	Compressive loss modulus
k	Cantilever spring constant
F	Force
E	Young's modulus
δ	Indentation distance
Δd	Cantilever deflection
Δz	Cantilever displacement
k_{trap}	Optical trap stiffness
β	Viscous drag coefficient
P	Optical tweezers power
x_i	Position of i-th object

$\Delta x_{i\text{-}j}$	Relative position of i-th and j-th object
v_i	Velocity of i-th object
A_{OT}	Optical tweezers sequence amplitude
N_{OT}	Number of trap sequence points
v_s	Optical tweezers switching frequency
F_{grad}	Gradient trapping force
r	Object radius
k_{on}	Cell attachment rate
k_{off}	Cell detachment rate
N	Number of cells
σ	Variance of the Gauss function
f	2D Gauss probability profile
λ_{max}	Probe spectral peak position
b	Probe photobleaching

1   Biomaterials and scaffold engineering

Tissue engineering in regenerative medicine (TERM), schematically presented in Figure 1.1, is relatively young research field with the first scientific report dating back in year 1995 (1), where it is described as "*the application of the principles and techniques of biomedical engineering to products and processes involving living cells*". Briefly, the research field comprises the development of advanced materials by high-end characterization methods and translation of the research from preclinical to clinical phases to meet diverse clinical applications (2). At the beginning, the transition of material development into clinical practise was depicted as the most challenging issue in this field of research (1), while currently the most challenging is the development of new and complex biomaterials (3) suitable for more and more specifically targeted clinical applications (2). One of them is scaffold engineering, the rapidly growing multidisciplinary field which incorporates the synthesis of biologically relevant materials and the production design, both essential for the cell-material interface (4).
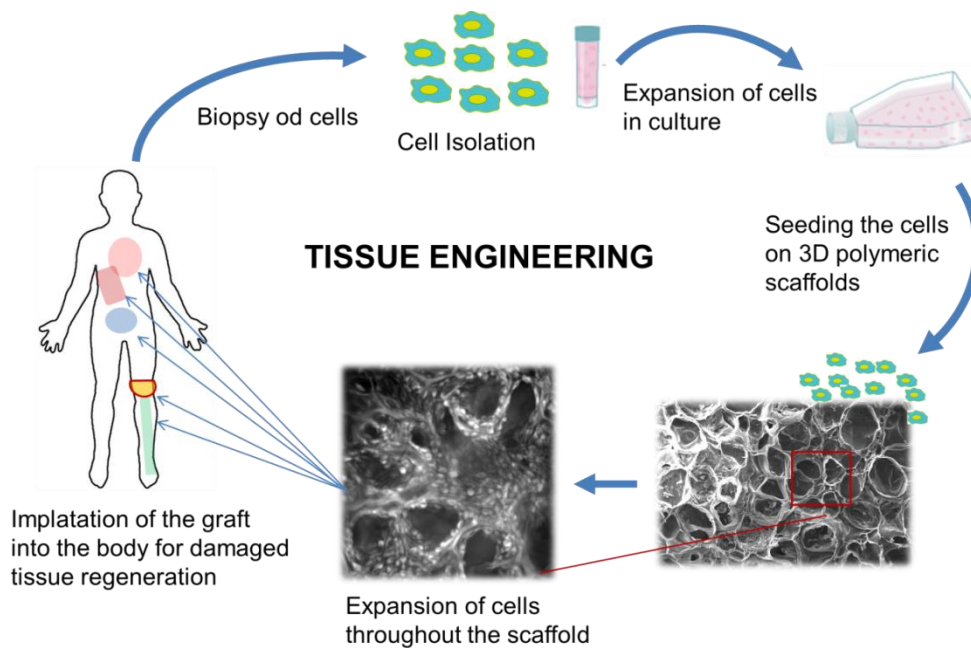
Figure 1.1. Basic principles of tissue engineering in regenerative medicine. Great attention is paid to the development of new complex scaffolds with adequate biocompatibility, biodegradability and mechanical performance.

There is a vast number of specifically designed and fabricated scaffolds for tissue engineering applications in regenerative medicine, which are composed of natural and synthetic polymers or even the combination of both (5). Most common natural polymers used are collagen, gelatin, alginate, chitosan, hyaluronic acid, agarose, silk and lately the mixture of polymers obtained by decellularization of tissues (6). These materials usually express higher biocompatibility once introduced into the body compared to synthetic ones but typically lack in stable mechanical properties, possess high structure variability and have

too fast biodegradation kinetics. Common synthetic materials with good mechanical tunability, controllable properties as well as biodegradability are polyesters, polyurethanes, polyanhydrides, polyphosphazenes, polycarbonates and polyethylene glycol (PEG) (7).

Very briefly, in order to achieve the maximum efficiency of biological scaffolds, these have to possess both structural and functional characteristics for proper remodelling of the tissue. Factors which strongly affect the final success and tissue function are:

- mechanical adequacy,
- porous, interconnected, highly diffusive structure,
- proper surface biochemistry and physical properties on the molecular scale,
- biodegradability dynamics,
- minimized inflammatory response, etc.

To control the structure, morphology and thus functionality of the fabricated 3D materials, various techniques have been implemented (8). One of the simplest and inexpensive methods presents solvent casting and particulate/porogen leaching technique, where the pores are created after solvent removal by evaporation (9). Another conventional well implemented methods are the phase separation technique, where the temperature change is needed to induce separation of different polymer phases (10) and freeze drying, where the solvent is removed by lyophilisation to acquire high porosity and interconnectivity (11). Among more sophisticated methods producing more controlled scaffolds structure are electrospinning technique, where the polymeric fibers of the sizes from nanoscale to microscale are produced by electrostatic force (12) and rapid prototyping, where 3D porous structure can be produced layer-by-layer by selective laser sintering, 3D printing, photo-polymerization, etc. (13). With the rapid prototyping, so-called computer-aided design approach, specific tissue directed scaffolds can be fabricated by accurate control of its architecture and topography to precisely regulate specific cell behaviour (14,15). Mixing different polymer materials and crosslinking techniques is another currently implemented practise, producing scaffolds with extreme functionalities to meet variety of applications (16,17). However, the best approximation of native mechanical and biological properties are obtained by scaffold fabrication through decellularization process of the tissues (6,18), where the preserved extracellular matrix (ECM) provides the native compositional and structural environment, crucial for cell recognition and tissue formation, but even with this procedure many significant challenges remain (19).

1.1 Biocompatibility issues of 3D scaffolds

The need for chemical and biological inertness of implanted materials in the co-existence with the tissue has become essential throughout the last years of the development. Due to the increased number of applications and the need for more efficient and specific-site focused treatments, materials were optimized for inducing specific chemical and biological activity on the tissue interface. In order to improve materials, an accurate understanding of the interface has thus become extremely important and new concepts of biocompatibility have been evolved (20). To understand and increase material biocompatibility, biochemical,

physiological as well as physical mechanisms have to be taken into consideration, which however still presents the major issue.

Scaffold design can limit either the sufficient porosity which can restrict the perfusion. i.e. oxygen or nutrients supply into the scaffold once introduced into the tissue (21,22) or sufficient tissue formation while achieving adequately porous tissue networks (22), where concentration gradients of various types of proteins across 3D structure can significantly impact cell behaviour (23). Poorly controlled cell seeding combined with lack of cell infiltration/administration into the structure represent another problem which can reasonably limit successful implementation of a number of scaffold designs, essentially calling for modifications (24). However, the crucial limitation or more precisely the key issue regarding all scaffold designs is unpredictable biocompatibility, which should be given the highest attention, especially due to the increased complexity of fabricated scaffolds (4).

What makes biocompatibility so elusive is its origin in a complexity of cell-biomaterial interaction (25). Its convoluted nature imposes extensive preclinical functionality testing (26), that needs to simulate diverse conditions and elucidate not only the "first contact" response but also its time evolution through tissue regeneration and biomaterial degradation (27), which altogether features the importance of the material and tissue contact duration (28). With the additional requirement of minimazing the inflammatory response after implantation of biomaterials in the body (29) and the need for their rational cost-effective design (30), the development is currently focused on mimicking the properties of the native ECM to promote a relevant physiological environment (31,32). Such a bionic way has successfully resulted in the composition and functionalization of various scaffold matrices through identification of the essential molecular ECM compounds (33). Although many aspects of cell-biomaterial interaction have been identified (34–36), the puzzle of their rational control is still unresolved. Currently, the majority of preclinical biocompatibility testing of scaffolds, composed from variety of synthetic and natural polymers, focuses on cell responses to the substrate, from cell adhesion, proliferation, migration, differentiation, to ECM secretion. The search for crucial parameters modulating such cell responses is organized in three directions (Figure 1): *scaffold morphology* by evaluation of the pore size (37–42) and interconnectivity (43–45), essential for cell promotion and nutrition transport; *scaffold mechanical properties* by evaluation of the influence of stiffness, viscoelasticity and physical stimulation (46–53), essential for cell focal adhesion, communication, shape and motility as well as material degradation dynamics; and *scaffold properties on the molecular level* by evaluation of the effect of surface chemistry, energy, topography and specificity (54–60), essential for the cell-scaffold contact.
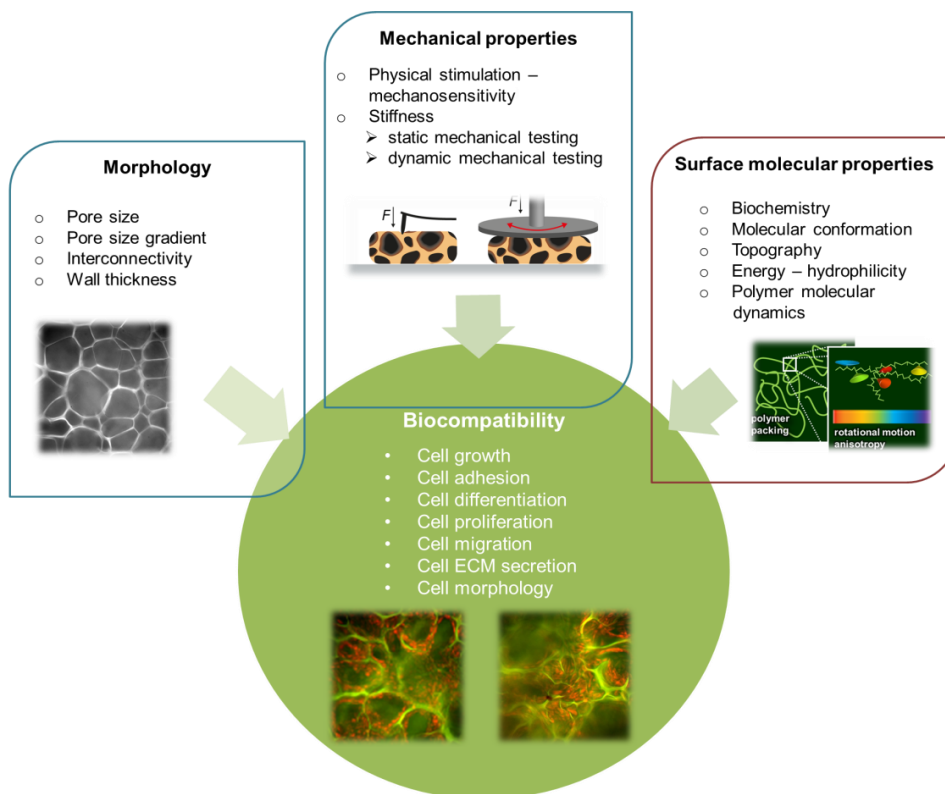
Figure 1.2. Schematic overview of the scaffold properties investigated to resolve biocompatibility. Commonly, macroscopic scaffold physical properties such as morphology and mechanical properties have been investigated, while recently great attention has been dedicated to characterize the influence of surface molecular properties. In our study, combination of properties with special focus on molecular mobility was studied and correlated with cell growth in order to get more insight into the complex nature of biocompatibility.

Despite constant improvements, biocompatibility of particular material with selected cell line or tissue cannot be predicted due to lack of generalized picture of cell response to various materials, precluding the production of tailor-made scaffolds (61). Traditionally, each scaffold property is correlated by specific cell response in a statistical way or a trial-and-error approach (Figure 1), missing the correlation between different material properties and cell responses and, even more importantly, scattering the investigation focus away from the actual mechanisms of biocompatibility. In order to improve this commonly established concept, new strategies are developed, one of which is presented in our thesis.

2   Cell-material interface

When studying and developing tissue engineering materials, one of the most important aspects is the understanding of the cell response once brought into the contact with the material surface. Proper response is shown through the adequate cell proliferation, migration, gene expression and minimized inflammatory response once introduced into the body, all of which depend on the processes on the interface starting from initial adhesion.

2.1 Biology of cell attachment

Cell attachment to tissue engineered scaffolds is primarily done through integrin molecules spanned on the cell surface (Figure 2.1). They consist of cell adhesion receptors denoted with α and β subunits (62), which in different combinations specifically bind to various ECM components and analogous scaffold materials (63). Recent structural, biophysical and biochemical studies of the mechanisms of integrin-ligand binding have (further) shown the importance of conformational regulation and changes of the binding complex (64). Integrins play an important role in controlling various steps in cell downstream signalling pathways, acquired across the plasma membrane, through cytoskeletal linkages and further transduction processes inside the cell with cytoplasmic components (62). These signalling pathways regulate processes such as proliferation, migration, differentiation and survival of cell, which can result in efficient tissue growth and remodelling. Integrin mediated cellular processes are mainly done through the so called focal adhesions complexes – large clusters of proteins in the plasma membrane with the structural and transduction function – which bind to actin filaments (Figure 2.1). These complexes recognize biochemical diversity of the extracellular space as well as its physical and topographical characteristics, which induces different mechanisms of environmental sensing (65). These focal assemblies are regulated by focal adhesion kinase (FAK) proteins (66), which can act as a cell mechanosensing agents during cell migration (67).
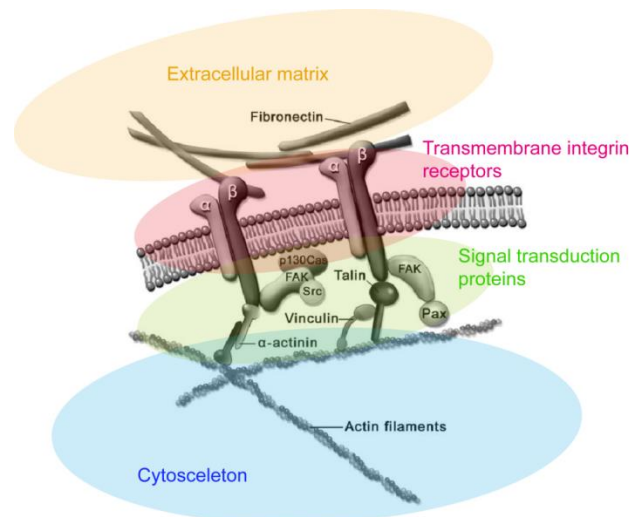
Figure 2.1. Scheme of proteins actively involved in cell interaction with the extracellular matrix (ECM) or analogous tissue engineering materials. Proteins are extracellular (orange; fibronectin as the most common ECM protein), transcellular (red; α and β subunits) and intracellular (green and blue; talin, vinculin, actinin, actin, etc.). Scheme is adapted from (68).

2.2 Exploring cell-material interaction

One approach to investigate material-tissue or material-cell interface is to study their interaction, starting from the initial cell response after the first contact up to the stage where proliferation, migration and possibly differentiation accompanied with secretion of ECM components had already been introduced into the system. However, the majority of the studies are being focused to material-cell interaction by exploring the response of the cells with already established focal complexes between membrane integrins and specific ligands on biomaterial site (63). These studies comprise investigation of specific cell dynamics during and after establishing focal adhesions (69,70), exploring the signalling processes governed by mechanotransduction (71), or revealing specific gene expression and differentiation. On the other hand, the intrinsic material-cell interaction that is expected to be reflected and exposed during the initial contact with first molecular events can be modulated by the cell-secreted components that can mask the real material properties making the choice of the experimental detection even more important.

2.2.1 Methods for the initial adhesion dynamics characterization

Quick review through the literature reveals that material-cell interaction is commonly investigated by cell counting assays applied hours after most likely occurring adhesion (72–74). To study the mechanics of the initial attachment, few methods with different force and time detection range have been implemented (Figure 2.2). Among them, spinning disk technique (75) and microfabricated post array detection (76) enable force measurement of cell adhesion up to hundreds of nanonewtons, while micropipette aspiration technique (77) and centrifugation assay (78) up to hundreds of piconewtons. However, in all the described

methods, the adhesion is studied minutes to hours after initial cell-material contact, thus unable to identify the first molecular events responsible for further strong integrin-based adhesion. Furthermore, the above experimental setups lack a direct efficient probing of cell-substrate interface, which makes the interpretation of the behaviour of cell on the interface even more difficult. To address this issue, two advanced methods, Single-Cell Force Spectroscopy (SCFS) using AFM (79) and Optical Tweezers (OT) (80) have been successfully implemented allowing accurate investigation of the adhesion dynamics of single cells in the first seconds to minutes time scale after the initial contact with approximate piconewton accuracy (81,82). For the detection of single molecular events at the very beginning of the contact, new methods have recently been developed, tension gauge tether (TGT) approach to measure single integrin-ligand bonds (83) and molecular tension-based fluorescence microscopy (MTFM) to measure pN-forces exerted by cell surface receptors (84). Due to the force resolution of less than piconewton (85,86) with its range highly relevant for biological systems (87) and particularly the ability of 3D manipulation of cells with independent 2D and 3D control (88), accompanied with easier handling and visualization of the investigated systems, OT is considered favourable over SCFS and the latter single molecular detection methods. However, physical principles of OT reviewed in (89) limit force detection range to maximum few hundred of pN which can balance only about few hundred of H bonds. OT is commonly combined with an imaging techniques such as fluorescence microscopy (90–92), convenient to investigate complex cell-material (93) or cell-cell adhesions (94).
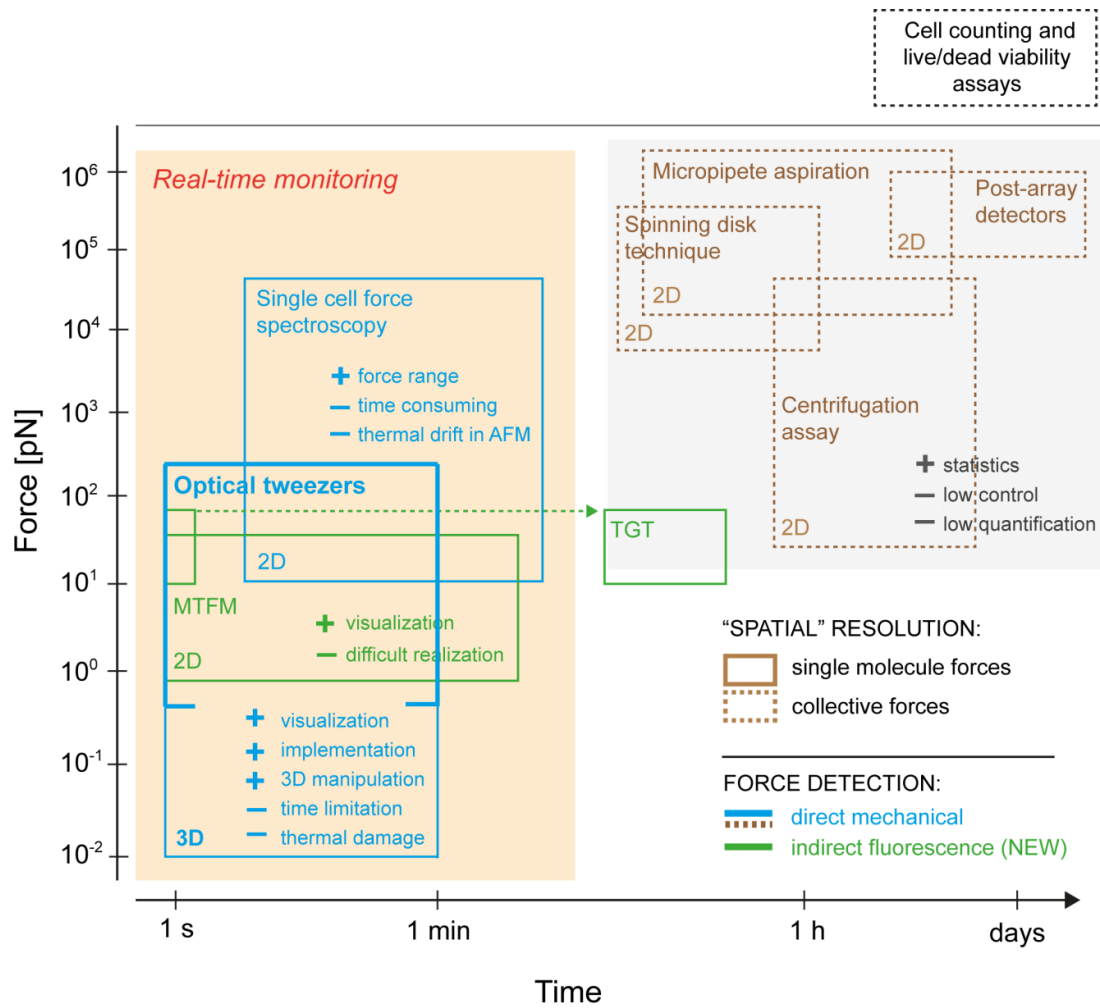
Figure 2.2. Comparison of cell adhesion characterization techniques, which vary in force resolution, time of acquisition and spatial resolution. Among the methods, optical tweezers were chosen in our research since they enable real-time cell monitoring, high force sensitivity (down to 1 pN in our system, denoted with thickened blue line) and 3D manipulation.

3   PhD thesis objectives

Our research was divided into two interrelated studies, both focused on the interaction between tissue engineered scaffolds and cells. The first goal was to study the aspects of scaffold biocompatibility by introducing new concepts of scaffold physical characterization and their correlation with cell response since the lack of the comprehensive studies done in this research field. To focus just on scaffold physical properties, the aim was to prepare scaffolds with the same chemical structure and different physical properties by accurately tuning the preparation parameters. The second goal was to study the dynamics of cell-scaffold adhesion in real-time to better understand the initial cell response by introducing new concepts of characterization. Very few methods with different force and time detection range have been implemented so far. Now, we explain the objectives in more details.

3.1 First objective

There are many studies which show correlations between the specific scaffolds property and the specific cell response (see the section 1.1.), but don't question whether this is the only property, which dictates cell response. One property usually correlated with cell response is scaffold mechanics, where different mechanical quantities are measured, from the compression modulus (47), shear storage modulus G' (50,95) to the Young's modulus E (96,97). The reason for such a diversity of implemented methods can originate from the fact that it is challenging to determine which material property cells actually feel throughout the process of attachment and spreading across the surface and thus any methodology is justifiably used. One of our first goals was hence to better understand how different scaffold mechanical quantities characterized by different characterization methods impact cell growth, if at all. By *rheometry*, shear storage modulus G' was measured, by *dynamic mechanical analysis*, compression storage modulus was measured E' and by *AFM nanoindentation*, the Young's modulus was measured.

Mechanical properties are not the only properties which are commonly measured and correlated with cell response. Scaffold surface molecular properties such as are surface biochemistry, topography, hydrophilicity, molecular conformations, etc. can strongly dictate cell response (see the section 1.1.). One of the biophysical properties which we believe it should be thoroughly investigated with respect to cell response and which was already noted in the literature (20) but never studied before, is the molecular mobility of the polymers composing the scaffold structure. The big question is how this molecular property effects initial cell response once it is introduced onto the scaffold surface? Our goal was thus to apply *electron paramagnetic resonance spectroscopy*, a common technique to measure motional patterns of the proteins and lipids in the biological membranes (98–100), to characterize the motional patterns of polymers in the intact scaffold structure and finally to search for the potential correlation with cell response.

Beside the mechanical and molecular characterization of scaffolds, the objective was to characterize also the scaffolds' morphological and structural properties by *confocal fluorescence*

microscopy, adsorption of serum proteins on scaffold surface by *UV-VIS absorption spectroscopy* and the dynamics of scaffold degradation by *enzymatic degradation analysis*. The results of the latter two methods are not shown in the thesis.

3.2 Second objective

Understanding of cell adhesion processes onto the scaffold surfaces from the very first recognition events is of crucial importance in the field of tissue engineering and regenerative medicine. Different techniques with different spatial, time and force resolution have been implemented so far (see the Figure 2.2) with new advanced techniques being developed lately, particularly to study single molecular events of single cells at adhesion site in real-time (83–84). There are still many questions how adhesion events are triggered and how adhesion dynamics influence further cell response such as cell signalling and more general, cell growth across the scaffold surface. To investigate these processes in real-time, special techniques with appropriate setup have to be employed.

The objective of second part of the study was thus to implement *near-infrared optical tweezers* combined with *CFM* to measure cell-scaffold adhesion dynamics and binding forces in real-time in 3D and search for the possible correlations with the initial cell growth throughout the scaffold surface. Briefly, the optical tweezers were used to enable cell manipulation with few tens of nm resolution in 2D and *z*-stage sub-micron position control in 3D in order to accurately measure their adhesion once introduced onto the scaffold surface. To characterize binding forces, the aim was to perform precise force calibration on cells and optionally on model systems such as are micron-sized beads. CFM detection was considered the most suitable for the visualization and further analysis of the cell-scaffold interface. The goal was thus to properly label the cells and scaffolds with fluorescent probes prior the experiment.

Another big question is how the local physical properties in the plasma membrane at the interface change during the adhesion and how this could be effectively measured in real-time? The idea was to apply *fluorescence microspectroscopy* (*FMS*) (101), developed in our laboratory, to detect possible local plasma membrane changes at the scaffold interface determined through the spectral analysis of plasma-membrane-labelled environmentally sensitive fluorescent probes (102).

4 Scaffold preparation

4.1 Materials

Gelatin type B (Sigma-Aldrich) derived from lime cured bovine skin with isoelectric point of 4.7-5.2, bloom number of 225 and the average molecular weight of 47 kDa was used as a scaffold material. Phosphate and carbonate buffers were used as a scaffold solutions and were prepared from sodium phosphate monobasic dihydrate, sodium phosphate dibasic heptahydrate, sodium carbonate and sodium bicarbonate, all purchased from Sigma-Aldrich. 1-ethyl-3(3-dimethylaminopropyl)-1-carbodiimide hydrochloride (EDC; Carbosynth) and N-hydroxysuccinimide (NHS; Sigma-Aldrich) were used to crosslink gelatin amino-acids during the scaffold preparation. Fluorescein isothiocyanate isomer I (FITC; Invitrogen) and 3-maleimido PROXYL (Sigma-Aldrich) (Figure 4.1) were further used as a fluorescent and spin probes, respectively, to label the side chains of gelatin polymers. L929 mouse fibroblasts were purchased from tissue engineering company Educell d.o.o. (Ljubljana, Slovenia). Fatty acid membrane fluorescent probes SPP158 and SPP268 (Figure 4.1), synthesized by co-worker dr. Stane Pajk at the Faculty of Pharmacy (University of Ljubljana, Slovenia), were used to label the cell membrane.
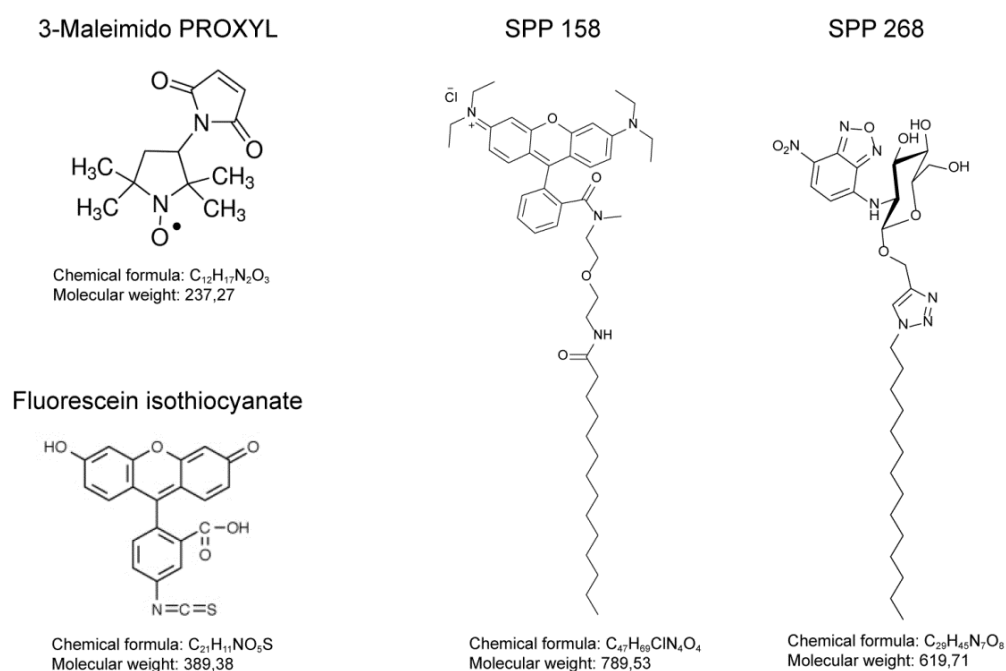

Figure 4.1. Chemical structure of the molecules used to label scaffolds' polymer side chains and grown cells. Chemical structures of 3-Maleimido PROXYL and Fluorescein isothiocyante are adapted from producer datasheet.

4.2 Gelatin scaffolds preparation

Scaffolds were prepared from 10% (w/v) gelatin solution at different pH: a) pH 7.5 obtained with phosphate buffer and b) pH 9.5 obtained with carbonate-bicarbonate buffer, both of concentration $c = 0.1$ M. The solutions were first let to swell under gentle stirring at room temperature and then heated up to the temperature of 50°C to overcome macroscopic gel-sol (microscopic helix-coil) transition to completely suppress gelatine chain helicity (103), enabling more efficient crosslinking and labelling by increasing accessibility of the primarily lysine sites. Randomly coiled gelatine polymers were then successfully functionalized by site-directed labelling mainly toward primary amine groups for further scaffold analysis. Fluorescent probe FITC (reactive via isothiocynate group (104)) and spin probe 3-maleimido PROXYL (reactive via maleimido group (105)) were used in a molar ratio of 1:2000 to the predetermined number of the available free amino groups, with more than 95% of ε-amines and less than 5% of α-amines, the number estimated by lysine concentration and the average molecular weight of gelatin chains. The chosen molar ratio enabled good detection of FITC fluorescent signal by fluorescence microscopy as well as good signal to noise ratio (S/N) of acquired electron paramagnetic resonance (EPR) spectra, while keeping the sample practically unchanged due to low percentage of labelled chains. Crosslinking of functionalized gelatin polymers was done by water soluble EDC and NHS in the molar ratio of 4:1 to produce stable amide bonds. Different concentrations with respect to gelatin free amine groups and different buffer pH were used to produce scaffolds with variable properties. The crosslinkers solution ($V = 0.7$ ml) was mixed with prewarmed gelatin solution ($T = 40$°C, $V = 6$ ml) and poured into Teflon petri dishes with diameter $d = 50$ mm, placed on the temperature-controlled plate schematically presented in Figure 4.2a. To accurately control crosslinking process, the experiment was optimized during the study, where the solutions were mixed just prior dosing on the cooled plate by syringe pump injection system. By temperature regulated crosslinking process during freezing-thawing process, the so-called cryogelation (106), stable scaffold were fabricated. Thawing cycle was performed between -10°C and 0°C in the time interval of 10 hours. The formed ice-templated, porous scaffolds were dialysed against the appropriate buffer to remove the excess of non-reacted crosslinkers and labelling probes. Scaffolds were sterilized with 70% ethanol solution for 2 hours and laminar UV light exposure for 30 min. Samples were dialyzed three times with sterile PBS to remove all excess ethanol and then stored at $T = 4$°C until characterization and cell interaction experiments. Scaffolds of the disk shape are depicted in Figure 4.3b.
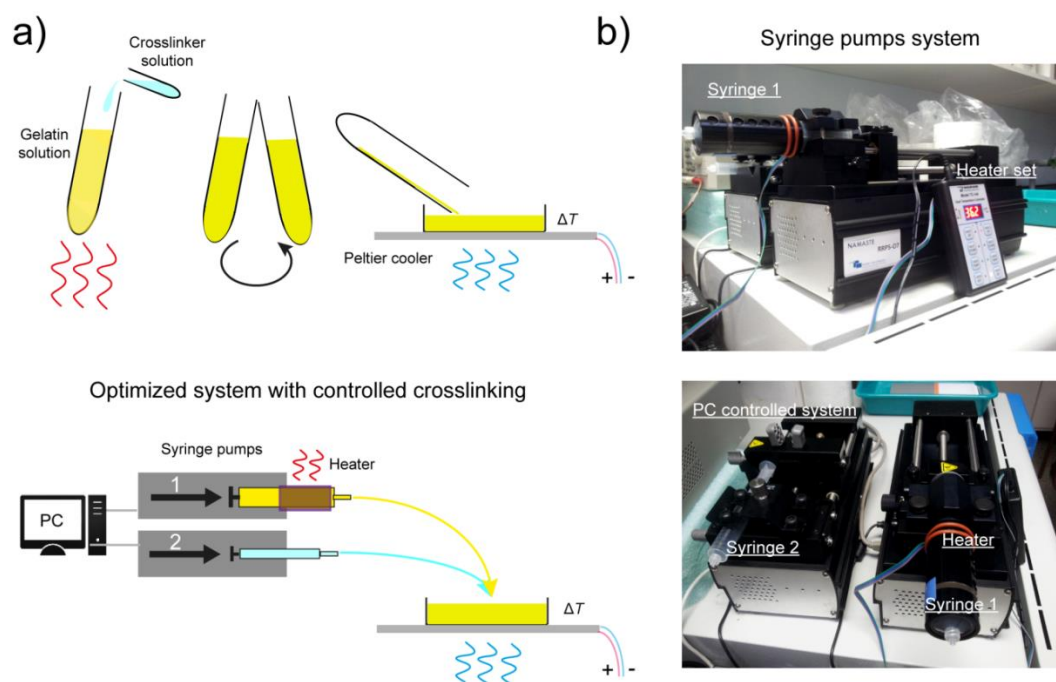
Figure 4.2. Fabrication protocol for gelatin scaffolds (a) with syringe pump injection system setup (b). First, crosslinker solution was mixed with prewarmed gelatin solution prior the cooling process. For an accurate control of the crosslinking process and thus the characteristics of final scaffolds, syringe pump injection system of the compunds was used.

4.3 Polyurethane scaffolds preparation

Polyurethane (PUR) porous scaffolds were fabricated by temperature induced phase separation (TIPS) method and subsequent solvent extraction (107). Briefly, PUR fabricated from polycaprolactone (PCL) diol, 1,4-butane diisocyanate and L-lysine ethyl ester dihydrochloride as described in (108), was first dissolved at $T = 60°C$ in dimethyl sulfoxide (DMSO; Sigma Aldrich) at 10% (w/v). The obtained solution was poured in a stainless steel parallelepiped mold (app. $50 \times 25 \times 30$ mm^3) and cooled down at $T = -20°C$ for 5 h. Quenching, performed by a rapid cooling with gradient temperature across on dimension induced DMSO crystal growth in specific direction, that is pore formation in a preferred direction. To extract the DMSO, the frozen scaffold was placed for seven days in a water/ethanol solution (30/70 v/v) refreshed twice a day. The scaffold was freeze-dried (Martin Christ ALPHA 2–4 LSC) and cut to obtain matrices with a thickness of about 1 mm (Figure 4.3a). Due to poor hydrophilic properties, which were measured by contact angle method (KSV INSTRUMENT CAM 2000) and poor surface chemistry, non-appropriate for the efficient cell adhesion and growth, scaffolds were modified by surface graft polymerization using plasma treatment (Plasma System Junior SN 001/072). Argon activation was first carried out to produce active radicals on material surface. Gas pressure in the instrument chamber was set to 0.5 Torr and the treatment was done for 60s at power 200 W. The samples were then exposed to the atmospheric pressure plasma treatment for 10 min and last, grafted with acrylic acid (-COOH) through radical copolymerization initiated by surface peroxides generated by second atmospheric treatment. Acrylic acid treatment was

done for 10 min and 20 min at power 100W. Samples were washed with distilled water to remove any unreacted monomer.

For better biocompatibility, surface of the samples was functionalized with proteins (gelatin Type B) through the formation of amide bonds between COOH groups on the surface and NH2 groups on proteins site. EDC and NHS were used as zero-length activators for chemical reaction, which was done at pH 5 and at pH 8.5 for the final covalent binding.
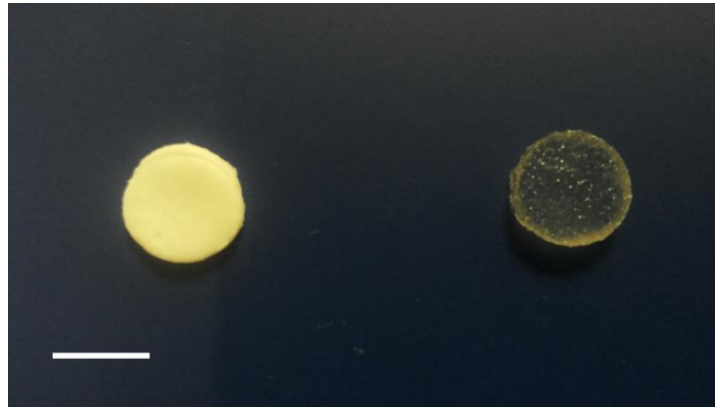

Figure 4.3. Polyurethane scaffold sample (left) and gelaitn scaffold sample (right). Shown dimensions were used for mechanical as well as cell growth analysis. The scale bar represents 1 cm.

5 Scaffold characterization

5.1 Polymer side chain mobility analysis by EPR spectroscopy

Site-directed spin labelling (SDSL) with 3-maleimide PROXYL on the gelatin primary amines and on traces of cysteine thiol groups was performed before scaffold preparation to elucidate the side chain conformational dynamics of polymers through EPR spectral lineshape analysis, as described before (109,110). Since spin probe size is similar to that of the protein side chain and much smaller than polymer itself, there is no significant influence of the probe on the polymer motion. Consequently, spin probe rotational motion basically reflects available space for side chain wobbling which is in addition superimposed on the polymer motion. If protein/polymer backbone is folded then backbone motion is slow and the anisotropy of the spin probe fast conformational motion characterizes the packing of the local protein side chains. These principally depend on the protein secondary structure and packing of the several proteins together (fibres, bundles, networks, etc.). In such a case the probe motion is fast, restricted and thus anisotropic. On the other hand, when protein backbone is unfolded (i.e. random coil), its reorientational motion is faster and, more important, much less restricted, significantly increasing the space available for spin probe to wobble. In this case the probe motion is fast, unrestricted and thus almost isotropic. The anisotropy of the spin probe conformational motion can therefore be a good indicator for local polymer mobility, as schematically presented in Figure 5.1a.

For the analysis, samples were put into quartz capillary tubes of diameter of 1 mm and transferred into the temperature-controlled EPR resonator. EPR measurements were done on X-Band Bruker Elexsys E500 Spectrometer (Karlsruhe, Germany), with microwave frequency of 9.3 GHz, the power of 20 mW, modulation frequency of 100 kHz and field modulation amplitude of 0.2 mT. Several spectra were accumulated to obtain the signal-to-noise ratio (S/N) of 200-300, suitable for further spectral simulation and analysis. Temperature-dependent polymer mobility measurements were performed in cooling-heating cycles from room temperature down to 5°C, followed by a temperature ramp-up to 80°C in steps of 15°C, and a final decrease down to room temperature to check for reversibility or potential temperature-induced structural changes.
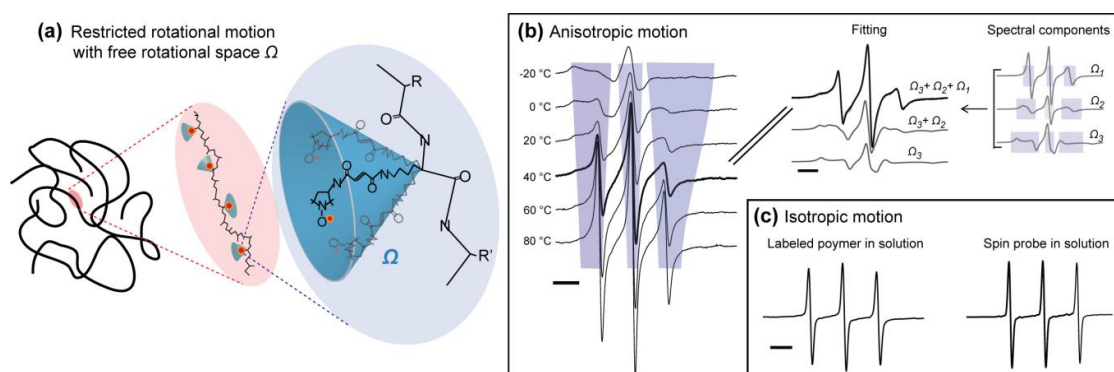

Figure 5.1. Temperature dependent spectral analysis of polymer mobility. (a) – Schematic view of site-directed spin labelling and its conformational dynamics characterized by cone wobbling

model. (b) – Spectra of anisotropic wobbling of polymers in scaffold matrix composed of several spectral components. Temperature induced polymer structure changes influence the anisotropy and the rate of reorientational motion reflected in the lineshape indicated within grey bands. (c) – Spectra of isotropic wobbling, of polymers in solution (left) and free spin probe in solution (right). Spectra have a sharp triplet with narrow spectral lines. The bar range is 10 G.

Spectral analysis took into account that local polymer rotational motion varies from fast unrestricted at unfolded ends and unstructured parts of gelatin polymer chains to fast restricted motion within structured and densely packed parts of chains, both motional patterns being sensitive to temperature. The impact of the anisotropy and rate of reorientational motion of the spin label attached to a polymer on the EPR spectral lineshape was employed to detect molecular motion measured at different temperature. The grey bands indicated in Figure 5.1b show the spectral regions where the lineshape can reflect the motional anisotropy. To extract the information in these parts, we needed to employ spectral simulations to decouple a sharp-triplet component - 3 equal hyperfine lines, reflecting part of the labels being motionally unrestricted - from a component arising from fast tumbling but sterically restricted labels. Spectrum of a disordered polymers in solution (Figure 5.1c), is on the other hand composed of only one spectral component with the sharp triplet due to its isotropic wobbling. By the mentioned spectral simulations done within the software EPRSIM-C (http://lbf.ijs.si/download.html) (111), the anisotropy of the restricted rotational motion was revealed and described by free rotational space Ω, defined as $\Omega = \theta\varphi/(2\pi)^2$, where θ and φ are the two cone angles of restricted rotational motion (99,112). The free rotational space analysis through the entire temperature region was used to characterize the phase transitions of a polymer structure through the detection of phase transition temperature ($T_{\text{ph.tr.}}$), dependent on molecular packing and intramolecular interactions (113). Additionally, average free rotational space Ω_{AVG} was calculated at temperature $T = 37°C$ as $\Omega_{\text{AVG}} = \sum_i d_i \Omega_i$ to characterize an average polymer mobility at the spin labelled amines. Ω_i presents the free rotational space of the corresponding spectral component and d_i its weight.

5.2 Morphology analysis by confocal fluorescence microscopy (CFM)

For this purpose, primary amine groups, mainly on lysine side-chains of polymers, were covalently labeled with reactive isothiocyanate group of FITC fluorescent probe before scaffold preparation. Scaffolds were cut to fit into a Nunc® Lab-Tek® chambered coverglass (Thermo Scientific, Denmark) and placed onto the inverted microscope Nikon Eclipse TE 2000-E. Images were acquired under 15× and 10× objective magnification in confocal mode with Lambda LS xenon-arc lamp source (Sutter Instrument, Novato, USA) and iXon EMCCD camera (Andor, Ireland). For optimal fluorescence detection, excitation, dichroic and emission filters of the CARV IITM unit (BD Biosciences, Franklin Lakes, USA) were selected to meet FITC absorption/emission spectra. The whole setup is schematically presented in Figure 6.4a.

Acquired images of the optical cross-sections were then analysed to characterize wall thickness and pore size distributions using several 1D intensity profiles across an image (Figure 5.2, horizontal and vertical blue lines). Efficient fluorescent labeling, resulting in a

good contrast of fluorescence intensity between scaffold walls and pores, enabled accurate positioning of the scaffold wall boundaries and wall intensity profiles (Figure 5.2), which were fitted with modified Gaussian curves (yellow shaded regions) to determine wall thickness at each position detected (the values at the bottom in μm). To correct the obtained wall thicknesses for non-perpendicular crossings of the walls with the line profile, the crossing angles were calculated from the shifts of the wall positions at two reference line profiles in direct vicinity to the primary one (Figure 5.2, inset). Analysing several line profiles across 5–10 images of the same sample at different sites, sufficient statistics was obtained for construction of the wall thickness and pore size distribution histograms, where the latter was acquired from the measured distances between two closest walls. The average wall thickness and pore size with their standard deviations were finally calculated from the acquired and analysed images.
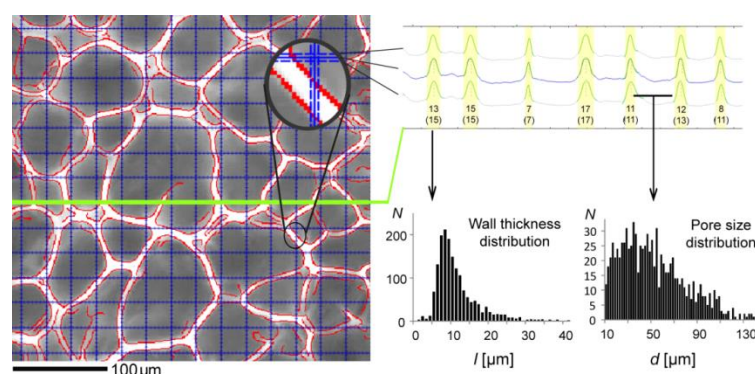
Figure 5.2. Scaffold wall thickness and pore size analysis. (a) Scaffold walls were located by computer designed surface detection based on intensity differences in the acquired fluorescence microscopy image (thin curves surrounding the walls). (b) Line intensity profiles of horizontal/vertical slices were extracted from an image, and the walls' signals (shaded regions) were used to fit the wall thickness via modified Gaussian curves. Calculated values in μm are presented in the bottom, where they were additionally corrected due to the walls' and the line profile intersection angle. (c) The wall thickness and the pore size distributions presented with histograms.

5.3 Mechanical analysis by rheometry, dynamical mechanical analysis (DMA) and atomic force microscopy (AFM)

Dynamic oscillatory shear rheometry (114) was performed to characterize the dynamic shear mechanical properties of the fabricated scaffolds in order search for the possible correlations with cell response. This was carried out at HAAKE RT20 Rotovisco-Oscillatory Rheometer (Thermo Scientific, Germany) in parallel plates oscillatory mode, with 30 mm plate diameter and gap distance adjusted to scaffold thickness of 4mm. Both components of dynamic shear modulus $G(\omega)^*$, storage ($G(\omega)'$) and loss ($G(\omega)''$) moduli were recorded in a constant strain mode over the frequency range of $\nu = 0.1\text{-}100$ rad/s in linear viscoelastic region (LVE) (strain amplitude of 1 percent predetermined with strain amplitude sweep measurement, data not shown). Variations in G' and G'', calculated from the measured dynamic shear stress strain data represent the elastic part (the stored energy per cycle) and viscous part

(energy dissipated by heat per one cycle of loading), respectively, were recorded at reference temperature $T = 37°C$. The measured curves were modelled with commonly applied constitutive modelling, not solving inverse or ill-posed (115). Since simple Maxwell spring-dashpot viscoelastic model was not enough to fit the measured dynamic shear (Figure 5.3, dashed curves), 6-parameters Wiechert model (generalized Maxwell model (116)) was used to adequatelly fit the experimental data (Figure 5.3, blue curves). Each parameter is characterized with the relaxation time τ_i and shear modulus G_i. In terms of scaffold structural or physical properties, τ_i represents the relaxation response of individual domains and G_i its wall strength. For example, smaller pores are represented by smaller τ and thus take over the stress at higher frequencies, whereas bigger pores are represented by bigger τ and thus deform more at lower frequencies. On the other side, G could represent the domain wall strength, where thicker pore walls possess higher stiffness and thus sustain more load, whereas thinner pore walls possess lower stiffness and thus sustain less load. The complexity of the scaffold viscoelasticity comes from its structural inhomogeneity due to broad pore size and wall thickness distribution across its profile.
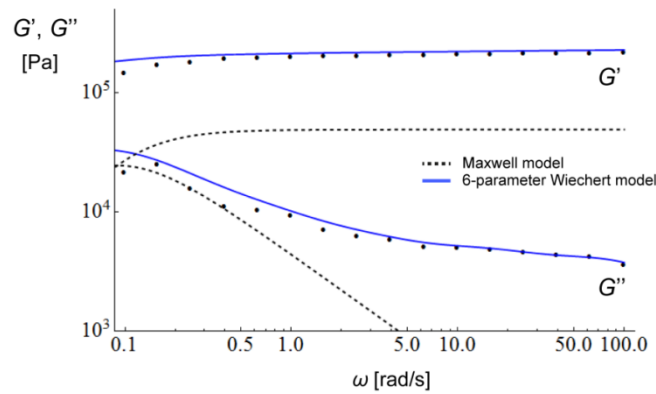
Figure 5.3. Rheological characterization of scaffolds. The measured frequency dependent storage (G') and loss (G'') moduli (black points) were fitted with 6-parameter generalised Maxwell model (blue curve).Simple Maxwell model was not enough to suitably fit the raw data (dashed curves).

Dynamic compressive mechanical properties of scaffolds were characterized by dynamic mechanical analysis (TA Instruments, Q800 DMA) in order to search for the possible correlations with cell response. Linear viscoelastic region was determined first by stress-strain measurements done by oscillatory mode with $\nu = 1$ Hz using compression clamp of cylindrical geometry. The samples were therefore cut with the same shape to properly fit between the compression clamps. Stress-strain was acquired at room temperature within the strain range $d = 30 - 300$ μm, where the upper limit represents 10% of sample deformation in the uniaxial direction. Frequency sweep from $\nu = 1 - 20$ Hz at constant strain, ranging from 1% − 4% (inside the LVE) was implemented to determine frequency dependent compressive storage modulus (E_c') and loss modulus (E_c''). Measurements were carried out at the reference temperature $T_{ref} = 37°C$ in the customized liquid chamber shown in Figure 5.4, to prevent water evaporation during experiment and in order to mimic *in vivo* conditions.

Figure 5.4. Setup for scaffold dynamic mechanical analysis. System is composed of compression clamps of cylindrical geometry mounted on a bottom drive motor. Sample is put in customized liquid chamber and calibrated at the reference temperature T_{ref} = 37°C prior stress-strain and frequency sweep measurements.

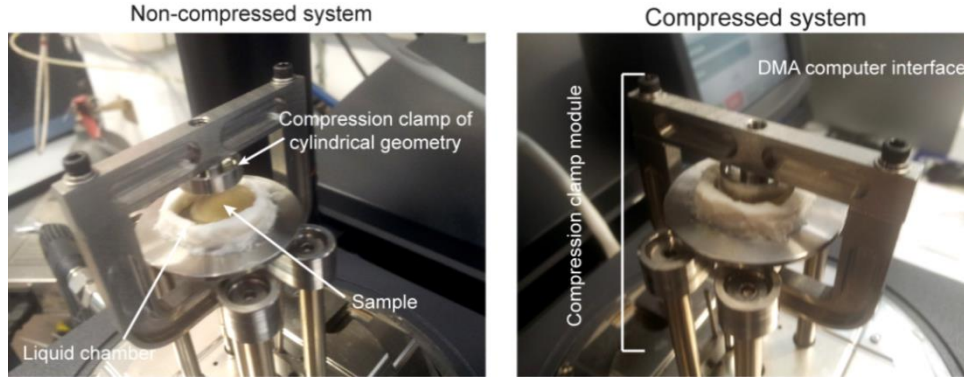Last, the mechanical analysis was done on submicron scale by nanoindentation using AFM as schematically presented in Figure 5.5b, where the technique was recently applied on soft scaffolds for the first time (117). This technique could thus be the most appropriate when searching the possible correlations with cell response. For a nanoindentation we used cantilever with the spring constant of k = 0.01 N/m and four sided pyramide shaped tip of symmetric geometry with the tip radius of 10 nm and front and back angles of 15° and 25°, respectively (Veeco MSCT – C, Bruker, Germany, Figure 5.5b). Scafold samples were loaded with vertical amplitude Δz = 1 µm at constant frequency of 1 Hz. Normal force applied on the scaffold surface was calculated from the measured cantilever deflection Δd with known k. Hertz model for the four-sided pyramid shaped tip (118):

$$F = 0.745 \frac{E}{1-\nu^2} \delta^2 \tan \alpha \qquad (1)$$

was used to fit the force-indentation curve presented in Figure 7.9. E presents scaffold's Young modulus, δ scaffold indentation, a the face angle of the pyramid and ν the Poisson's ratio which describes the material lateral expansion under axial compression. It was set to ν = 0.5 since it shows the best resemblance with the hydrogel (119). In submicron scale indentation our scaffold with the crosslinked polymer network behaves as a hydrogel. If the material would somehow show slight deviation from the estimated ν, it wouldn't have any significant effect on the calculated E according to the equation 1. Indentation was done multiple times in several spots within the small neighbouring area to precisely measure the force curve and hence the Young modulus.

Experiments were done in the liquid cell to preserve the scaffold functionality and mimic real conditions. PBS was added into the liquid-sealed space of the sample chamber mounted on a sample plate prior to any measurements (Figure 5.5a). Scaffold was fixed on the chamber surface with the (biocompatible) glue to prevent its floating after the injection of liquid. The AFM instrument with optical set-up from the top view (Figure 5.5a) enabled an accurate positioning of the cantilever above the scaffold.
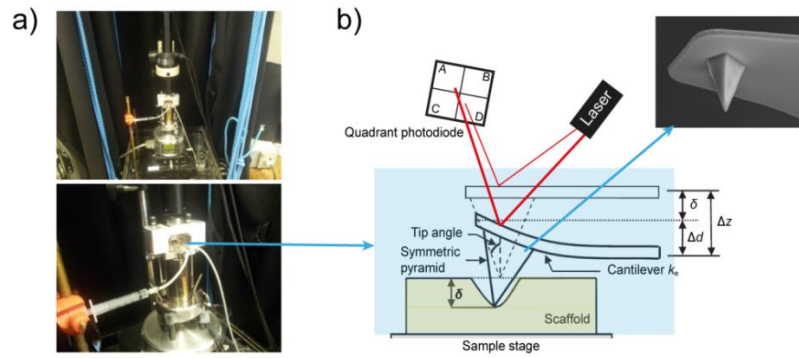
Figure 5.5. Mechanical characterization of scaffolds using AFM nanoindentation. a) AFM instrument with the liquid chamber on the sample stage and optical set-up from the top. Water is injected through the syringe system. b) Schematic representation of AFM nanoindentation experimental system, where piezo-electrically controlled cantilever displacement Δz is the sum of cantilever deflection Δd and indentation distance δ. Tip schematic is adapted from Bruker official site.

6   Cell-scaffold interaction characterization

6.1 Cell preparation for cell growth analysis

Since our objective was to study the spreading and growth of the cells across fabricated, highly porous gelatin scaffolds, which are a model for cartilage tissue, L929 fibroblasts cells were intentionally chosen as they fill spaces and form ECM components within connective tissues throughout the body including cartilage. They were cultured in DMEM containing 10% fetal bovine serum (FBS) and 1% penicillin/streptomycin (PS) at $T = 37°C$ and 5% CO_2. Cells were harvested from the culture plate at the confluent state by incubating in trypsin solution for 2 min at $T = 37°C$. Cells were resuspended with serum-supplemented DMEM and transferred into the 15 ml test tubes ($V = 5$ ml) with the cell concentration of 10^5 cells/mL. Sliced scaffolds of the size $5 \times 5 \times 5$ mm^3 were added into cell suspension and a gentle stirring method using temperature controlled shaking bath (Julabo) was used for 2 min for the controlled cell administration onto the scaffolds. Seeded scaffolds were removed from cell suspension, put into 96-well plates, resuspended with serum-supplemented DMEM and transferred into the cell culture incubator.

6.2 Cell preparation for adhesion dynamics analysis and microspectroscopy

Following the protocol of culturing and trypsinization described above, cells were suspended in serum-supplemented DMEM containing fluorescently labeled fatty-acid membrane probe SPP158 (Figure 4.1) at concentration of $c = 5 \cdot 10^{-7}$ M for 1 min to stain the cell membranes for fluorescence detection. Cell suspension (10^6 cells/2mL) was centrifuged at $300 \cdot g$ for 2 min to remove the supernatant with non-labelled probe and resuspended in serum-supplemented DMEM or PBS at a concentration of 10^5 cells/mL. 400 µl of cell suspension was seeded on a tempered scaffold placed in a Nunc® Lab-Tek® chambered cover glass suitable for high magnification and high numerical aperture imaging and thus highly efficient optical tweezers manipulation and detection.

For the microspectroscopy measurements, cell membranes were stained with the environmentally sensitive fluorescently labeled fatty-acid membrane probe SPP268 (Figure 4.1). Since the probe had to be localized inside the outer plasma membrane as much as possible to gain the highest sensitivity, spectral acquisition was done immediately after staining. Namely, the probe rapidly (in minutes time scale) distributes into the intracellular membranes by an active or passive transport across the outer plasma membrane. Staining was performed right after cell adhesion to the scaffold surface using optical tweezers manipulation as described in details in section 6.4.3.

6.3 Cell growth analysis by CFM and by viability assay

Cell membranes were stained with SPP158 diluted in DMEM at the concentration of $c = 5 \times 10^{-7}$ M for 5 min. Prior the analysis, cell staining suspension was changed with body temperature serum supplemented DMEM to remove all excess fluorescent probe. CFM images were taken under $10\times$ and $15\times$ magnification. Cell number was calculated via thresholding the cell intensity against the darker environment as depicted in Figure 6.1. Cell density ($N_{cells}/unit^3$) was obtained by dividing cell surface area (red region, Figure 6.1c) with the average surface of a single cell estimated prior the analysis. More valuable representation of cell density was acquired by normalization of the cell number to the scaffold surface available for cell growth ($N_{cells}/unit^2$). Since the latter depends mainly on the pore size (within the thin confocal volume), cell density was simply normalized to an average pore size derived from morphology analysis as described previously.
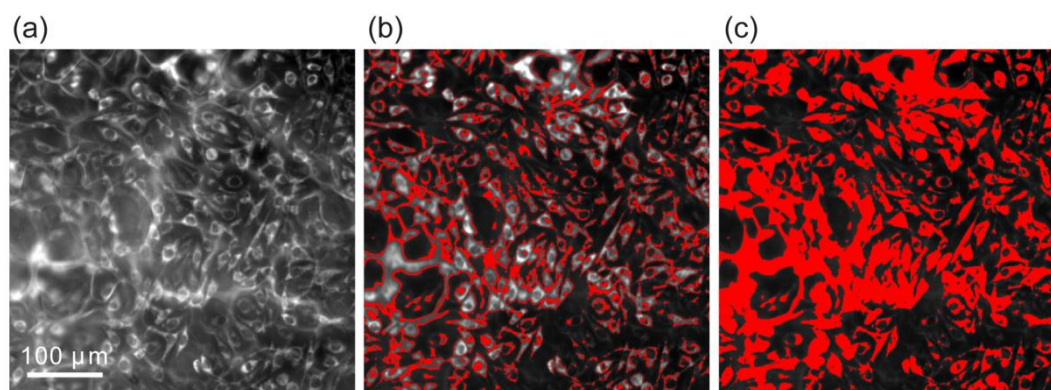
Figure 6.1. Cell growth characterization. a) original CFM image acquired under $15\times$ magnification; b) detection of cell boundaries by thresholding image intensity and c) surface area of cells in a confocal optical volume. Average number and its standard deviation were calculated from 5-10 acquired images.

To quantify cell growth with a complementary test in case CFM test was not sufficient, fluorometric analysis using Resazurin cell viability assay (Invitrogen) was applied. Fluorescence intensity was measured 4 h after Resazurin incubation at the concentration of $c = 500$ µM in DMEM in the corresponding emission filter of 580−650 nm. The reference signal of DMEM was measured to subtract the background. To estimate the total number of cells on scaffolds, Resazurin calibration curve was done by measuring the fluorescence signal at different concentrations of cells grown in cell culture plates (Figure A2 in the Appendix). The viability assay was measured six times for each scaffold. The analyses using both methods were done in the first week after cell scaffold culturing.

6.4 Cell adhesion analysis by optical tweezers (OT) and CFM detection

Before describing the adhesion analysis approach and force measurements, one should be familiar with the basic principles of optical tweezers. In this section we introduce first its physical principles including the force calibration methods followed by its setup on a FMS experimental system.

6.4.1 Optical tweezers

Biological and materials-science has gained a lot of interest among researchers which lead to the development of many new and advanced technologies in the last few decades. One of them is "single-beam gradient force optical trap" or "optical tweezers", invented by Arthur Ashkin (120), which has been used for broad-reaching applications in diverse fields such as biophysics and mentioned materials science and cell biology. Its applications in biology are divided into force measurements and manipulation of single molecules, cell organelles to the whole cells, where typically near infrared laser is used, which is weakly absorbed by living specimen and with thus minimal photodamage introduced.

To understand how optical tweezers work, we should describe the basic physical principles.

Basic principles

The difference in the refractive index between the trapping object and the surrounding medium causes the refraction of passing light. Conservation of the light momentum induces radiation pressure which holds the trapped object in the focus of the diffraction-limited laser beam with the spring-like potential. The force exerted on the object depends on the power of the laser, the difference in the refractive index between the object and surrounding medium and dimensions and size of the object. The force is divided on a scattering force, acting in the direction of light propagation and a gradient force, acting in the direction of the spatial light gradient (Figure 6.2). The first is a counterbalance to the change in the light momentum caused by scattering and absorption on the object and the second, due to the interaction of object dipoles with the inhomogeneous electric field, typical for the laser beam. Both components arise from the very same underlying physics, where in order to obtain stable trapping with the object equilibrated in the focal region, gradient force must dominate over scattering force. This is acquired by a very steep intensity gradient in a sharply focused laser light obtained by an objective with high NA.
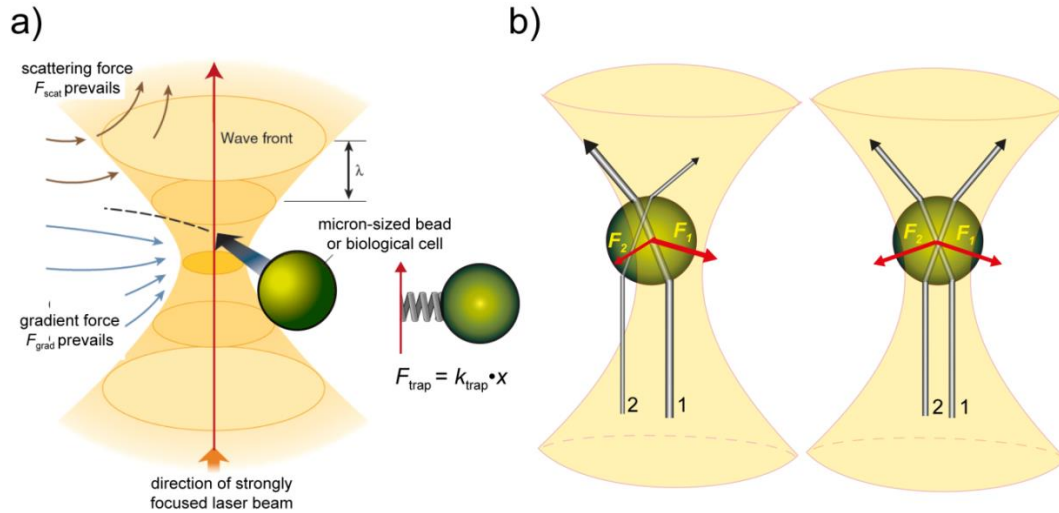
Figure 6.2. Near the focal zone, the gradient force is sufficient to overcome the scattering force. For small displacements of the trapped object from the center of an optical trap, the restoring force is proportional to displacement, which makes the trap as a harmonic potential with fixed stiffness. Scheme on the left adapted from (121).

However, there are two limiting cases of the interaction of a laser beam with the trapped object, dependent on the size of the object. If its radius r is much smaller than the wavelength $r << \lambda$, it is described as a Rayleigh scatterer (forces computed from object being as point dipole), whereas at the $r >> \lambda$ it is describes as a Mie scatterer (forces computed from simple ray optics). When the dimension of a trapped object is comparable to the laser wavelength $r \sim \lambda$ (most of the trapped objects used in various biological applications – investigations of single molecular events (122), cell organelles (123), the whole cells ((80), our thesis)), neither the ray optics nor the point-dipole approach can appropriately describe the interaction. Instead, more thorough electromagnetic theory is required to be in good agreement with the experimental results. Different optimized theoretical approaches were thus applied, one by implementation of object trapping by highly localized in phase EM field accompanied with electrodynamic continuum theory (124) or other by implementation of generalized Lorenz-Mie theory (125), valid from very small objects up to the ray optics region. These theories compute force or trapping efficiency-displacement curves as presented in Figure 6.3a–b. Modelling is done mainly for spherical dielectric objects, as are usually used in biological and biophysics experiments. Such studies are thus essential for quantitative interpretation of force experiments on various biological systems. Force-displacement curve using theoretical model (124) for a spherical 5µm sized Si bead applied in our experiments is presented in Figure 6.3c as a comparison.
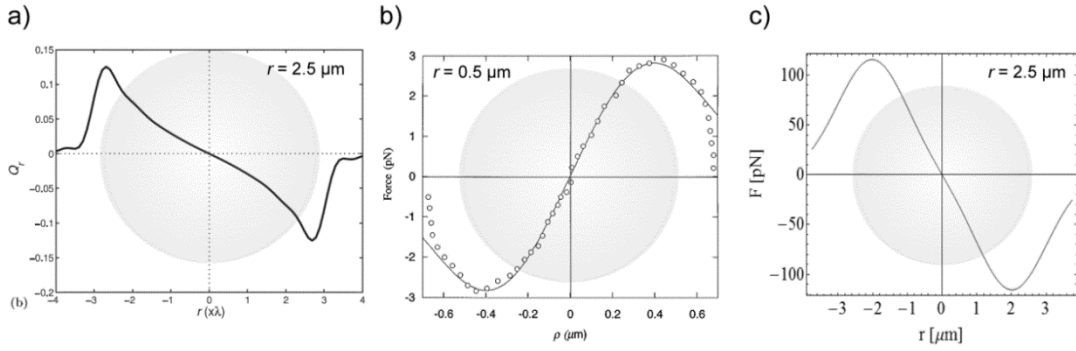
Figure 6.3. Transverse force profiles on spherical objects in a Gaussian beam trap, calculated from different theoretical approaches: a) force profile or trapping efficiency is calculated by generalized Lorenz-Mie theory (adapted from (125)); b) force profile is calculated on the basis of electrodynamic continuum theory accompanied with strongly focused EM field (adapted from (124)); c) force profile on Si microsphere used in our study, calculated from the latter model. Maximal force of approximate 100 pN is obtained with the laser power 100 mW and the beam waist 1 μm. Good agreement of the theoretical curve with the experimental data is shown on figure b. Dimensions of the trapped spherical objects are represented with grey circles.

Force calibration of an optical trap

First method commonly applied to determine optical tweezers force is *escape force method*. It determines the minimal force required to pull the object from the trap, which is usually done by a viscous drag force of the surrounding fluid. Either the trap is moved with the stationary fluid or more conveniently the stage is moved in a defined pattern with the trap remained stationary (126). When the object is pulled out of the trap, fluid drag force levels with the maximum opposite directed restoring gradient trapping force F_{grad}. The latter is however determined by optical properties of refraction at the edges of the trap, where the restoring force is no longer a linear function of the trapped object displacement (Figure 6.3). To determine the trap stiffness k_{trap}, *drag force*, *equipartition*, *power spectrum* or *step response* method are be applied accordingly. By first method, periodic movement of the microscope stage within the linear region of the trap potential is acquired with the object remained in a fixed trap. k_{trap} is computed by knowing viscous drag coefficient b (fluid viscosity and the shape of the object, usually spherical one). By second method, trap stiffness is computed by measuring thermal fluctuations at the position of a trapped particle inside the harmonic potential of the trap: $\frac{1}{2} k_B T = \frac{1}{2} k_{trap} <x^2>$ and no knowledge of object geometry and fluid properties are required (88). By third method, k_{trap} can be measured from the power spectrum of the position (thermal motion) of a trapped object (85,88,127). It is calculated through the fitting of its characteristic Lorentzian shape, where the viscous drag coefficient should be known in the first place. k_{trap} can also be determined by tracking the movement of an object into the trap after sudden displacement of the trap, which must be faster than the characteristic damping time of the object (128).

Usually, damping in a harmonic potential of a trap is high and the system is at low Reynolds number, so that the inertial term in Langevin equation of motion $m\ddot{x} + \beta\dot{x} - F(x,t) = f(t)$ can be neglected. In other words, the viscous term βx is much higher than the inertial term. Additionally, $f(t)$ which presents the thermal force can also be

neglected since it is averaged out on the time scale of trap oscillation period, much higher than the decay time τ of the velocity autocorrelation function (129). The movement of the object into the trap is thus given by:

$$x_{\text{Object}} = x_{\text{Trap}}(1 - e^{-(k/\beta)t}) \qquad (2)$$

where k represents trap stiffness and β drag coefficient obtained from Stokes law $\beta = 6\pi\eta r$. In our study, escape force method was used to calculate maximal gradient trapping force F_{max}, whereas drag force and step response methods were used to calculate k_{trap} and force profile across the observed objects, respectively.

6.4.2 Optical tweezers setup on a FMS system

There are many optical tweezers setups, with single, multiple or counterpropagating trapping, and with various methods for beam stirring and beam detection. What is common to all setups is high-NA optical microscope. Optical tweezers are installed on microscope systems, where lately the method is combined with the advanced imaging or spectroscopic techniques such as confocal microscopy (90,91), fluorescence recovery after photo-bleaching (FRAP) (92) or Raman spectroscopy (130).

In our study, optical tweezers were installed on a confocal fluorescence microspectroscopy system (cFMS) (101) as shown in Figure 6.4. IR laser is mounted on the back side of the microscope, where shortpass dichroic mirror is used to deflect the beam on a microscope sample stage. Acousto-optic deflectors (AOD) are used to steer and multiplex the laser beam, which enable rapid scan of a single beam in 2D to create virtually many traps. Detection system of an optical tweezers trap position is done with two cameras mounted after the passage of light through the CARV unit specified for the fluorescence detection. Such system unfortunately doesn't enable nm-resolution of trap position detection as is acquired with quadrant photodiodes (QPD) (128), but has on the other side specific advantages due to fluorescence sensitive detection.
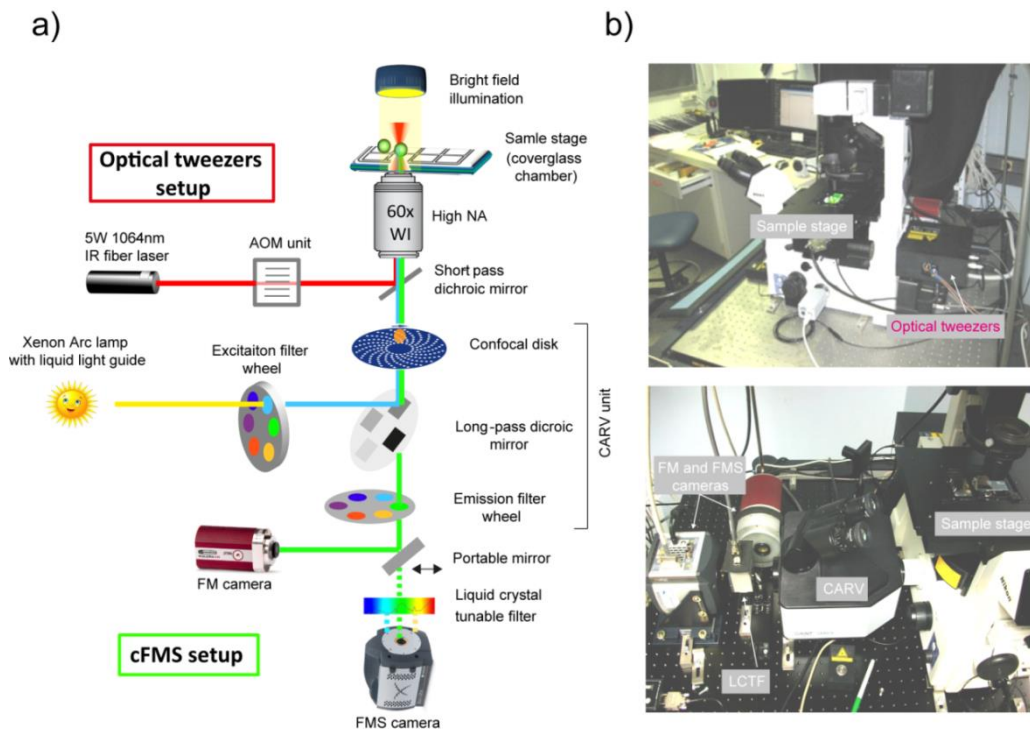
Figure 6.4. Instrument setup used in our study. a) schematic diagram of the optical tweezes built on an cFMS system and b) images of instrument setup. Two light sources are used, 5W IR fiber laser for OT manipulation of the measured system and Xenon Arc lamp for fluorescence excitation of measured system.

6.4.3 Cell adhesion analysis

Cell manipulation with optical tweezers was performed immediately after transferring the cell suspension into the sample chamber containing the scaffold sample. Experiments were performed on the inverted microscope Nikon Eclipse TE 2000-E, implemented with optical tweezers system (Tweez 200si, Aresis) and CARV II unit (BD Biosciences) for the fluorescence detection (101). Cells were trapped in the close proximity to the scaffold surface individually and then accurately positioned in direct contact with the scaffold surface (Figure 6.5a). For cell manipulation in the 3D, acousto-optic deflection system (AOD) mode of the optical tweezers system combined with the z-stage position controller was used. A high Z-axis working distance of 170 μm and high trapping power for sufficient 3D manipulation in the whole Z working distance was enabled by high numerical aperture (NA = 1.27) of the 60× water immersion objective (Nikon) and strong infrared (IR) laser source of 5 W. Due to localized cell heating (131) and known photothermal damaging effect on cells produced by strong focused optical fields (80,132), the laser power applied on cells was limited to $P = 500$ mW, with the maximum exposure time of 1 min. The limiting power was defined by measuring power dependent focal heating using temperature sensitive quantum yield of fluorescent NBD attached to the probe SPP268 (Figure A1 in the Appendix) and by modeling using heat equation, where both nicely correlated (133). The temperature in the focal volume was increased for nearly 7°C and for that reason the heater of the cell chamber was tuned on a 30°C to not exceed 37°C in the exposed volume. With such power, enough

optical force was induced to counteract relevant forces at the interface during and after the adhesion governed by specific ECM proteins (82,134), which is in the range from a few to several tens of piconewtons. More precisely, the setup enabled force measurement up to 200 pN without imposing high thermal stress onto the cells and maintaining biologically relevant conditions. Adhesion analyses were done approximately at the constant height of 50 μm to avoid trapping force being varied by the height (135).

After trapping and bringing the cell to a direct contact with scaffold (Figure 6.5a), two different cell adhesion analyses scenarios were implemented (Figure 6.5b). In the first case, cell adhesion was analysed after particular time of the contact during which no external force was exerted on the cell. Briefly, cell attachment was analyzed by monitoring the amplitude of cell displacement resulted from a single, two seconds lasted OT move (dashed line in Figure 6.5b) with the amplitude of 30 μm parallel to the scaffold surface, conducted after the initial contact time of 1−20 s. The time window was chosen according to the highest OT force sensitivity as measured by preliminary experiments in a broader time window. Experiments were done in DMEM growth media and in PBS with 50 to more than 100 tests to reach adequate statistics. In the second case, the time track of adhesion was analysed by measuring change in the amplitude of cell displacement through periodical OT moves across the cell (dashed curve in Figure 6.5b). Under such a scenario, an external force was constantly introduced on the cell, where its magnitude depended on the relative OT trap position within the cell. Thus, its effect on the lifetime of bonds (136) as well as on their dissociation rate (137) needed to be considered. In our model, cell displacement was inversely related to the number of binding sites established between the cell and the scaffold surface assuming interactions are homogeneous and nonspecific.

Cell displacement was analysed by acquiring cell positions through the cell shape fitting from CFM images with sub 100 nm resolution (Figure 6.6). High contrast of the cell shape was achieved by cell labelling with fluorescent membrane probe.
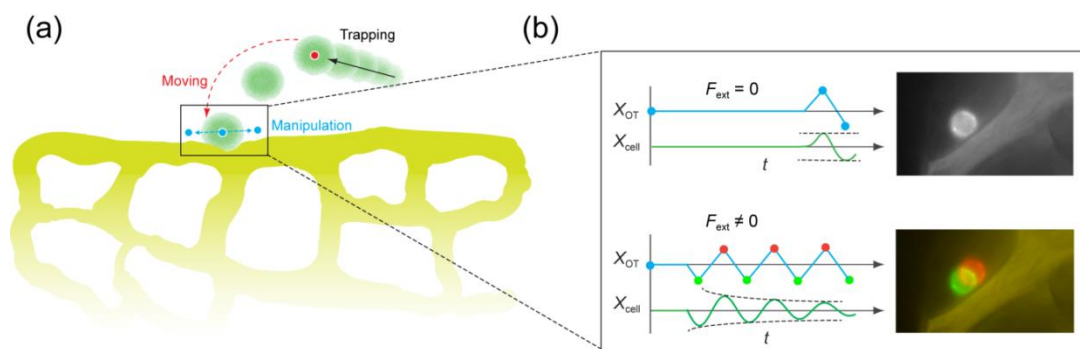
Figure 6.5. Scheme of cell−scaffold adhesion experimental setup. (a) Preparing the system for cell adhesion experiments − trapping, bringing, and manipulation of cells on the scaffold surface; (b) cell adhesion analysis with two different scenarios: when adhesion strength is measured after a particular time of contact (static conditions, no F_{ext} induced on the interface) or measured in time (dynamic conditions, F_{ext} induced on the interface by OT manipulation in the parallel direction to the scaffold surface). Cell displacement amplitude (dashed black line) was tracked to evaluate the binding force.
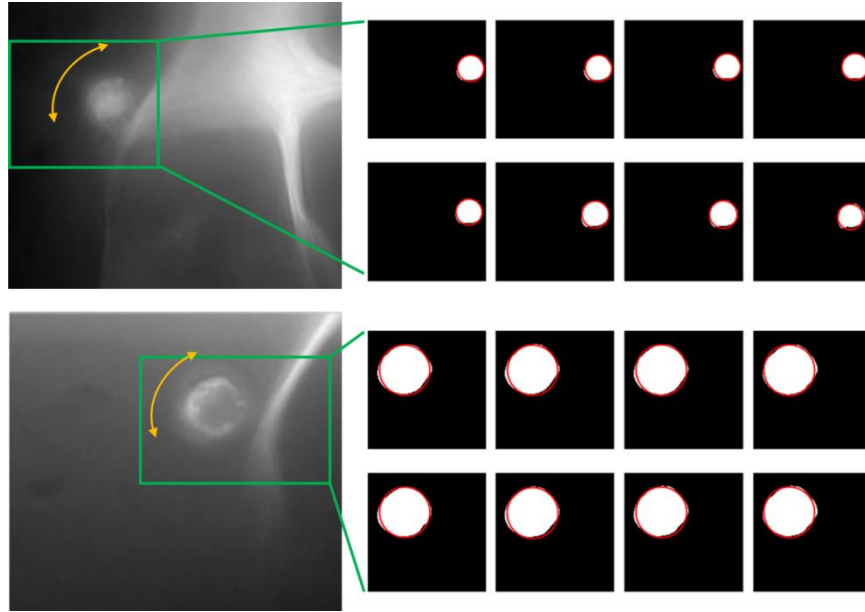
Figure 6.6. Analysis of cell-scaffold adhesion by measuring the amplitude of cell displacement induced by the optical tweezers force. The accuate analysis was acquired by cell fluorescence detection and cell position fitting by a computer software.

Measurement of the force profile across the cell by OT sequential trapping

For a quantitative characterization of the forces on the scaffold−cell adhering interface, OT force calibration was required first. Generally, a trapping stiffness k_{trap} and a maximal gradient trapping force F_{max} are measured by implementing different techniques of a trapped particle tracking, such as monitoring the phase lag between the trap and the moved object when imposing a forced oscillation (93,129) or applying thermal fluctuation method and dynamic viscous drag force approach on a trapped object (88,128,138) as noted in section 3.2.

In our study, force profile across the cell was first measured using OT sequential trapping across the cell with the triangular time function by AOD modulation as shown in Figure 6.7. The period and the frequency of the triangular periodical OT cell manipulation were set in such a way that characteristic damping time of the cell inside the trap was much faster than time period of oscillation and that an optimal imaging detection for force characterization was enabled using fast detection camera (Andor, Ireland). In order to acquire force profile, cell velocity was measured at the corresponding position of the optical trap inside the cell. From the measured cell velocity v_{cell} and cell radius r_{cell} and known fluid viscosity η, force was calculated using Stokes equation. We should briefly explain step-by-step what happens during OT sequential trapping and why trap changes its position inside the cell.

After the trap sequence is introduced, trap is moved from the center of the cell in the steps defined by $\Delta x_{OT} = A_{OT}/N_{OT}$, where A_{OT} is the sequence amplitude and N_{OT} number of trap sequence points in the path (Figure 6.7a). After moving the trap from cell center for $\Delta x_{OT} < r_{cell}$, cell feels gradient trapping force $F_{grad}(\Delta x_{OT})$, which directs the system back into equilibrium. However, if the switching frequency v_s of the trap in the sequence is fast enough, the system cannot get into initial position and trap moves away from the cell center

each time the trap position is changed (Figure 6.7b). At certain point F_{grad} is strong enough that cell starts "following" the trap, which means that cell displacement back into equilibrium in the time defined by inverse v_s, Δx_{cell} α (F_{grad}, $1/v_s$) equals trap displacement Δx_{OT}. In our system, we could neglect the possible phase lag between the trapped cell and the trap, since the trap manipulation frequency ω_{OT} was not significantly higher than characteristic frequency ω_0 related to the trap stiffness $\omega_0 = k/6\pi r\eta$ (129).
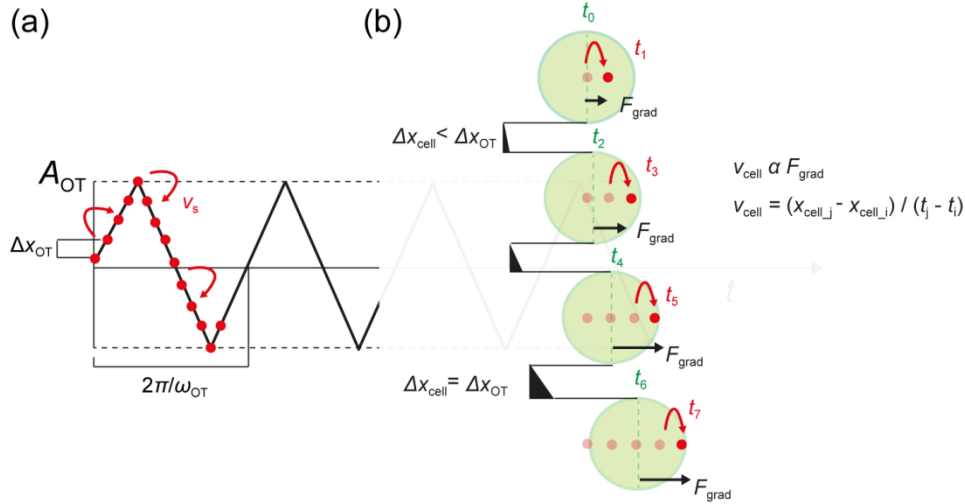

Figure 6.7. Schematic representation of the experiment for the characterization of force profile across the cell. (a) AOD modulated sequential trapping with predefined triangular function was implemented, where the switching frequency of the trap (v_s), the number of trap sequence points (N_{OT}) and trapping step (Δx_{OT}), all of which define v_{OT}, were set in such a way that force profile was characterized almost across the whole cell radius. (b) Scheme of time dependent cell displacement induced by sequential trapping. F_{grad} and its profile across the cell were calculated from the measured v_{cell} and the corresponding trap position relative to the center of cell, respectively.

To calculate the force profile inside the cell, accurate position of the cell and the trap in time was necessary. The latter was successfully employed through a two-photon excitation and fluorescence detection of an optical trap focus (139), where the cells had been labelled with membrane probe SPP158 with Rhodamine attached on the polar head prior measurements. Position of the trap inside the cell was acquired with computer designed image modification via thresholding high trap fluorescence intensity and fitting it with centroid function (Figure 6.8a, computer program and Figure 6.8c, red circles, respectively). To acquire an accurate position of cell, more work was needed. Fitting of the cell position by exploiting the contrat in intensity and intensity gradients across an image was greatly hampered due to strong trap fluorescence signal and low cell contrast due to fast frame rate of image acquisition. Image was thus subtracted with the fitted 2D gauss function at the trap position to adequately remove high trap signal (Figure 6.8b, upper right). Furthermore, a few image filters were applied to suitably fit the cell shape. From the analysis of cell and trap position in time, force profile across the cell was calculated at the trapping power $P = 500$ mW (Figure 6.9). Broad force profile was acquired by implementing step-by-step increase of the velocity of sequential trapping as shown in the inset of Figure 6.9a, where the increase of

the velocity induced higher force on a cell at obviously higher cell displacements from the trap. The data is highly scattered due to non-homogeneity of the cell and the fitting error. While data in Figure 6.9a represents one experiment, data in Figure 6.9b is gathered from 5 different cells. Again, the data is highly scattered, but with no significant differences between individual cells. Rough dependency of the optical tweezers position with respect to the centre of cell ($\Delta x_{\text{OT-cell}}$) and force induced can be seen (marked with illustrative red curve). Trapping force profile was measured within $F = 100$ pN with almost linear dependency of $\Delta x_{\text{OT-cell}}$. It seems that slightly different force profile was obtained with respect to the known force profile on homogenous microspheres (Figure 6.3), which is seen in the initial part of the slope, here, being more flat on average. It could be attributed to the cell non-homogeneity due to its more dense structure towards the outer part and possibly due to some effects of cell structure dynamics through the trapping volume.

During the experiments, cells were not able to escape from the trap, which is seen through $\Delta x_{\text{OT-cell}}$ not exceeding 6 μm (the average cell radius is $r = 8$ μm). It means that force, higher than 100 pN is needed to "push" the cell out of the trap at the power used. For that purpose, escape force method was used later on in the study.
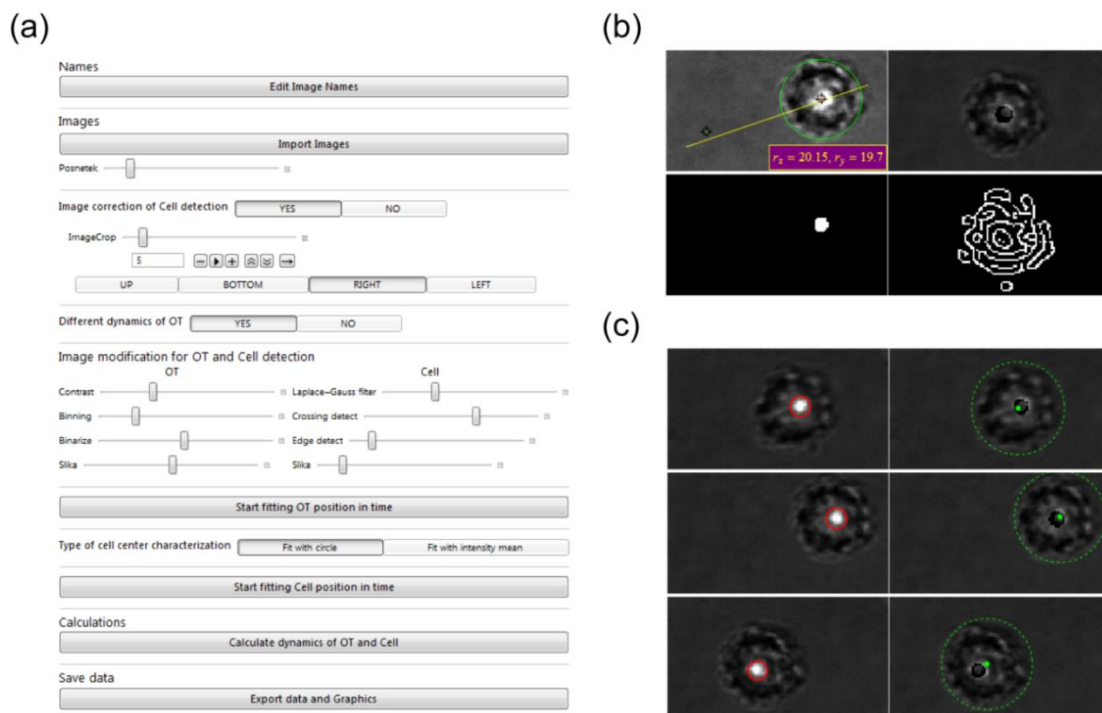
Figure 6.8. Graphical interface of the computer program for trap and cell dynamics analysis (a), image analysis and modification (b) and final fitting of the trap and the cell position in time (c). To accurately fit the position of the trap and the cell, image was modified via thresholding and additional image filtering, such as *Laplace-Gauss*, *crossing detect* and *edge detect*, respectively. To accurately calculate the force on a cell, trajectory of the trap sequence and size of the cell were measured as presented with yellow line and green circle, respectively. Position of the center of cell was most accurately obtained by fitting modified image presented in (b) with circle or by calculating its center of mass.
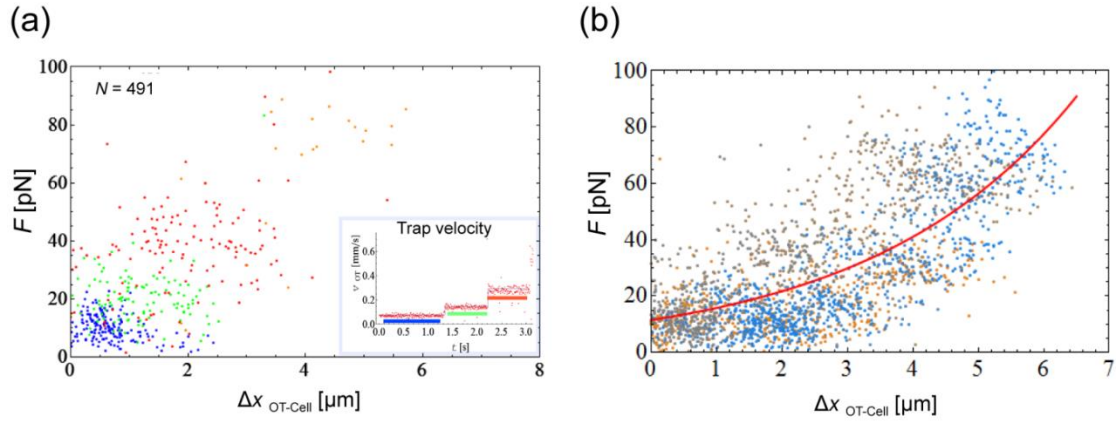
Figure 6.9. Trapping force profile across the cell measured by sequential optical tweezers manipulation (Figure 6.7) with $P = 500$ mW. (a) Force profile acquired on one cell, where the velocity of trapping manipulation was changed in order to gain more data (from blue to red). (b) Force profile acquired on 5 cells (marked with different colours) with the illustrative dependency curve.

Measurement of the trap stiffness of a trapped cell by step-response method

Trap stiffness of a trapped cell was measured using step-response method, which was done as an addition to the previous study of force profile by sequential trapping. Tracking the cell movement into the stationary trap position was applied as schematically presented in Figure 6.10a. For that purpose, cell had to be located in the close proximity of trap position to feel its trapping force potential. Fast cell position tracking was acquired using fast frame rate camera (Andor, Ireland) under 60× magnification. Trap stiffness was calculated according to equation 2 which was fitted to the measured data of cell displacement (Figure 6.10b). The analysis was done at different trapping powers from $P = 340 - 1420$ mW as presented in Figure 6.10c, where the dependency shows nice linear trend. The trap stiffness at $P = 500$ mW, used for cell-scaffold adhesion studies was determined $k_{trap} = 26.0 \pm 5.4$ pN/μm. Since k_{trap} has the linear regime at least few microns from the trap centre, we can assume that escape force of cell has to be higher than 100 pN, which was already conducted in the previous force profile characterization. To measure the exact escape force, viscous drag force measurement was followed and is described in the next section.
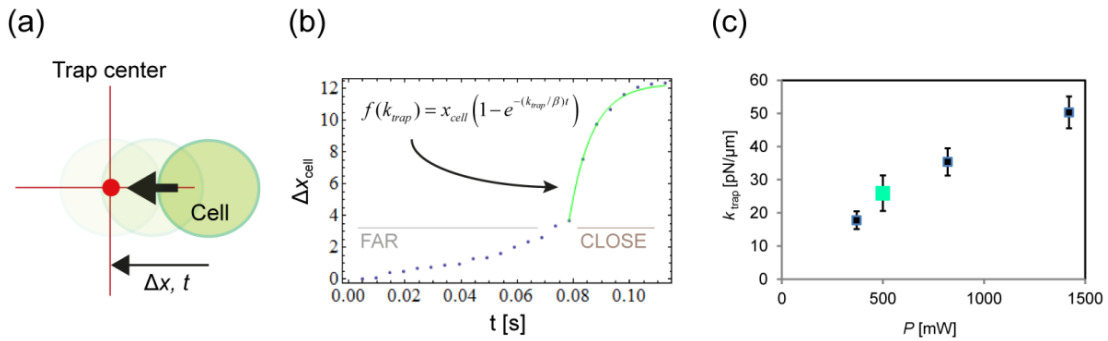
Figure 6.10. Trap stiffness experiment by step-response method. (a) Schematic presentation of cell trapping; (b) fitting the cell displacement curve towards the trap centre by Stokes equation; (c) trap stiffness measured at different optical tweezers powers done in triplicate. Errors represent standard deviation.

44

Measurement of the escape force of cell from an optical trap

The escape force was measured using viscous drag of the surrounding fluid as noted in section 3.2. At particular velocity of the surrounding fluid, viscous drag force exceeds the maximal trapping gradient force F_{max} and the cell is released from the trap. The experiment was conducted by moving the microscope stage in a defined pattern with the trap remained stationary as described in ref. (126). Velocity of the fluid was changed with the amplitude of microscope stage displacement, where the exact dependency had to be thoroughly calibrated. It was done by tracking the displacement of highly contrasted stage-fixed measuring segment using fast frame rate camera (Andor) (Appendix A, Figure A.1a). Velocity of the motorized stage was not constant throughout the displacement as expected. The maximum velocity, responsive for the cell release from a trap was thus subtracted from the part of the displacement curve (Figure A.1a, green line). Rough liner dependency was measured at stage displacements from 10 - 50 μm, with the maximum velocities from 2 - 4 mm/s. This was also the measured velocity which was needed to release the cell from the trap by using optical tweezers powers from $P = 820 - 1420$ mW (Figure A.1b). The escape force for such powers was calculated using Stokes equation ($F = 290 - 380$ pN). Since the power used in cell-adhesion experiments was lower, force was linearly extrapolated from the dependency curve ($P = 500$ mW; $F = 240$ pN) (Figure A.1c). Due to the limitations in the exact fluid velocity characterization and possible deviation from linear extrapolation, the latter force is only a good approximation, but in agreement with previous force profile results.

7 Correlations between scaffold physical properties and cell response

As noted before, scaffold properties are being consistently investigated in relation with the particular cell responses, all for the purpose to better understand biocompatibility and to improve tissue engineering materials. However, the complexity of the cell material interface commonly leaves and opens lots of new questions and non-solved issues. The research field needs new ideas, and one of them is the optimization of scaffold characterization combined with the search for their correlation with cell response. In our study, scaffold physical properties were analysed in a wide spatial range, from molecular to macromolecular, using different methods (see Table 1) and were correlated with the measured cell response.

In first part of the study, accurate physical characterization was done on wide spatial scales, with the focus on molecular scale, where the polymer molecular mobility was thoroughly analysed. Next analysis was focused more on the scaffold mechanical properties and their influence on cell response by additionally introducing stiffer scaffolds from different material and different preparation technique.

Table 1. Overview of the studies done on the fabricated polymer scaffolds

Samples		Sample characterization method				Conclusions
Type	**Preparation**	**Molecular**	**Morphological**	**Mechanical**	**Cell growth**	***…with respect to biocompatibility***
Study 1						
Gelatin scaffolds	Chemical crosslinking + freezing (direct contact with the cooling plate set to T = -10°C)	EPR	FM imaging	Rheometry	FM imaging	Best correlation of cell growth with polymer molecular mobility
Next focus	*Further mechanical characterization and correlation with cell growth.*					
Study 2						
Gelatin scaffolds	Chemical crosslinking + freezing (air contact set to T = -20°C)	EPR	FM imaging	Dynamical mechanical analysis (DMA), AFM nanoindent.	Cell viability assay	No significant correlation with mechanical properties
Polyurethane scaffolds	Temperature induced phase separation (T = -20°C)	/	FM imaging	DMA	Cell viability assay	No significant difference from cell growth on gelatin scaffolds during the first week.

46

7.1 Study 1 - analysis on gelatin scaffolds

The study was done on gelatin scaffolds with different physical properties which were tuned according to the preparation parameters (Table 2).

Table 2. Preparation parameters of investigated scaffolds

Samples	Buffer pH	n (EDC) : n (free COOH sites)*
Scaffold 1	9.5	0.15
Scaffold 2	9.5	1
Scaffold 3	7.5	0.15
Scaffold 4	7.5	1

* Molar ratio.

7.1.1 Molecular mobility of polymer side chains

The scaffolds 1-4 were first analyzed in terms of polymer mobility using spin labeling EPR spectroscopy (as described in section 5.1.). Polymer side chain rotational motion anisotropy via space angle (cone) was characterized, where the side chain is allowed to wobble unrestricted. The revealed temperature-dependent motional restrictions of the spin labeled polymer side chains are presented in Figure 7.1 with "bubbles", where each one represents one detected motional pattern characterized with the free rotational space Ω_i related to the anisotropy of rotational motion (y axis) and the size corresponding to its relative weight d_i. It is shown that motional pattern changes at specific temperature, phase transition temperature ($T_{ph.tr.}$), which is denoted with red dashed bands. $T_{ph.tr.}$ represents measurable physical quantity which reflects the temperature at which tight packing of polymers is lost resulting in a sudden change from anisotropic-to-almost-isotropic conformational motion of spin probe caused by structural changes of a polymer network. Note that conformational entropy of polymer chains become dominant in the free energy above this transition and the conformational space of a polymer chains is maximized.

In the measured temperature range from 0 to 70 °C, $T_{ph.tr.}$ for scaffolds 1–4 was detected at around 0 °C, between 25–35, 40–50, and 55–60 °C, respectively. Regarding the coexistence of different motional patterns through the temperature range scanned, scaffold 1 exhibited nearly isotropic local polymer motion without any other restricted motion through the entire range as represented by the dominating motional pattern with high free rotational space Ω. On the other hand, the rest scaffolds were identified through the coexisting isotropic and anisotropic motional patterns with the weight of the restricted motional component increasing from scaffolds 2 to 4. The EPR spectra acquired at $T = 35$ °C are shown above the temperature diagrams, where the main spectral differences were observed in the two side absorption peaks, most sensitive to the anisotropy of the rotational motion (indicated within colored bands). The other spectra acquired in the whole temperature scan are presented in Figure 7.2.
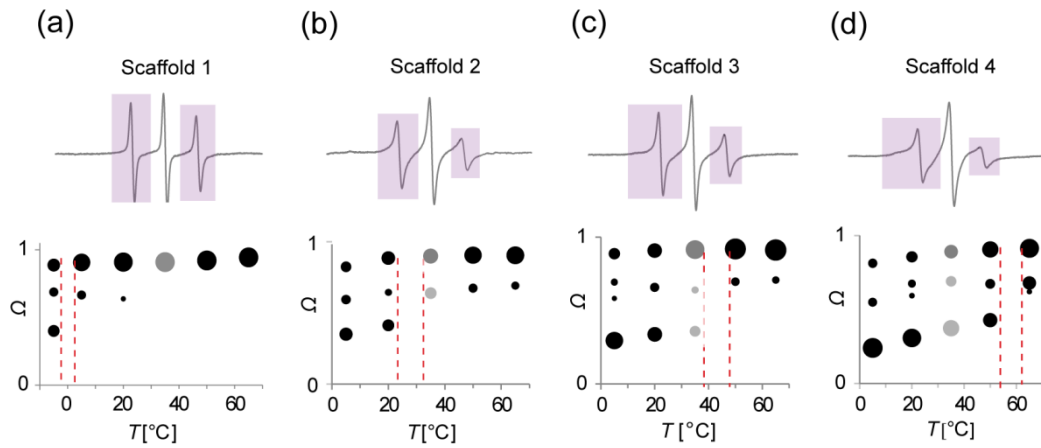
Figure 7.1. Temperature dependent gelatin polymer mobility via free rotational space Ω analysis for scaffolds 1–4 designated with (a–d). The fitted spectral components characterized with Ω are presented with bubbles with the size proportional to their weight. EPR spectra acquired at $T = 35\ °C$ are shown above with indicated the most sensitive parts to the changes in the molecular mobility. Red dashed bands represent the temperature region of polymer mobility $T_{ph.tr.}$
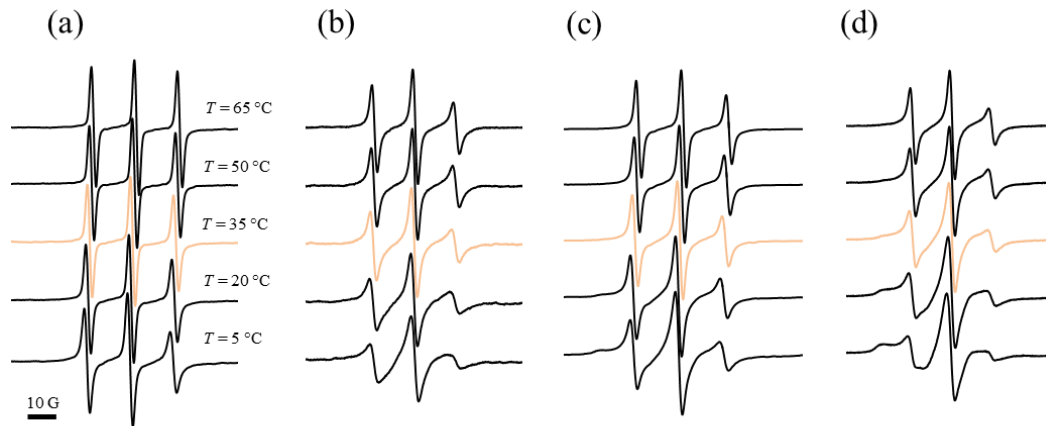
Figure 7.2. EPR spectra of scaffolds 1–4 (a–d) acquired in the temperature range from $T = 5\ °C$ to $T = 65\ °C$.

7.1.2 Scaffold morphology

Morphology of the porous gelatin scaffolds was studied by confocal fluorescence microscopy (CFM) by obtaining typical optical cross sections as shown in Figure 7.3. CFM images revealed well-defined walls and interconnected pores resulting from simultaneous freezing and cross-linking process during scaffold preparation. The scaffolds' wall thickness (d) and pore size distributions (l) were analyzed in terms of histograms as shown in Figure 7.3 insets, marked in black and white color, respectively. The scaffolds' wall thicknesses were $d_1 = 17.1 \pm 0.7\ \mu m$, $d_2 = 19.2 \pm 0.5\ \mu m$, $d_3 = 10.1 \pm 0.6\ \mu m$, and $d_4 = 11 \pm 2\ \mu m$, with an error representing standard deviation of the average values of distributions acquired from 5

to 7 analyzed images. Wall thickness was almost two times smaller in scaffolds 3 and 4 (Figure 7.3c and d), which is, considering the scaffold preparation, a consequence of the pH used. It should be stressed that the correlation between the wall thickness and pH reflects the importance of a polymer net charge during scaffold structure formation throughout cryogelation. Namely, the latter depends on dissociation of carboxylic groups and protonation of amino groups. In the applied pH range primarily protonation of amine groups changed, modifying polymer net charge. With the latter being modulated and the amount of polymer being constant in all scaffolds, the wall thickness variation actually reflects the polymer packing. On the contrary, no correlation between the wall thickness and the concentration of the crosslinkers was observed. The pore size average values of $l_1 = 45 \pm 3.5$ μm, $l_2 = 52 \pm 6$ μm, $l_3 = 38 \pm 3$ μm, and $l_4 = 52 \pm 5.5$ μm suggest that they are primarily influenced by the cross-linker concentration and not the pH. Namely, scaffolds with bigger average pore size were prepared at higher cross-linker concentration. Since the influence of the scaffold preparation parameters on its morphological properties was not the main scope of our work, we did not investigate them in more details.
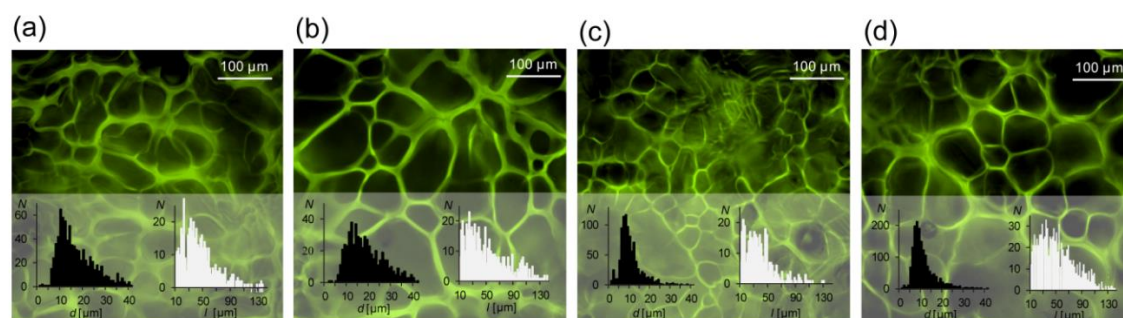
Figure 7.3. Morphology of scaffolds 1–4 (a–d) with wall thickness (black) and pore size (white) distributions in the insets. Images of fluorescently labeled scaffolds were acquired with CFM under 15× magnification.

7.1.3 Scaffold mechanical properties

Mechanical properties of the scaffolds were determined by rheometry. The above charts in Figure 7.4 show the measured storage (G') and loss (G'') shear viscoelastic moduli, presented with the black and grey curve, respectively. The moduli show viscoelastic response analogous to Maxwell with nearly constant storage modulus and decreasing loss modulus at higher frequencies, characteristic for elastic material. Absolute values of moduli differed substantially between different scaffolds, meaning that they would respond in a very different way to stress and handling.

A closer look at the loss modulus curves revealed multiple peaks in the low frequency range and no linear decrease at high frequencies as expected for classical Maxwell viscoelastics, indicating that the complexity of the system exceeded a simple Maxwell model. Scaffold mechanical properties were thus described by a 6-parameter Wiechert model. Each parameter is described with its own stress relaxation time τ_i (140), representing the viscoelastic mechanical response of individual domain in the non-homogenous scaffold

structure and shear relaxation modulus G_i, representing the structure wall stiffness. These sets of pairs are plotted in bottom charts in Figure 7.4.

The results show higher shear moduli in scaffolds 2 and 4 (Figure 7.4b and d), which were prepared with higher crosslinker concentration and vice versa. That indicates the importance of this parameter in final mechanical properties of scaffolds. However, the shear moduli were not found to fully correlate with the morphological properties since the scaffold with the lowest moduli (Figure 7.4a) exhibited neither extreme pore sizes nor extreme wall thicknesses. It indicates that morphological properties do not uniquely determine the macroscale mechanical properties. Moreover, the scaffolds with the similar average wall thickness of 17.1 ± 0.7 and 19.2 ± 0.5 μm, presented in Figure 7.3a and b, respectively, display very different mechanical properties (Figure 7.4a and b). This discrepancy originates in the physicochemical properties of the scaffold walls themselves, which are defined by the density of gelatin packing and its cross-linking during preparation. Although this relationship is far from being simple, we can assume that the position dependent cross-linking degree depends on time evolution of local concentrations of gelatin and cross-linkers. The latter are concentrated by the surrounding freezing nuclei, where the rate of freezing (i.e., concentrating) and cross-linking are temperature-dependent. Variable time evolution of all the concentrations therefore implies also variable mechanical properties of the material. As an example, scaffold 1 was engineered with the lowest amount of cross-linkers at high pH, which changes the efficiency of cross-linking reaction with respect to lower pH used. This resulted in least cross-linked matrix and loose packing as seen through almost two-times higher wall thickness and in the lowest shear moduli.
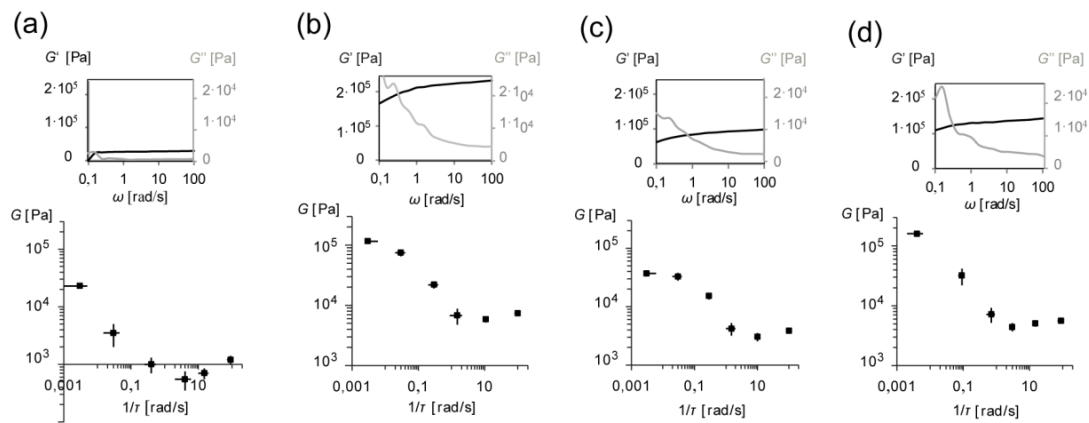

Figure 7.4. Mechanical properties of scaffolds 1−4 (a−d) acquired by dynamic shear rheometry. Above charts represent the raw measurements and below charts the corresponding mechanical spectra determined by 6-parameter Wiechert model.

7.1.4 Scaffold biocompatibility

To investigate the influence of scaffolds' molecular, morphological and mechanical properties (Figure 7.2−8.4) on its biocompatibility, growth of L929 fibroblasts was monitored after 2 days of culture (Figure 7.5). By using two sets of fluorescence detection filters, CFM images nicely show cell population with respect to the scaffold structure. Noticeable differences were identified between the group of scaffolds 2−4 (Figure 7.5b−d) and scaffold 1 (Figure 7.5a), with the approximately five times lower cell growth. First, the number of cells per unit volume (N_{cells}/mm^3) obtained directly from an acquired CFM images was determined: $N_1 = 9000 \pm 3000$, $N_2 = 31000 \pm 8000$, $N_3 = 46000 \pm 4000$, and $N_4 = 32000 \pm 4500$. Second, the number of cells per scaffold surface available for cell growth (N_{cells}/mm^2) was calculated by normalization with their average pore sizes: $N_1 = 60 \pm 25$, $N_2 = 270 \pm 70$, $N_3 = 290 \pm 25$, and $N_4 = 280 \pm 40$. The 5−10 cross sections were acquired from total 3 scaffolds with at least one cross-section from each scaffold. More than two were acquired on those scaffolds that were less homogeneously populated. An error represents standard deviation of the average cell growth obtained from three scaffold parallels. Cell growth was measured also after 1 week of culture using CFM as well as Resazurin cell viability assay. As the cells started to crowd, i.e. densely populating the scaffold, the precise evaluation of the growth was not possible. The measurements of Resazurin fluorescence felt out from the linear regime of fluorescence intensity-cell number dependency of the viability test (141). Nevertheless, it seems that differences in cell growth between the scaffolds decreased with time indicating that the cells slowly adapt even to the less appropriate scaffolds, very likely by producing their own matrix elements which are incorporated in the local microenvironment and thus masking the material native properties, including the mobility of a polymer network.
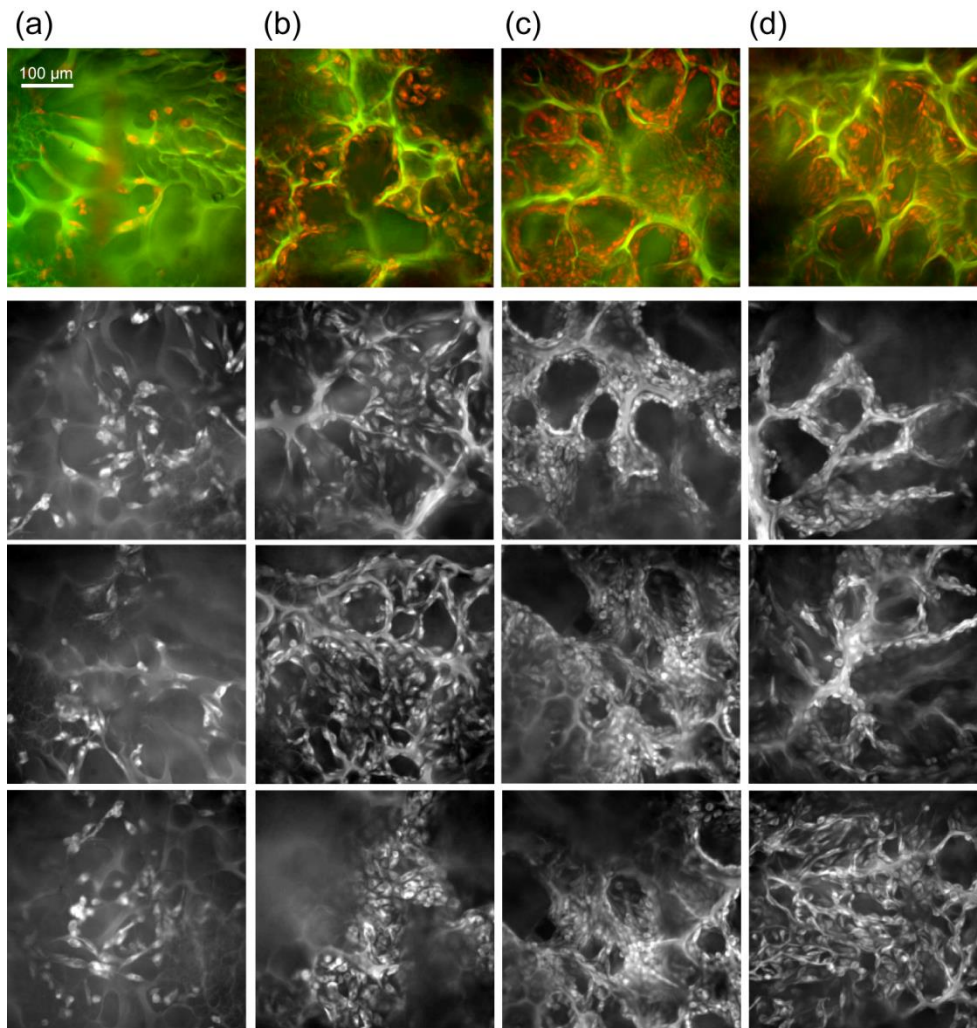
Figure 7.5. Cell growth on scaffolds 1−4 (a−d) measured after 2 days of culture. Cells (red) and scaffolds (green) were labeled with Rhodamine B membrane probe and FITC respectively. Images were acquired under 15× magnification with CFM using two sets of pairs of light excitation and emission filters, corresponding to the fluorescence characteristic of each probe.

7.1.5 Molecular mobility of scaffolds' polymers influences initial cell growth

Different scaffolds, composed of a natural biocompatible and biodegradable polymer, gelatin type B, were fabricated at different pH and concentration of EDC/NHS cross-linkers. Without an intention to investigate the chemistry or the efficacy of the cross-linking of the scaffolds, the variation of these parameters was implemented only to obtain a set of scaffolds with different properties to search for correlations with cell growth (Figure 7.6). One can see that best correlation was found between cell growth and scaffold molecular mobility, specifically with the polymer dynamics phase transition temperature $T_{ph.tr.}$, while no significant correlation was observed with morphology and slightly lower with mechanical properties. Here we discuss the results more systematically.

Starting with polymer molecular mobility, materials with higher $T_{ph.tr.}$ promote cell growth, where the experimental accuracy suggests overall dependency as a linear one. However, the data does not exclude the possibility that there exists a threshold value of scaffold $T_{ph.tr.}$ (between 0 and 30 °C), above which cell growth would not depend on polymer mobility dynamics anymore. Note that $T_{ph.tr.}$ is a thermodynamic property of a scaffold polymer network used to characterize the samples, while the cell response reflects directly the polymer mobility itself. Inefficient cell attachment and proliferation during the first two days of culture (Figure 7.5a) is most likely associated with almost completely non-restricted motion of polymers with the highest free rotational space Ω_{avg} and lowest $T_{ph.tr.}$ (Figure 7.1a). From the results we can assume that cell growth is promoted if the appropriate part of polymer side chain motion is substantially restricted, characterized with the lowest values of free rotational space Ω measured at $T = 37$ °C (Figure 7.1, grey bubbles). This correlation is presented in Figure 7.6a bottom, where the decrease of Ω_{avg} corresponds to the degree of polymer restricted motion, and where the dependency shows the significance of such motional component. The explanation could be found in the cell attachment properties related to the mobility of polymer side chains, where it is believed that the mobility related interaction time for which a polymer binding motif is available for cells to interact with plays a significant role.

By focusing on the morphology, our study cannot reliably confirm that it either correlates or non-correlates with cell growth, which is due to relatively narrow experimental range (Figure 7.6b). However, the average wall thickness as well as the pore size seemed to be mostly uncorrelated with cell growth, which joins the study, where also no effect of pore size was reported (43).

Last, mechanical properties measured by dynamic shear rheometry have shown better correlation with cell growth than morphology. Regarding the shear moduli G' and G'' measured at typical stress induced on a cartilage tissues, $\omega = 1$ rad/s, cell growth did not differ significantly on scaffolds with $G' > 80$ kPa and $G'' > 5$ kPa. It could mean that above this threshold value, cells don't have the ability anymore to respond differently to changing material stiffness (possibly due to too high scaffold rigidity), while below the value, it seems that cells response depend highly on scaffold stiffness. However, the measured shear modulus might not be the best representative of the mechanical property to which the cells actually respond once introduced on the surface. More detailed analysis and discussion about the influence of mechanical properties is presented in the next section.
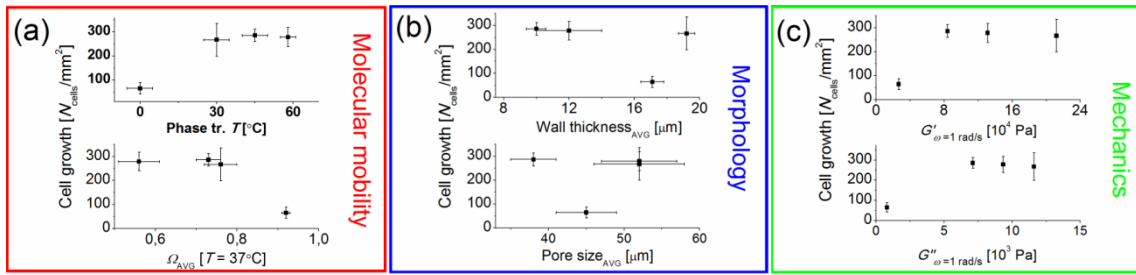
Figure 7.6. Search for the best correlation between cell growth represented as cell surface density (N_{cells}/mm^2) and scaffold properties on (a) molecular scale (polymer mobility phase transition temperature and average free rotational space), (b) microscopic scale (average wall thickness and pore size), and (c) macroscopic scale (storage and loss shear moduli). The errors on y-axis are standard deviation of the average cell growth obtained from three scaffold parallels and the errors on x-axis standard deviation of (a) 3 and (b) 5−10 measurements.

To sum up, scaffold molecular mobility showed slightly better correlation with cell growth compared to scaffold shear moduli. Anyway, both show similar trends, with one point standing out. The question is why to consider molecular mobility more crucial parameter for such cell response? Cell growth which combines cell attachment, cell proliferation and cell migration was measured in first two days in culture, where growth is still greatly influenced by the efficiency of cell attachment. Since cell attachment depends on biophysical and biochemical properties at the interface on a molecular scale, we can reasonably conclude that polymer molecular mobility influences initial cell growth the most. This molecular property, which has never been investigated thoroughly, but was noticed to impact cell response (20), should therefore be considered in scaffold biocompatibility studies. As an example, knowing the exact polymer molecular mobility in addition to the known, e.g. surface chemical structure or surface charge acquired by well-established techniques, could importantly contribute to the current understanding of the processes on the material-cell interface.

7.2 Study 2 - analysis on gelatin scaffolds and polyurethane scaffolds

In order to more proficiently determine how mechanical properties actually influence on cell response one should find the specific one, which the cells actually "fell" during and after the adhesion. For that purpose, the specific mechanical characterization method should be applied. In the scientific society it seems that solving this issue is not of the main focus, since various methods, from tensile tests (47), rheometry (50) and AFM nanoindentation (96,97) are used when searching for correlations with cell response. It is difficult to know, if the mechanics obtained by macroscale rheometry as was in our study is the right choice, and therefore other techniques should not be discounted entirely. On the other hand, it might be possible that different scale techniques give comparable mechanical results. Our next study was thus focused on more thorough scaffold mechanical characterization and its possible correlation with cell growth, implementing dynamic mechanical analysis (DMA) and AFM nanoindentation.

The study was done on gelatin and polyurethane scaffolds prepared with different parameters only to acquire different morphological and mechanical properties (

Table **3**).

Table 3. Preparation parameters of investigated scaffolds

Samples	Sample preparation	Buffer pH	n (EDC) : n (free COOH sites)
gelatin scaffold 1	Chemical crosslinking + freezing	9.5	0.15
gelatin scaffold 2	(direct contact with the cooling	9.5	1
gelatin scaffold 3	plate set to T = -10°C)	7.5	0.15
gelatin scaffold 4		7.5	1
gelatin scaffolds 5a–c*	Chemical crosslinking + freezing	9.5	1
gelatin scaffolds 6a–c*	(air contact set to T = -20°C)	7.5	0.15
gelatin scaffolds 7a–c*		7.5	1
Polyurethane scaffold	Temperature induced phase separation (TIPS)	/	/

* Preparation in different buffers (phosphate, carbonate, PBS).

7.2.1 Scaffold morphology

Morphology of scaffolds was measured by confocal fluorescence microscopy (samples in wet state) and scanning electron microscopy (samples in dry state) (Figure 7.7). The results of SEM analysis done on scaffolds 2-4 and polyurethane scaffold depict the method as a good complementary method to the CFM. The images show well-defined walls and interconnected pores, but with high deviation in the wall thickness and pore size between different scaffolds. As was described in section 7.1.2., it is due to both, the pH and crosslinker concentration used during the scaffold preparation, which determine the final structure. The morphology was not quantitatively characterized since the scope of this part of the study was scaffold mechanical characterization and its correlation with cell growth.
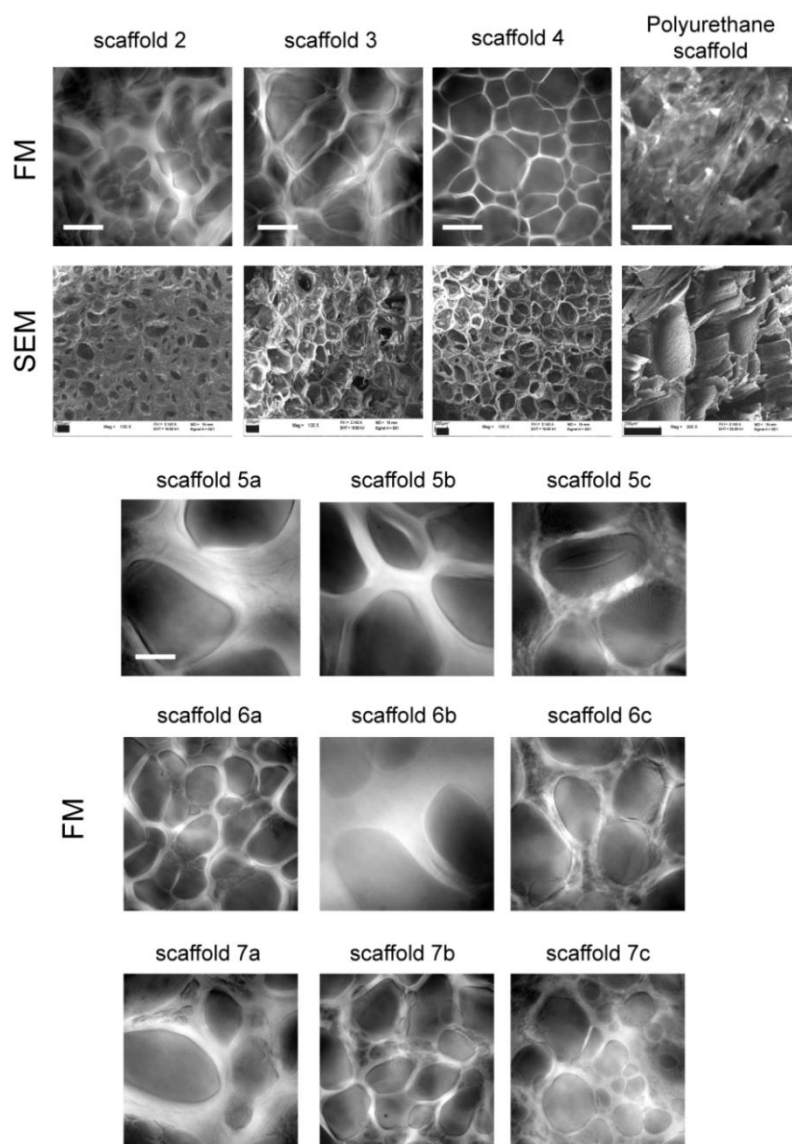
Figure 7.7. Scaffold morphology images done by FM (wet state) and SEM (dry state). Scale bar is 200 μm.

7.2.2 Scaffold mechanical properties

DMA "stress-strain" measurements to determine the linear viscoelastic region of uniaxial compressed scaffolds are presented in Figure 7.8a, whereas "frequency sweep" compression measurements conducted at fixed strain amplitude inside the LVE (black circles) are presented in Figure 7.8b. Almost all gelatin scaffolds showed LVE response at the compressions/strains up to few %, except the scaffold 5a with the non-linear response above 2%. More stiff scaffolds were obtained at the higher crosslinker concentration on average, while both, pH and preparation buffer affected the final mechanical properties. pH dependency was much more pronounced on scaffolds 2–4 prepared by fast freezing (mold in direct contact with the cooling plate).

Storage compression modulus (E_c') exhibited similar trend in all scaffolds, where it increased with the loading frequency. Huge differences of E_c' were measured between individual scaffolds, ranging from 5 kPa to 200 kPa at frequency $v = 10$ Hz. Compression tests were performed also on polyurethane scaffolds (Figure 7.8, black curves). E_c' showed the similar frequency dependency as the one on gelatin scaffolds but with higher strength. In fact, it could be much higher, if the sample was suitably compressed during the measurement. Due to the scaffold shape it was difficult to achieve the homogenous compression over the whole sample. The steep curve obtained by the "stress-strain" test could indicate that the stiffness of these scaffolds is at least an order of magnitude higher than the one of gelatin scaffolds.

(a)

(b)
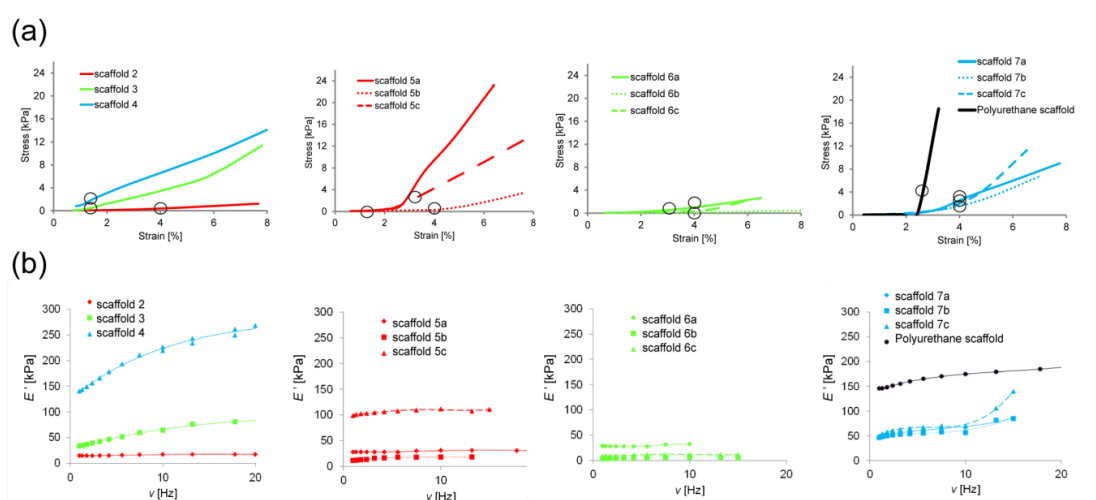
Figure 7.8 Stress-strain (a) and frequency sweep (b) measurements of scaffold dynamic mechanical properties in compression mode. Frequency sweep was acquired at constant strain amplitude between 1–4% according to the linear viscoelasticity profile of each sample (black circles). The figure colours correspond to the individual scaffold fabrication parameters (*red* - high pH, high crosslinker concentration; *green* - low pH, low crosslinker concentration; *blue* - low pH, high crosslinker concentration), while the shape of the curves to the buffer used (see the Table **3**).

Additionally, AFM nanoindentation testing of scaffolds 1–4 was applied to measure their mechanical properties on a local submicron-scale. Their Young modulus was calculated by fitting the cantilever deflection curve during sample nanoindentation (Figure 7.9a) using Hertz model for the four-sided pyramid shaped tip (equation 1). The deflection (Δd) was prior calibrated through the measured voltage signal corresponding to the position of a laser beam reflected from the cantilever tip onto a quadrant photodiode (Figure 5.5b). Scaffold indentation, which was shown in the particular part of the curve (region inside the red vertical lines), was used for further characterization of the Young modulus. Flat part of the curve on the right side means the cantilever is not jet in the contact with the scaffold surface since no Δd is measured, while linear curve on the left side means that there is no more indentation into the scaffold structure since Δd follows the cantilever displacement (Δz). When indenting the stiffest scaffold with such a soft cantilever, the indentation was just the few tens of nm, with the force of approximately 1 nN (Figure 7.9a, inset).

Calculated Young moduli are shown in Figure 7.9b, where the modulus measured on the polyurethane scaffold by the same technique is gathered from ref. (107). Its Young modulus was shown at least an order of magnitude higher than the average Young modulus of gelatin scaffolds, which was calculated between $E = 10$ kPa and $E = 200$ kPa. It is worth mentioning that Young modulus calculated from nanoscale indentation is similar to the frequency dependent complex modulus calculated from macroscale compression testing. It means that macroscale characterization could in principle be used for a good estimation of the properties on much lower scales, despite the fact that scaffold structure is highly porous. However, it is not so straightforward, as the frequency dependent moduli depend on the various setup parameters.

Good correlation between scaffold mechanical and morphological properties was obtained this time. Scaffolds with higher Young modulus had more densely packed structure (thinner walls; scaffold 4), while the ones with lower Young modulus more loosely packed structure (thicker walls; scaffold 2). For the comparison, polyurethane scaffold showed more oriented porous structure but with much higher inhomogeneity.
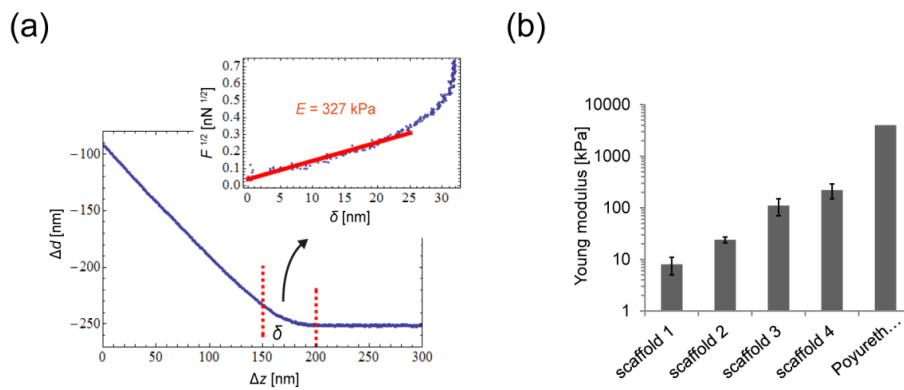
Figure 7.9. Scaffold nanoindentation analysis. (a) cantilever deflection curve and the fitted indentation region for Young modulus E characterization and (b) chart of the measured E. Indentation tests were acquired multiple times (5-10) in several spots within small neighbouring area.

7.2.3 Mechanical properties do not show correlation with cell growth

To check whether mechanical properties influence on cell response, cell growth analysis was done on all scaffolds using cell viability assay. It was measured on the 2, 5, and 9th day after cell seeding. No correlation with mechanical properties was detected in this period, with basically random distribution of cell growth over the mechanical range (Figure 7.10). The mechanical property which was correlated was the stress required to deform the sample at chosen strain (4%), which in general represents the scaffold stiffness. The only scaffold which didn't show any cell growth was the one with the lowest mechanical strength. This might not be attributed to the mechanical property, but rather to the scaffold surface molecular property, e.g. surface charge or polymer molecular mobility as discussed in previous section. Polyurethane scaffolds, which were characterized with much higher stiffness didn't show any significant difference in cell growth (unfilled squares), except after

longer contact time of more than a week, where the cell number increased on average in comparison to the one on gelation scaffolds Figure 7.10c. Broad distribution in cell growth on polyurethane scaffolds can be attributed to the differences in the surface molecular properties (differently functionalized surface), non-homogenous structure and also cell seeding error.

Figure 7.10. Cell growth on different scaffolds after 2 days (a), 5 days (b) and 9 days (c) of culture and the corresponding mechanical properties. Cell growth was measured by resazurin cell viability assay while mechanical properties by uniaxial compression test. Stress required for 4% deformation on gelatin and 1% on polurethane scaffolds is presented on *x*-axis. The error bars represent standard deviation of 5 measurements.

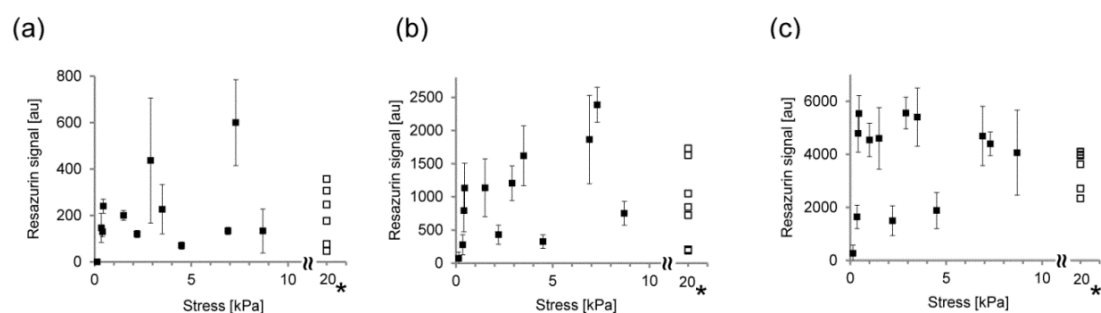In the literature we find number of studies, which investigate the impact of mechanical properties on particular cell response (Table 4). According to this review, cells respond to the substrates with mechanical properties in the range from just few tens of Pa to the values as high as hundreds of kPa. At limiting cases, cells express completely different response with completely different mechanisms of the formation of focal adhesion complexes followed by traction force generation by actin cytoskeleton, induced mechanotransduction and last cell proliferation and differentiation. An example is one study, where they show different cell response to stiffer materials by rapidly developing higher Young's modulus (49). We thus believe that the mechanical properties of cells themselves have to be taken in great consideration when studying interdependency. The mechanical properties of scaffolds should be at least of the same order as the cells' to enable an "optimal" cell response or recognition. Mechanical properties of cells have been thoroughly investigated throughout the last years, where their Young's modulus was calculated between 0.5 kPa and 15 kPa (Table 5). Their stiffness is thus comparable to the stiffness of the majority of the investigated scaffolds, but with still few exceptions (Table 4). Young modulus of our gelatin scaffolds measured by nanoindentation varied between 5 and 200 kPa, which is within the range of the materials' stiffness presented in Table 4 and doesn't deviate from the cell stiffness for more than two orders of magnitude. On the other hand, stiffness of polyurethane scaffolds was measured much higher. According to our hypothesis, the efficient cell growth on polyurethane scaffolds in the later stage (the second week of culture) is very likely non-dependent on its stiffness, but rather on its surface molecular properties, such as are surface charge, protein structure or even molecular mobility. However, the true interpretation might be screened, due to cell secretion of the extracellular matrix proteins, which can strongly modulate the cell response in the later stage.

Table 4. Investigations of the effect of substrate stiffness on cell behavior

Type of biomaterial and cells	Mechanical properties of biomaterial	Mechanical properties of cells	Conclusion	Ref.
Fibronectin and hyaluronan hydrogels, human dermal fibroblasts	0.1 – few kPa (AFM)	/	Cells modify their mechanical response in order to match substrate stiffness. Cells migrate faster on soft scaffolds, while proliferate faster on stiffer ones.	(48)
Polyacrylamide hydrogel, human glioma cells	0.4 – 120 kPa (AFM)	/	Cell migration speed and morphology (traction polarization) depend on ECM stiffness. The stiffness for an optimal cell migration was found at some intermediate between 0.4 and 120 kPa.	(97)
Agarose hydrogel, chondrocytes	/	5 – 20 kPa	Cell mechanics, structure, and function are regulated by the stiffness of the three-dimensional microenvironment	(49)
Collagen-glycosaminoglycan scaffold, preosteoblast cells	0.5 – 2 kPa (Tensile testing machine)	/	Increased stiffness enhances cellular activity within the scaffolds.	(47)
Polyacrylamide gel, human breast myoepithelial cells	0.1 – 50 kPa (AFM)	/	Cells sense the substrate rigidity by different integrin bond dynamics	(96)
Polymer network, neural stem cells	0.01 – 10 kPa (Rheometry, AFM)	/	Substrate modulus directs neural stem cell behaviour	(50)
Collagen-coated polyacrylamide substrate, 3T3 fibroblasts	13 – 30 kPa (Steel ball nanoindentation)	/	Cell movement is guided by the rigidity of the substrate	(142)

Table 5. Investigations of the mechanical properties of cells

Type of cells	Method to determine Young modulus	Measured Young modulus [kPa]	Ref.
Chondrocytes	Micropipette aspiration	0.5 ± 0.2	(143–145)
Human chondrosarcoma, different tissue cells	AFM nanoindentation	In the range from 0.5 – 3	(146,147)
Human breast cells	AFM nanoindentation	1.1 ± 0.8	(148)
Fibroblasts	AFM microrheology	1.6 ± 0.2	(149)
Chondrocytes	Cytocompression	1.1 ± 0.8	(150)
Chondrocytes	Linearly elastic finite element model	In the range from 3–15 and 1–7	(49,151)
Chondrocytes	Microcompression tester	14 ± 1	(152)
Bovine capillary endothelial cells	Magnetic-pulling cytometry	/	(153)

8 Investigation of cell-scaffold adhesion dynamics by optical tweezers manipulation and fluorescence microscopy detection

The aim of our last part of the study was to better understand the cell-scaffold interface during the initial adhesion and to further elucidate the measured effect of polymer molecular mobility on cell growth, suggested to be crucial during the initial cell adhesion. So far, all cell response measurements applied on different scaffolds were acquired at least one day after cell seeding, which is a common approach (72–74), but it many cases, important processes at the interface which lead to a specific cell response are activated much earlier. Accurate characterization of adhesion processes, e.g. force characterization of the first adhesion molecular events measured in real time and physiological conditions still presents a major issue. Therefore, new methods have been developed recently, for example tension gauge tether approach to measure single integrin-ligand bonds (83) and molecular tension-based fluorescence microscopy (MTFM), to measure piconewton forces exerted by cell surface receptors (84). In our work, force characterization of early adhesion events was conducted with the optical tweezers technique, which is due to the ability of 3D manipulation of individual cells with independent 2D or 3D control and easy handling and visualization of the investigated systems considered favourable over other advanced methods.

The adhesion analysis was conducted on scaffolds 1–4 (Table 3) and the potential differences were search for.

8.1 Molecular mobility of polymer side chains

This physical property was measured first since it was shown before as an essential parameter for the initial cell response on the surface of polymeric scaffolds. The EPR spectra were acquired at room temperature $T = 25$ °C and are presented on Figure 8.1a. Free rotational space of polymer side chains Ω_i, measuring the anisotropy of their rotational motion with the corresponding relative weight d_i were calculated from spectral fitting and are presented with "bubbles" on Figure 8.1b. We can see that spectral line shapes narrow and increase as we go from scaffold 4 to scaffold 1 (denoted by black arrows), which means that the restricted motion of polymer side chains - most broadened spectral component - slowly disappears (highlighted in grey and by red dotted arrow on "bubble" diagram). Average free rotational space Ω_{AVG} thus increases from scaffold 4 to scaffold 1: $\Omega_4 = 0.59$, $\Omega_3 = 0.77$, $\Omega_2 = 0.86$ and $\Omega_1 = 0.92$ at room temperature. Since Ω_{AVG} showed almost linear increase in the temperature range from $T = 5$ °C to $T = 50$ °C as measured in first part of the study (see the section 7.1), we can accurately estimate Ω_{AVG} at $T = 30$ °C (temperature during cell adhesion analysis) and at $T = 37$ °C (temperature during cell growth). By extrapolation we obtained: $\Omega_4 = 0.63$ (0.68), $\Omega_3 = 0.80$ (0.85), $\Omega_2 = 0.88$ (0.91) and $\Omega_1 = 0.93$ (0.94).
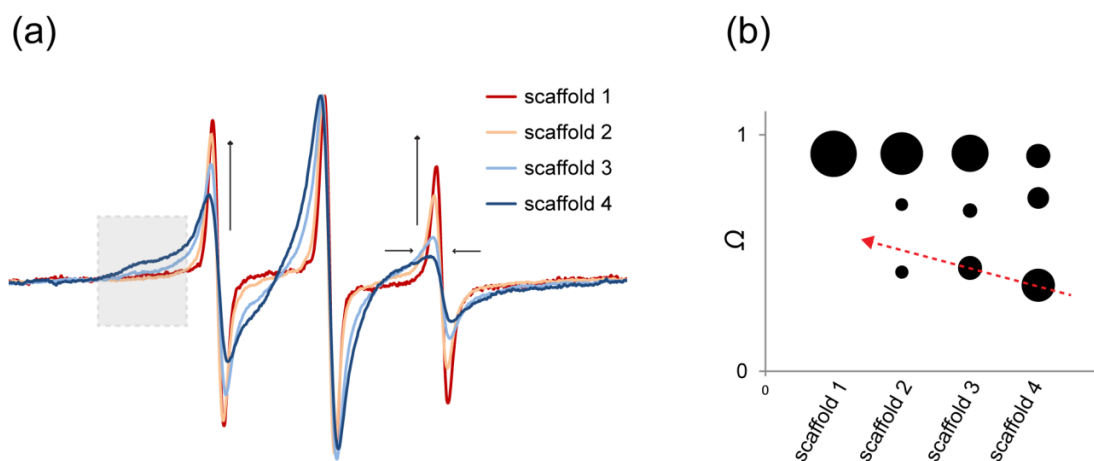
Figure 8.1. EPR spectral analysis of the molecular mobility of polymer side chains in the scaffolds 1–4 measured at $T = 25$ °C. (a) EPR spectra showing the line shape broadening (narrowing); (b) "bubble" diagram of polymer free rotational space Ω calculated for individual domains of the size corresponding to the bubble size. The dotted arrow shows on the dissapearing anisotropic domain.

8.2 Scaffold biocompatibility

To check whether cell adhesion dynamics relates with the molecular mobility of polymers and thus constitutes biocompatibility concept, reference fibroblast growth was monitored first on the investigated gelatin scaffolds 1–4 (Table 3). Cell growth was measured after one and seven days of culture via CFM and cell membrane staining (Figure 8.2). Although some differences can be identified already after 1 day, especially between a pair of scaffolds 1 and 2 and a pair of scaffolds 3 and 4, the statistical analysis (Figure 8.3a) cannot confirm this result as a significant one ($P = 0.135$; all the data compared simultaneously). The major problem originates in the high deviation of the cell number throughout the images due to generally low number of adherent cells that were counted over the limited field of view of 0.6 mm². To resolve this issue, cell growth was additionally analysed with Resazurin cell viability assay (141), which reaches better statistical relevancy by measuring the number of cells across the whole sample (Figure 8.3b). Analysis was done in six parallels. By this test, significant difference in cell growth between individual scaffolds was acquired already after 1 day of cell culture, with $P < 0.005$ when comparing scaffold 3 with 1 and 2 and $P < 0.001$ comparing scaffold 4 with 1 and 2, while no significant difference was acquired between pairs of scaffolds (1 and 2) and (3 and 4). The Resazurin assay thus clearly revealed that cell growth differentiates already during the first day of culture. In addition, the ratios between scaffolds' cell growth remained practically unchanged after one week with no notable change in P value between individual pairs. The total number of cells on scaffolds was estimated from the Resazurin calibration curve (Figure B.1. in the Appendix).

Although the CFM analysis cannot adequately support the Resazurin results due to high deviation, it can on the other side provide insight into the cell morphology, proliferation, and migration through the scaffold. For example, efficient cell spreading around scaffold

pores with more layers was observed on scaffolds 3 and 4, while less spreading with weak contact between cells was observed on scaffolds 1 and 2 (Figure 8.2, third column).

Again, the results show the correlation between cell growth and scaffold polymer molecular mobility. Less biocompatible scaffolds 1 and 2 exhibit higher Ω_{AVG} with practically no restricted motion at T = 37 °C, $\Omega_1 = 0.94$ and $\Omega_2 = 0.91$. On the other hand, more biocompatible scaffolds 3 and 4 exhibit lower Ω_{AVG} with the substantial fraction of the restricted motion especially the latter one, $\Omega_3 = 0.85$ and $\Omega_4 = 0.68$. $\Omega = 0.85$ could represent the upper threshold value for the efficient initial cell growth. To determine how the initial cell growth is dependent on cell adhesion dynamics, which could in fact be governed by polymer molecular mobility, the next focus was to characterize cell adhesion in real time.
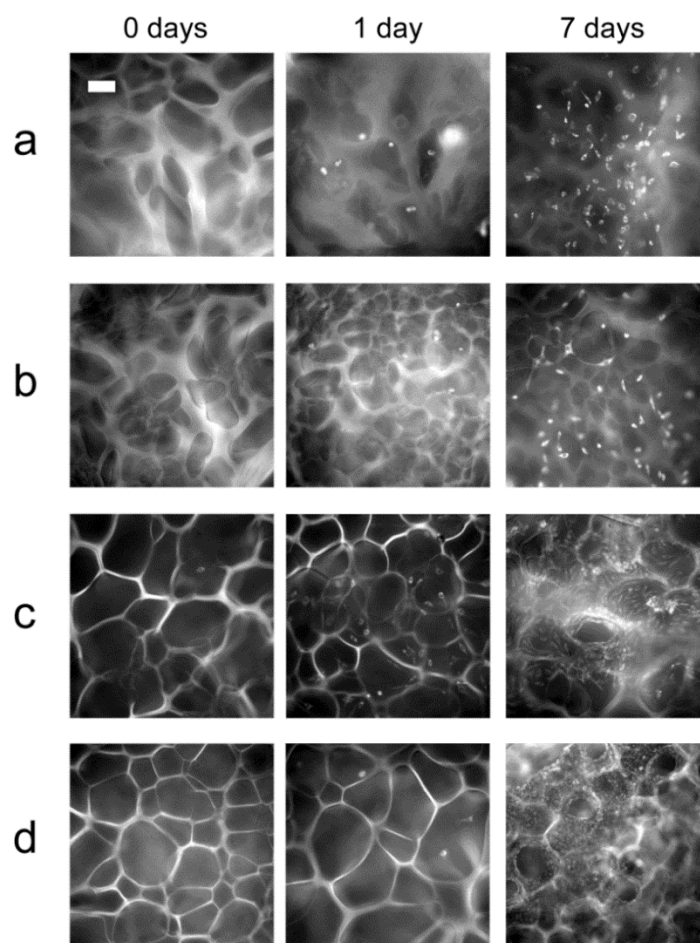
Figure 8.2. Fibroblast cell growth on scaffolds 1−4 assigned with a−d. Images in the first column show scaffold morphology, while the images in the second and the third column show cell growth after 1 and 7 days of culture, respectively. Images were taken using confocal fluorescence microscopy with 10× magnification. Scaffold polymers were labelled with fluorescein isothiocyanate (FITC) during fabrication and cells with SPP158 membrane probe prior analysis to acquire good fluorescent resolution and contrast. Results presented here are complemented with cell viability assay results shown in Figure 8.3b. The scale bar in the upper right corner represents 100 μm.
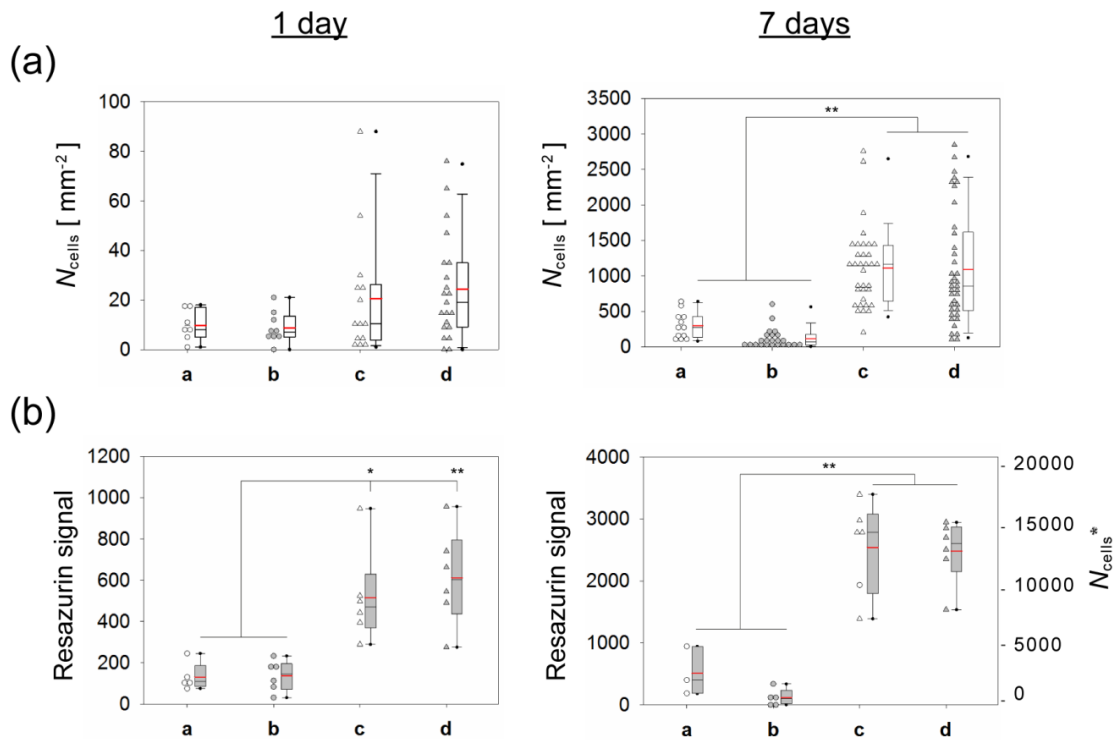
Figure 8.3. Cell growth of fibroblasts on scaffolds 1−4 assigned with a−d measured by a fluorescent detection of stained cells (a) and by Resazurin viability assay (b). Analysis was done after 1 and 7 days in culture. Measurements are represented with dot density plots with raw data on the left side of the bars. The boundary of the box closest to zero indicates the 25th percentile, lines within the box mark the median (black) and the mean (red), and the boundary of the box farthest from zero indicates the 75th percentile. Error bars above and below the box indicate the 90th and 10th percentiles. Data was correlated pairwise using statistical analysis: (*) $P < 0.005$; (**) $P < 0.001$. Optical detection was performed in three parallels each with 5−10 acquired images, and viability assay, in six parallels.

8.3 Classification of cell adhesion

To search for the potential correlation between cell adhesion and initial cell growth, adhesion dynamics was studied by using advanced system of optical tweezers manipulation combined with confocal fluorescence microscopy detection. During the analysis, different adhesion strength was observed through the measured cell displacement within OT manipulation as depicted in Figure 6.5. Accordingly, three scenarios were defined, connecting different trap position dependent profiles of cell displacement and OT force induced on the interface (Figure 8.4.):

a) In the case of high adhesion, the initial adhesion was too strong to be broken by the OT force of approximately 200 pN as measured by cell escape force (see the Section 6.4.3). In this scenario the amplitude of cell displacement corresponds to the inverse number of integrin−ligand bonds at the interface. Due to strong adhesion, slight cell displacement was observed only when the highest force was exerted (illustrated with D_1), i.e. when the optical trap was positioned in the region with the highest refractive index gradient Δn (120), which is towards the cell membrane (first vertical dashed line). When

passing this point of the highest OT force, the cell could not be detached from scaffold. Instead, cell was released from the trap (illustrated with D_2) and shifted back to the initial position, due to release of the force-induced stretching (second vertical dashed line). The adhesion profile was quantitatively measured by tracking the cell displacement induced by OT sequential trapping through the whole cell region (Figure 8.4d). When the OT position approaches the denser part of the cell with the highest Δn, the cell displacement from the equilibrium is more pronounced as denoted with the steep curve. When OT position is on the membrane, force starts to decrease and cell is slightly shifted towards the equilibrium (the last point and the last picture). The position of OT is measured through the fluorescence acquired by two-photon excitation phenomena of the strongly focused IR OT laser on the fluorescent membrane probe SPP158. Maximum amplitude of cell displacement of 5 μm was estimated for this adhesion type assuming geometrical and topological aspects of the cell surface with multidomain binding structures extending out of the lipid bilayer for 50 nm (136) accompanied by the surface microvilli of the size up to 500 nm (154), and considering additional bond and cell stretching due to OT force (155).

b) In the case of low adhesion the amplitude of cell displacement was higher than 5 μm, meaning that OT force of 200 pN was strong enough to break the initial contact. However, new attachment sites were formed before cell detachment. In this scenario the amplitude of cell displacement corresponds to the inverse rate of bond formation while rolling the cell along the scaffold surface. By such a dynamic binding analogous to the rolling attachment mechanism of leucocytes to endothelium in a shear flow (156–158), force can induce an increase in bond rupture during manipulation. The latter can be detected through the rapid increase in cell displacement caused by bond release which changes also the force profile (illustrated with D_3). Otherwise, the force profile is similar to the first scenario with high adhesion, as long as the trap is positioned within the cell where it experiences bond stretching (illustrated with D_4).

c) In another case of low adhesion cell binding is realized through the membrane tethers where cell displacement ranges from 5 to 20 μm. The amplitude corresponded more to the size of the extracted tether and not so much to the number of bonds formed through the tether or membrane−cytoskeleton tension, which was therefore approximated as being constant. Tethers were recognized through the cell displacement at small exerted force which is characteristic for lateral translocation/flow of lipids. In this roughly linear regime, force induced tether formation and stretching can be well described with spring constant (159), where the force profile was of a similar shape as the cell displacement profile (illustrated with D_5). Note that the force induces flow of the lipids from the cell membrane reducing the cell internal volume and thus creating an increased pressure inside the cell. After the force is released, the internal pressure tends to increase the volume again by retracting the lipids from a tether back into the normal membrane state. This results in a backward motion of a cell toward the initial position (before force was applied).
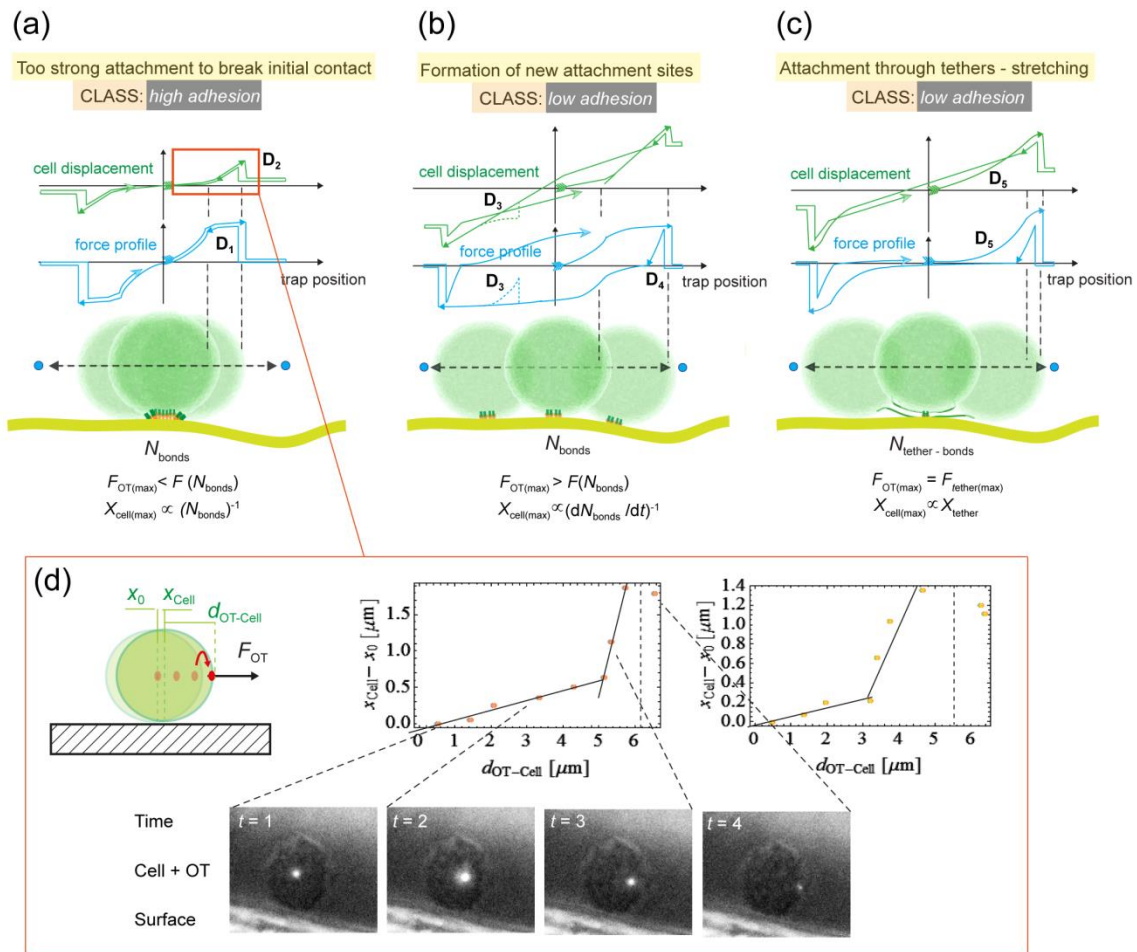
Figure 8.4. Observed scenarios of cell adhesion to the scaffold surface (a−c), characterized with optical trap position induced cell displacement (green) and OT exerted force (blue) and (d), quantitative characterization of strongly adherent cell. In all scenarios, cell adhesion is strong enough to withstand OT force, but different cell displacement profiles point to different adhesion strength and mechanism: (a) small cell displacement is observed due to too strong adhesion to break initial attachment site; (b) high cell displacement is observed due to the breakage of initial attachment sites, where new ones are formed before cell detachment leading to rolling of the cell along the scaffold surface; (c) high cell displacement is observed due to adhesion through membrane tethers. They could be seen optically or recognized by OT induced cell displacement profile. The profiles have specific characteristics, which is denoted with characteristics $D_1−D_5$: (D_1) slight cell displacement is observed when the highest force exerted with its profile unchanged by the direction of OT manipulation due to the type of adhesion; (D_2) cell displacement back into equilibrium position after the release of the stretched cell from a trap; (D_3) rapid increase in cell displacement and decrease in force induced on the interface due to bond detachment (optional); (D_4) bond stretching; (D_5) tether formation and tether growth.

Each individual cell adhesion was classified with respect to the described cell attachment scenarios, which is presented in Table 6. The adhesion strength (1−4) was defined according to the measured amplitude of cell displacement. For cell displacement of less than 5 μm, cell adhesion type was identified as type (a) with adhesion strength 3−4. The number of bonds was roughly estimated according to the known experimental data of force per single integrin mediated bond with specific ECM amino acid sequence which was shown ∼50 pN after the interaction with collagen matrix (81), ∼40 pN after interaction with RGDfK peptide (83), and ∼20 pN after the interaction with fibronectin (82). For cell displacement of more than 5

66

µm, cell adhesion type was identified with low strength (1−2) and as type b or c dependent on the characteristic force and cell displacement profile. Accordingly, binding rate (N_{bonds}/s) or tether size was roughly estimated. In case of nonadherent cells or cells detachable by the force of OT, the adhesion strength was identified with 0 or 0.5, respectively.

Table 6. Classification of cell adhesion according to the amplitude of cell displacement

Adhesion type	Adhesion strength [0 - 4]	Cell displacement [µm]	Number of bonds[a] (N_{bonds})		
Figure 8.4a	4 – High	< 1	> 50		
	3 – High	1 - 5	> 10		
Adhesion type	Adhesion strength [0 - 4]	Cell displacement [µm]	Binding rate [N_{bonds}/s]	OR	Tether size
Figure 8.4b OR **Figure 8.4c**	2 – Low	5 – 15	> few		Few microns
	1 – Low	> 15	≅ few		10 microns and more
	0.5	Slow detachment	few		/
	0	Instant detachment	<1		/

[a] Number of bonds was roughly estimated according to the experimental data of force per bond (82,83,134,159).

8.4 Seconds scale adhesion dynamics correlates with cell growth

As described, each cell adhesion experiment was characterized with the strength 0−4 and the corresponding time of contact, which was represented with 2D Gauss probability profile:

$$f(t, \text{Adh}) = \exp\left(-\left(\frac{(t-t_0)^2}{2\sigma_t^2} + \frac{\left(\text{Adh} - \text{Adh}_{avg}\right)^2}{2\sigma_{\text{Adh}}^2}\right)\right) \tag{3}$$

with the variances σ defined by corresponding measurement errors. By summation of all data points, contact time dependent distribution of adhesion strength was obtained as represented with contour plot (Figure 8.5). Final probability distributions were normalized to the number of data points.
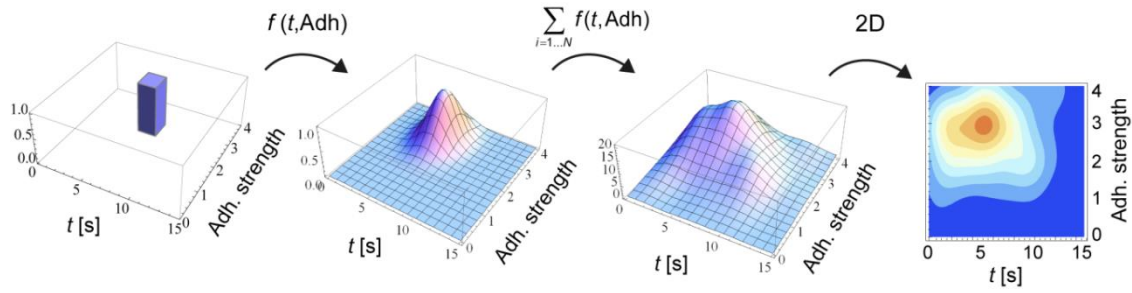
Figure 8.5. Construction of the contact time dependent cell adhesion strength distribution. Each analyzed cell adhesion was represented by a 2D Gauss function with the variances corresponding to the measurement errors ($\sigma_t = 1$ s and $\sigma_{Adh} = 0.5$). After summation of all data points, the distribution was represented with color-coded contour plots.

The results of cell adhesion analysis are presented in Figure 8.6, where the measurements were done both in serum supplemented growth media DMEM and in PBS to check for the potential influence of serum proteins. Comparison between scaffolds 1−4 (a−d) was studied through the difference in distributions, taking into account adherent and nonadherent cells separately or all data points (adherent and nonadherent cells) together. Adhesion strength was measured comprising only adherent cells, whereas overall adhesion comprising all the data (Figure 8.6, third and fourth column). Cell adhesion was found to be significantly different between scaffold 2 and scaffold 3 with the $P = 0.01$ and even more different between the scaffolds 2 and 4 with $P = 0.001$, both measured in growth media. In PBS, the significance is even more pronounced ($P = 0.001$ in both cases). To note, scaffold 1 was not identified as significantly different from scaffold 2. Similar relationship was found when comparing cell growth on different scaffolds (last column). This means that overall adhesion (adhesion strength combined with the probability of the cell adhesion) measured in first few seconds might serve as an indicator to predict the initial cell growth.

By focusing back on the results of adhesion distribution analysis, a remarkable increase of probability of adhesion from scaffold 1 to 4 can be seen throughout the contour plots presented in first two columns. In addition, cells adhere to scaffold 1 to 4 with nearly increasing strength. This can be seen in the shift of the average value of adhesion distribution, i.e. in the shift of distribution maximum toward higher strengths (from 2 to 3). An increase of adhesion strength on scaffolds 3 and 4 compared to the one on scaffolds 1 and 2, where the majority of cells did not establish strong attachment sites yet in the measured time window of a few to 10 s is indicated by the arrows. Weak attachment on the latter scaffolds means that few bonds are formed during the few seconds contact and potentially, binding is to some extent governed through membrane tethers. Still, scaffold 2 was identified with slightly wider distribution compared to scaffold 1, indicating more probable strong adhesion. On the other hand, the average adhesion strength on scaffold 3 and especially on scaffold 4 indicates that the majority of cells were able to establish strong attachment sites during this short time of contact, with more than just a few bonds (Table 6). The deficiency of serum proteins in PBS did not significantly modify cell adhesion as confirmed by statistical analysis (a slight time delay of adhesion when measuring in PBS cannot be confirmed as significant due to too low statistics in the acquired time range). This indicates that serum proteins do not impact the initial contact time and strength during the

first few to ten seconds of adhesion, which is shown to be crucial for establishing first strong contacts. This finding is in accordance with some previous studies, where no significant effect of the presence of serum proteins was observed on cell growth on different polymer materials (160). The latter can be explained either by the weak protein adsorption onto the highly hydrophilic surface of the scaffolds used in our study or by the barely changed scaffold surface by serum protein adsorption (161).
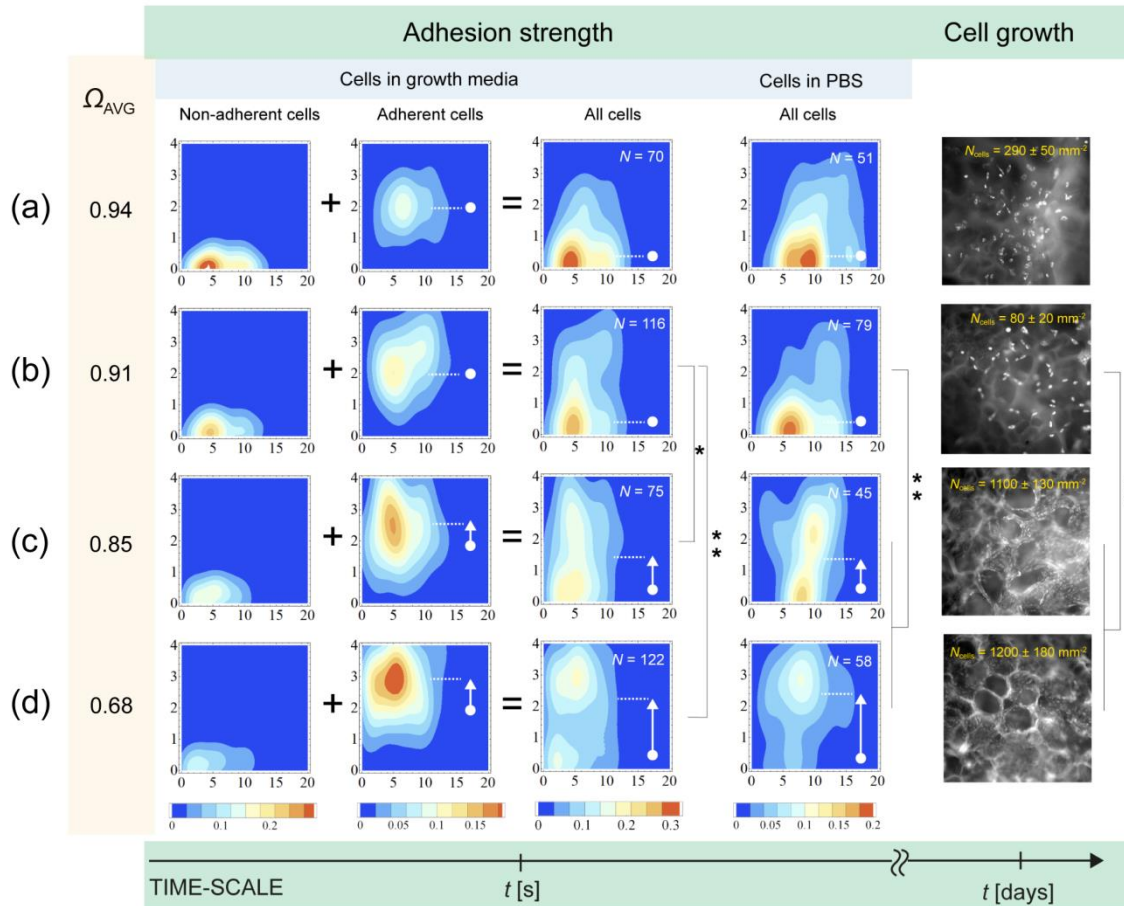
Figure 8.6. Distributions of cell adhesion on the surfaces of scaffolds 1−4 (a−d) measured in different media (first four columns) and the comparison with cell growth (fifth column). On the left side, the corresponding average free rotational space Ω_{AVG} calculated from polymer molecular mobility is presented for the comparison. Adhesions strength was characterized with 0−4 (y-axis) after the contact time 0−20 s (x-axis). Distributions represented with contour plots were normalized to the number of analyzed cell adhesion events, with their number shown in the upper right corners. Besides, the increase of the average adhesion strength from the one on scaffolds with the lowest adhesion is depicted with white arrows. Raw data of cell adhesion events shown in Figures C.1. and C.2. in the Appendix was correlated pairwise using statistical analysis with (*) $P = 0.01$ and (**) $P = 0.001$.

To summarize, cell adhesion analysis in the first seconds showed good correlation with cell growth during the first week of culture. The fact that the majority of the adhesion events established binding forces stronger than 200 pN in about 5s can additionally indicate how first-seconds time-scale binding events determine the initial cell growth. According to the results, it is reasonably to say that the differences in cell adhesion and followed cell growth

between scaffolds could be a consequence of the differences in polymer molecular mobility. More efficient cell adhesion was shown on scaffolds with the lower calculated average free rotational space of polymers Ω_{AVG} (Figure 8.6, left). This result directly indicates that polymer molecular mobility, which was found to influence cell growth (first part of the study), has the most pronounced effect right during the process of cell adhesion.

To understand the relationship between adhesion dynamics and cell growth more thoroughly, additional analysis of dynamic manipulation with OT was implemented. Beside the measurements of adhesion strength after particular time of the contact through which we estimated the number of bonds (Table 6), real-time dynamics of bonds formation was measured by dynamic OT manipulation of adherent cells as well (Figure 6.5b). Cells were moved by periodical sequential optical trapping parallel to the scaffold surface, where the amplitude of cell displacement was measured in real-time. Time dependent cell displacement was then related to the time dependent number of bonds, and the last transformed into the rate of bond formation (Figure 8.7). By such manipulation, conditions analogous to the ones *in vivo* were mimicked, where cells in a shear flow adhere dynamically employing their rolling mechanism on adhesive surfaces (156,157,162). Adhesion dynamics is thus not dependent just on the rate of receptor−ligand binding (k_{on}), their concentrations and their diffusion in the contact area as in the previous case, where adhesion strength was measured after static contact, but also on the considerable detachment rate (k_{off}) induced by the external force (136,137). In our case, this was induced by OT with the force loading rate dependent on the attachment scenario (Figure 8.4) and maximum force of approximately 200 pN (trap positioned close to the cell membrane).

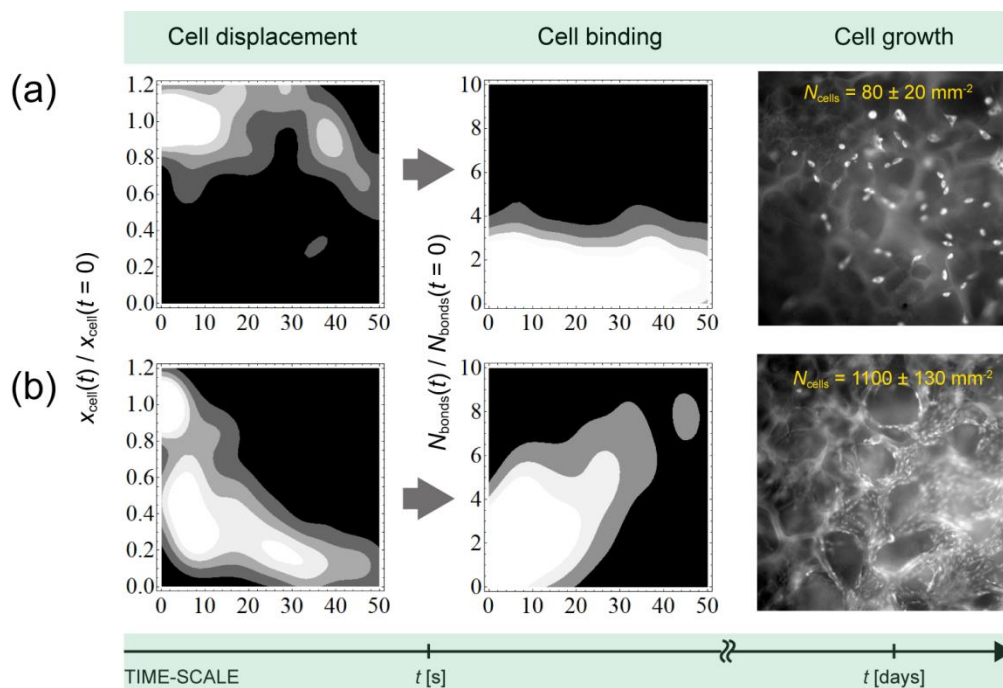**Figure 8.7.** Dynamics of cell displacement normalized to the initial value at time $t = 0$ (first column) and bond formation rate (second column) on the surfaces of scaffolds 2 (a) and 3 (b). The corresponding cell growth is shown in the third column. A higher density of data points is seen as brighter regions. The analysis on scaffolds 2 and 3 was obtained from 7 and 14 cell adhesion kinetics analysis, respectively.

The time dependent cell displacement and bond number evolution was analyzed on scaffolds 2 and 3, characterized with significantly different cell growth (Figure 8.3), to check if such analysis can also support different cell growth on scaffolds. Distribution of adhesion dynamics was again obtained with Gaussian representation of data (Equation 3 and Figure 8.5) with the variances defined by measurement errors ($\sigma_t = 3$ s, $\sigma_{Disp} = 0.1$ and $\sigma_{Bonds} = 1$). Amplitude of cell displacement was normalized to the initial value which was 4.8 ± 3.0 μm for scaffold 2 and 3.7 ± 2.8 μm for scaffold 3, indicating that the majority of analyzed cells on scaffold 3 was characterized with strong adhesion not being able to break the initial contact, while approximately half of the analyzed cells on scaffold 2 were characterized with low adhesion with thus lower ability of bond formation. Indeed, cell displacement shows remarkable difference between scaffold 2 and 3. On the time scale of 10 s to 1 min, the adhesion strength (number of bonds) is approximately 5 times larger in the case of scaffold 3 than in the case of scaffold 2. Since the analysed binding dynamics shows the competition between attachment and detachment rates, k_{on} and k_{off} respectively, one quickly notices that k_{on} prevails over k_{off} on more biocompatible scaffold 3 even though the external force is constantly induced, endeavoring to break bonds (137) or to drastically decrease lifetime of bonds (136). On less biocompatible scaffold 2, k_{on} and k_{off} seem to be of similar value. To sum up, the OT analysis revealed that the cell adhesion forces much stronger than 200 pN can build up in the first few seconds. The results could serve to identify the scaffolds suitable for efficient initial cell growth, a few orders of magnitude slower process.

8.5 Measuring the potential changes of the local physical properties at the cell attachment site by fluorescence microspectroscopy

During the cell attachment, other physical processes beside the receptor-ligand binding dynamics can be investigated. Physical properties which can change at the interface right after adhesion is the restructuring of membrane proteins and lipids (163), which eventually lead to the protein clustering and formation of focal adhesions. This physical changes on the interface effect also on the alterations in the local membrane fluidity (164), charge, polarity (165), etc. In order to be able to measure these changes, advanced experimental methods with high local molecular sensitivity must be applied. One of them is the fluorescence microspectroscopy developed in our laboratory (101), where the physical changes in the membrane can in theory be detected through membrane incorporated environmental sensitive fluorescent probes (166). For example, higher local polarity in the membrane can be detected through the red shift in the spectra, which is the consequence of the decreased difference in the energies of the fluorophore ground and excited state due to higher dipole-dipole interaction with the environment. Polarity can be increased by hydration of the outer membrane region (167).

In our experiment, cell membranes were labelled with environmental sensitive fatty-acid probe SPP268 (Figure 4.1) just prior FMS spectral analysis. The accurate spectra acquired in each image pixel were obtained by subtracting the background of the surrounding fluorescent signal. We searched for the potential differences in the probe spectral peak position (λ_{max}) and photobleaching (b) between the parts of the cell plasma membrane, one in direct contact with the scaffold surface and other, outside the interface region. Significant differences were observed in λ_{max} throughout the plasma membrane, while b didn't change considerably (Figure 8.8b and Figure 8.8c, respectively). However, it is difficult conclude that the red shift (denoted with asterisk) is in those parts of the membrane, which form the first adhesion sites with the scaffold surface. The optical resolution is limited by the optical diffraction limit, which is approximately 200 nm and is thus difficult to determine the exact position of the adhesion sites.

Average spectral peak position in the membrane was measured λ_{max} = 534nm ± 1nm, both on the contact with the scaffold (green dashed line) and outside (blue dashed line), while locally, the 4 nm red shift was measured. The shift indicates that the probe has good sensitivity to distinguish between different local physical properties in the surroundings, such as the polarity gradients. However, it is difficult to determine the exact cause of the spectral shift since the very likely strong local electric fields in the membrane produced by the ordered charges and dipoles can as well change the energy profile of the fluorophore electronic transitions and thus the emitted spectra (102). There could be other physical causes for the red shift, which are in our case less significant but has to be considered in such analyses. One is that red-shift can be detected also when dye-dye interaction is present at high fluorophore density. Since the fluorescence intensity throughout the plasma membrane which correlates with fluorophore density (Figure 8.8a) is not the entirely correlated with the red shift distribution (Figure 8.8b), this effect could be neglected. On the other side, photobleaching doesn't change throughout the plasma membrane, but

significantly increases inside the cell. This indicates on different physical properties of the intracellular membranes and the plasma membrane.

To conclude, the results suggest that the local physical changes in the plasma membrane can be measured using this particular environmental sensitive membrane probe SPP268 with NBD attached. However, it is difficult to conclude that the spectral changes are measured exactly on the adhesion sites and thus more analysis should be performed including the usage of the other potentially more membrane environmental sensitive probes.
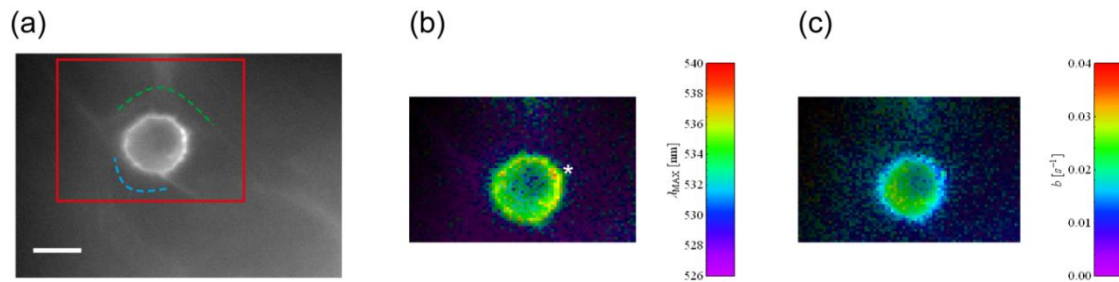
Figure 8.8. FMS spectral analysis of the cell attached to the scaffold surface. (a) Fluorescence microscopy image of the cell, where the first adhesion sites are formed on the upper half of the membrane (green dashed line). (b) Fluorescence microspectroscopy image with the contrast on the spectral peak position λ_{max}. (c) Fluorescence microspectroscopy image with the contrast on the photobleaching b. Cells were stained with the SPP268 probe (Figure 4.1) just prior spectral analysis and after cell adhesion. The part of the plasma membrane with the maximal spectral red shift is presented with asterisk. The scale bar is 10 μm.

9 Scientific contribution

The research was primarily focused to elucidate how different physical properties of polymer scaffolds measured on various scales influence on cell response and how they are correlated. This approach presents one of the new strategies to better understand initial cell-biomaterial interaction or more generally to better understand the mechanism of biocompatibility. By the comprehensive study of scaffolds physical properties, from its morphology, mechanical properties to the polymer molecular mobility, which was conducted for the first time in this research field, we were able to define the parameter influencing the initial cell growth measured on gelatin scaffolds the most. The latter, polymer side chain molecular mobility was shown the best correlation with cell growth, while scaffold mechanical properties seem to have an effect, but the contradicting results imply to the further investigations. Polymer molecular mobility should therefore be considered in scaffold biocompatibility studies. For instance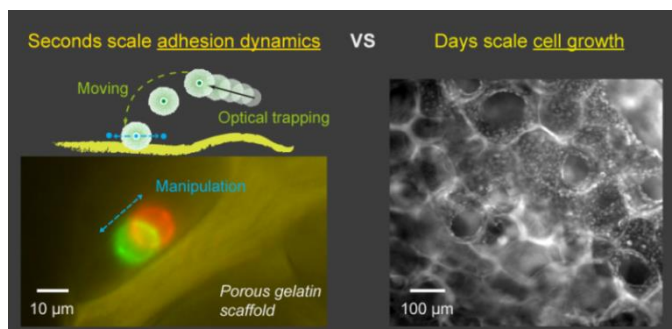, knowing the exact mobility in addition to the known, e.g. surface chemical structure or surface modification, could importantly contribute to the current understanding of the processes on the material-cell interface.
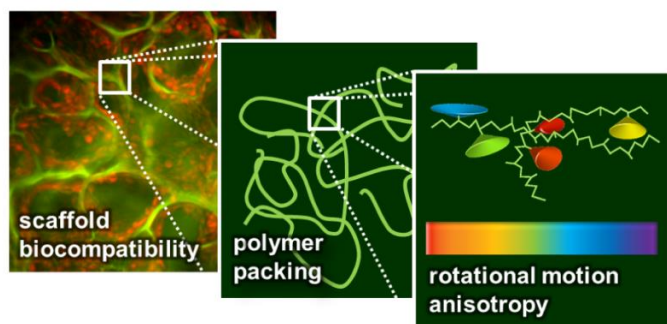
Since the differences in cell response were shown during the first days of culture, our next aim was to understand the cell-scaffold interface right from the initial contact, when the first attachment sites are formed. The study was performed with the system of optical tweezers used for controlled cell manipulation and confocal fluorescence microscopy used for accurate submicron scale detection. We have developed cell adhesion analysis technique with the quantitative characterization of the adhesion strength, adhesion probability and adhesion dynamics during the first minute of the contact. It was found that cell adhesion measured throughout the first seconds correlates with cell growth measured throughout the first days of culture and that cell adhesion could be governed by polymer molecular mobility. This indicates that first seconds of the contact can markedly direct further cell response. By FMS, physical changes in the local plasma membrane at the interface were further measured, but no significant change was detected. It indicates on negligible membrane restructuring or the lack of method sensitivity and thus, further investigations are needed. To summarize, the experimental technique applied on 3D scaffold surfaces can represent a novel approach in gathering the essential information on initial cell−scaffold surface dynamics and more importantly could serve to predict scaffold biocompatibility.

10 Razširjen povzetek v slovenskem jeziku

Uvod

Področje raziskav tkivno-inženirskih nadomestkov oz. nosilcev je v zadnjih letih doživelo velik razcvet. Za učinkovito uporabo pri večjih poškodbah tkiv je potrebno dobro razumeti njihove fizikalne in biokemijske lastnosti ter na drugi strani odziv posameznih celic in celotnega tarčnega tkiva. Z eno besedo, cilj tako laboratorijskih kot tudi kliničnih testov je izboljšava biokompatibilnosti nosilcev sestavljenih iz različnih biomaterialov, ki bi vodila do učinkovite uporabe za regeneracijo posameznih tkiv (2). Zaradi kompleksnosti bioloških sistemov razumevanje biokompatibilnosti še ni dovolj dobro raziskano zato so študije vpliva različnih lastnosti nosilcev in samih materialov na odziv celic nujno potrebne. V doktorski disertaciji smo zato proučevali vpliv različnih fizikalnih lastnosti nosilcev iz naravnih materialov na pritrjevanje in rast celic. Nato smo z naprednimi eksperimentalnimi tehnikami proučevali dinamiko pritrjevanja celic v realnem času s simuliranjem pogojev biološkega sistema, saj je lahko prav slednja pomembna za nadaljnji odziv celic, torej njihovo rast, migracijo in ustrezno diferenciacijo. Ustrezen odziv celic v mehansko in strukturno primernem nosilcu, pa je pogoj za uspešno klinično aplikacijo.

Biomateriali in tkivno inženirstvo

Pri razvoju tkivno-inženirskih nosilcev so poleg raziskav različnih načinov in postopkov priprave pomembne tudi raziskave materialov, ki so lahko naravnega ali sintetičnega izvora. Med najpogostejše naravne polimere štejemo: kolagen, želatino, hitosan, hialuronsko kislino, agarozo, svilo in kombinacijo polimerov pridobljenih z decelularizacijo tkiv (6). Med najuporabnejše sintetične polimere štejemo razne poliestre, poliuretane, polikarbonate, polianhidride, idr (7). Prednost naravnih materialov je večja biokompatibilnost, prednost sintetičnih pa ustreznejša mehanska stabilnost in biorazgradljivost. Za doseganje čim večje učinkovitosti pri regeneraciji poškodovanih tkiv, pa morajo vsi čim bolj ustrezati naslednjim strukturnim in funkcionalnim pogojem:

- mehanska primernost in stabilnost,
- porozna, prepletena in dobra difuzivna struktura,
- primerne biokemijske in fizikalne lastnosti površine na molekularni skali,
- primerna dinamika biorazgradljivosti,
- minimalen imunski odziv v telesu, idr.

Za doseganje omenjenih lastnosti poznamo več metod priprave 3D nosilcev (8). 3D porozne strukture lahko dosežemo z mešanjem in raztapljanjem polimerov v organskih topilih, fazno separacijo polimerov in liofilizacijo (9–11) ter bolj naprednimi metodami kot so mikro- in nano- strukturiranje polimernih mrež s pomočjo elektrostatične sile, 3D tiska, laserskega sintranja, foto-polimerizacije, ipd. (13). Poleg tega lahko visoko funkcionalnost

dosežemo z metodo kemijskega zamreževanja polimerov (16), v zadnjih letih pa tudi z metodo decelularizacije tkiv, kjer pridobimo strukturo iz ohranjenega naravnega ECM (18).

Biokompatibilnost

Zaradi vse večjih potreb po bolj usmerjenih in tarčnih zdravljenjih poškodovanih tkiv se razvijajo novi materiali in nove tehnike, kjer morajo nosilci izražati tako primerno mehansko, kemijsko kot tudi biološko aktivnost. To še vedno predstavlja velik problem, zato se velik del raziskav posveča študijam vpliva različnih biokemijskih in fizikalnih lastnosti pripravljenih materialov na odziv celic kot so njihovo pritrjevanje, proliferacija, rast, morfologija, izražanje fenotipa, ipd. Na Slika 1 je shematski prikaz, kjer proučevane lastnosti lahko razdelimo v tri kategorije.

Kljub mnogim že dobro raziskanim vplivom materialov na odziv celic (34–36) še vedno obstaja veliko nerešenih vprašanj povezanih z biokompatibilnostjo. Potrebujemo nove koncepte raziskav. Enega izmed njih predstavljamo v doktorski disertaciji, v kateri koreliramo odziv celic s fizikalnimi lastnostmi materiala na več velikostnih skalah iz vseh treh kategorij prikazanih na Slika 1.
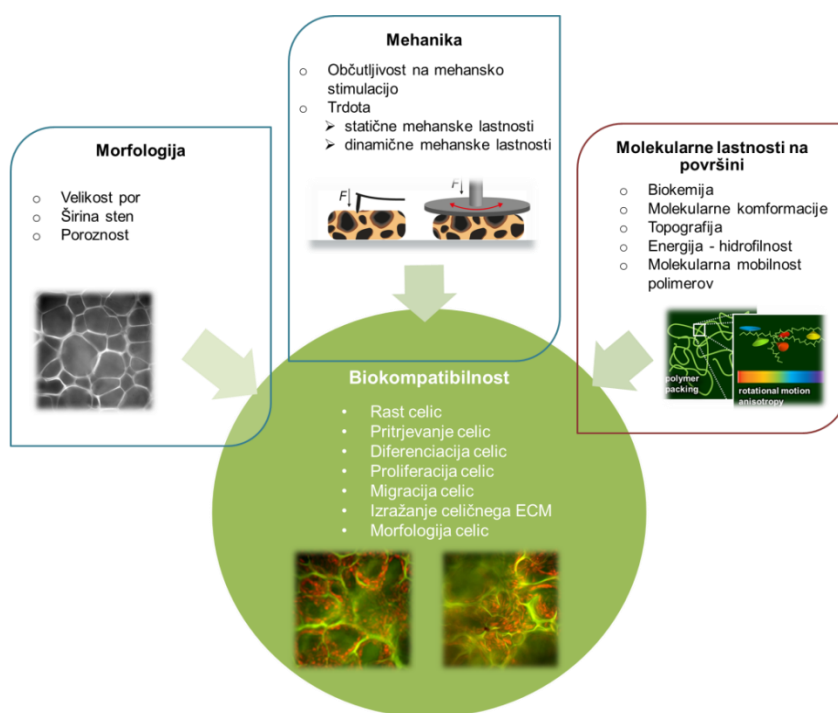

Slika 1. Shematski pregled raziskav lastnosti materialov in njihovega vpliva na odziv celic za študij in razumevanje biokompatibilnosti. V doktorski disertaciji smo raziskovali vpliv tako morfologije, mehanike kot tudi molekularnih fizikalnih lastnosti na pritrjevanje in rast celic s poudarkom na študiji molekularne mobilnosti polimerov.

Stik celice z materialom

Raziskave procesov na stiku celice z materialom od prvega kontakta naprej so za razumevanje nadaljnjega celičnega odziva izredno pomembne. Začetni kontakt, pri katerem se tvorijo pretežno nespecifične vezi med membranskimi proteini integrini in ekstracelularnim matriksom, vodi do nastanka fokalnih transmembranskih proteinskih kompleksov, ki sprožijo mehansko transdukcijo signala v celico in pretvorbo v celične signalne poti, ki določajo končni odziv celic (62,71).

Poznamo več metod in tehnik proučevanja interakcije z različnim časovnim in »prostorskim« oknom detekcije ter različno občutljivostjo. Za kvantitativen opis interakcije po navadi merimo sile tekom pritrjevanja. Na Slika 2 je grafični prikaz najpomembnejših eksperimentalnih metod, ki se uporabljajo za tovrstne študije. V zadnjem obdobju je velik poudarek na metodah, s katerimi merimo interakcijo v realnem času pri čim bolj realnih pogojih in pri čim večji občutljivosti, ki gre do molekularne skale. Najpogostejši metodi sta spektroskopija sil posameznih celic na sistemu mikroskopa na atomsko silo (AFM) (79) ter manipulacija in merjenje sil posameznih celic z optično pinceto (80). Vsaka ima določene prednosti in slabosti (Slika 2, bolj podrobno v poglavju 2.2.1.), za naše potrebe pa smo v doktorski disertaciji uporabili optično pinceto vgrajeno na sistem konfokalnega fluorescenčnega mikroskopa (90–92). Poleg omenjenih metod se v zadnjem času razvijajo tudi metode, ki omogočajo detekcijo posameznih molekularnih dogodkov (nastanka vezi) na začetnem stiku celice in materiala (na shemi označeno z zeleno), a je sama izvedba za zdaj še zahtevna.
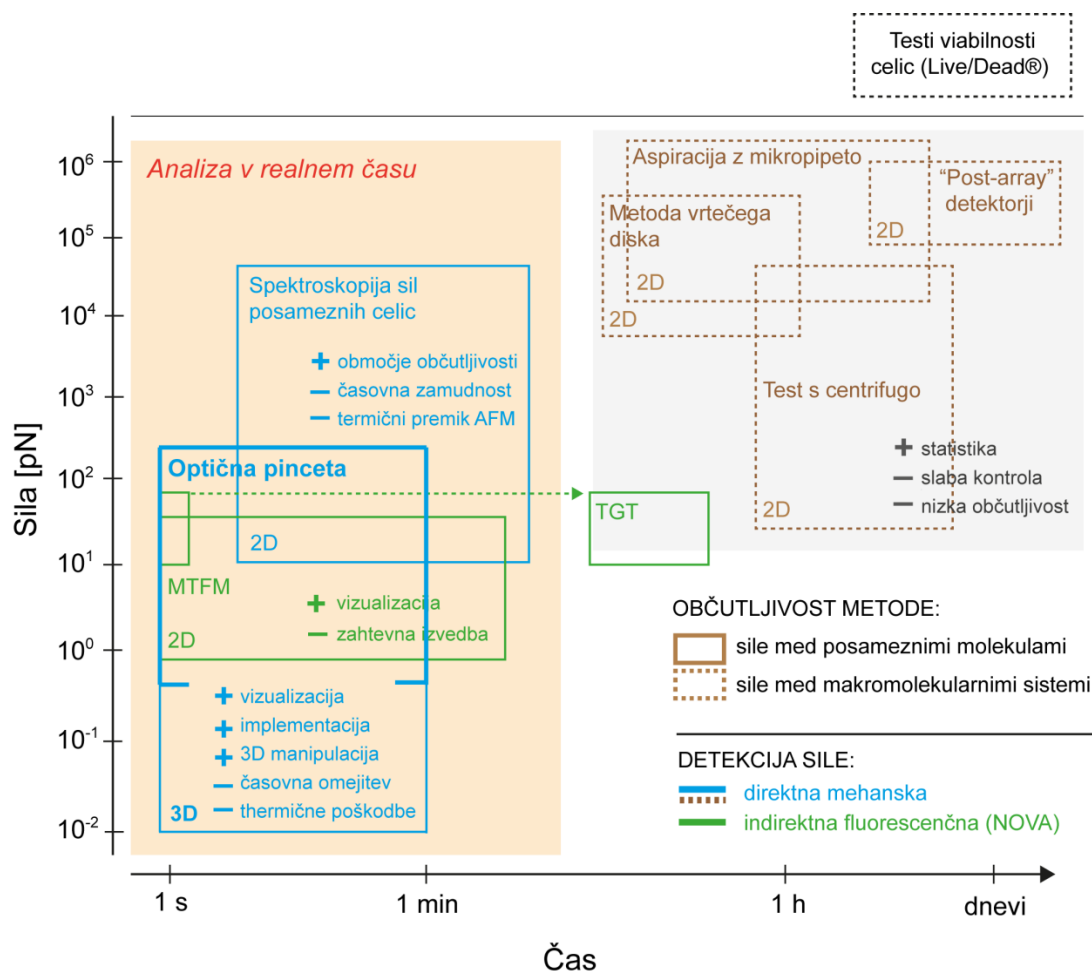
Slika 2. Primerjava metod za karakterizacijo pritrjevanja celic na material. Razlikujejo se v časovnem oknu detekcije po samem stiku, občutljivosti, načinu kvantitativne detekcije sile in pa v možnosti/nezmožnosti analize v realnem času. Sistem optične pincete, ki smo ga uporabili v doktorski disertaciji, omogoča analizo v realnem času in realnih pogojih ter občutljivostjo detekcije sil do pN v 2D s 3D kontrolo položaja.

Cilji doktorske disertacije

Cilj doktorske disertacije je bil raziskati vidike biokompatibilnosti biopolimernih nosilcev z vpeljavo novih konceptov in tehnik karakterizacije fizikalnih lastnosti nosilcev na več velikostnih skalah in njihove korelacije z odzivom celic. Poleg tega je bil cilj raziskati tudi interakcijo celic s površino različnih nosilcev z merjenjem dinamike pritrjevanja z optično pinceto v realnem času. Namen je bil vpeljati tudi nove koncepte karakterizacije in analize interakcije ter rezultate ustrezno opredeliti iz vidika lastnosti materiala in po drugi strani z vplivom na biokompatibilnost.

Za bolj podrobno in sistematično opredelitev ciljev doktorske disertacije in izbranih implementiranih tehnik, glej poglavje 3.

Priprava nosilcev

Nosilce smo pripravili iz naravnega polimera želatine raztopljene v različnih pufrih in z metodo hkratnega zamrzovanja in kemijskega premreževanja uspeli narediti porozno in mehansko stabilno 3D strukturo. Za pripravo strukturno in mehansko stabilnih nosilcev z različnimi fizikalnimi lastnostmi smo tekem priprave ustrezno spreminjali pH, ki vpliva na stopnjo kemijskega premreženja, koncentracijo kemijskega zamreževalca EDC/NHS, ki vpliva na število novonastalih amidnih vezi v strukturi polimerov in posledično končne mehanske lastnosti, ter temperaturo in čas priprave, ki vplivata tako na končno strukturo kot tudi na mehanske lastnosti. Tekom priprave smo za potrebe nadaljnje karakterizacije nosilcev stranske verige polimerov kovalentno označili s fluorescenčnim (FITC) in spinskim označevalcem (3-maleimido PROXYL) (104,105). Za natančno kontrolo premreževanja in 3D poroznega strukturiranja smo vse komponente injicirali direktno na hladilno ploščo z nastavljivim časovnim temperaturnim profilom. Podrobnejši opis priprave najdete v poglavju 4.2.

Poleg nosilcev iz naravnih polimerov smo pripravili tudi sintetične sestavljene iz poliuretanov. Uporabili smo metodo temperaturne fazne separacije in nazadnje kemijske modifikacije površin s plazemsko obdelavo. Podrobnejši opis priprave najdete v poglavju 4.3.
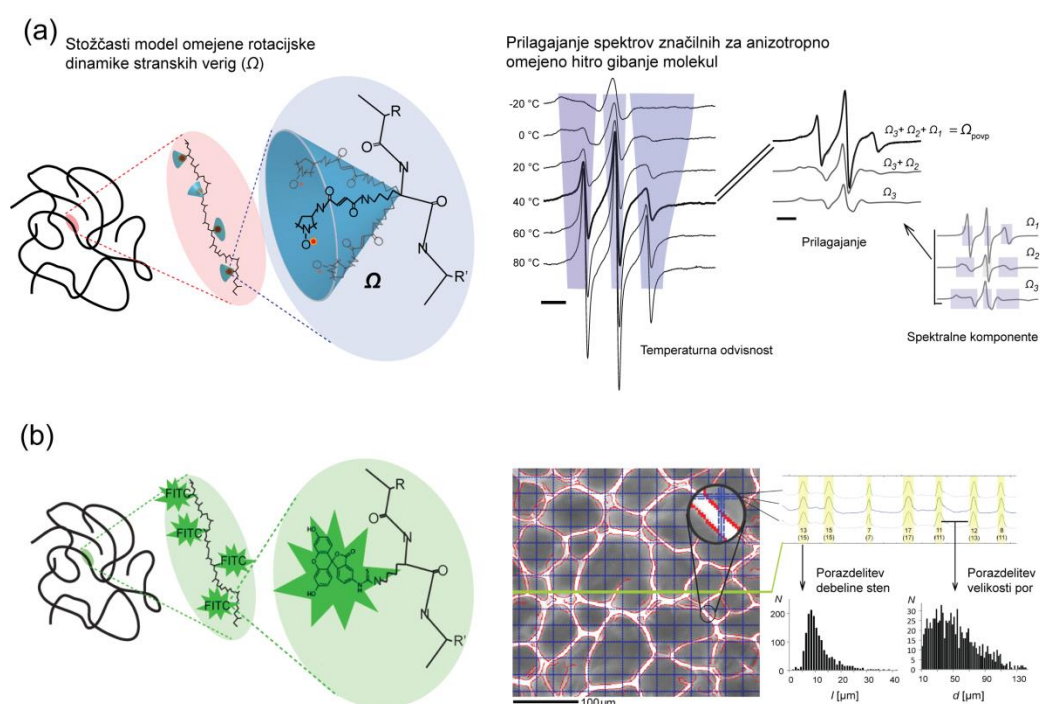
Lastnosti nosilcev

Merili smo fizikalne lastnosti pripravljenih nosilcev na več velikostnih skalah, od strukture, morfologije in mehanskih lastnosti na makro skali do mobilnosti stranskih verig polimerov na molekularni skali. Uporabili smo napredne eksperimentalne tehnike in analize, poleg tega pa smo vzorce pred tem morali za potrebe detekcije ustrezno modificirati.

Molekularno mobilnost stranskih verig polimerov smo merili z elektronsko paramagnetno resonanco (EPR), ki izkorišča absorpcijo elektromagnetnega polja na nesparjenih elektronih in kjer energijski absorpcijski spekter mogoča analiza mobilnosti verig na molekularni skali (99,110,113). Za potrebe detekcije smo zato na stranske verige kovalentno vezali spinski označevalec z nitroksidno skupino z nesparenim elektronom, preko katerega smo merili lastnosti mobilnosti oz. konformacijske dinamike verig v neposredni okolici (Slika 3a). V primeru zaprte strukture proteinov je rotacijska dinamika stranskih verig bolj omejena in anizotropna, pri odprti strukturi pa ravno obratno in se kaže v obliki spektrov. Za meritve smo uporabili X-pasovni spektrometer z mikrovalovno frekvenco vzbujanja prehodov med elektronskimi stanji in magnetnim poljem reda nekaj desetink Tesla. Za spektralno analizo mobilnosti - anizotropije rotacijske dinamike stranskih verig - smo uporabili spektralne simulacije, razvite v našem laboratoriju, in so podrobno opisane v literaturi (111,112). V simulacijah smo izmerjeni spekter prilagajali z modelnim spektrom, ki je lahko sestavljen iz več posameznih spektralnih komponent, ki predstavljajo posamezne konformacijske domene v strukturi vzorca (Slika 3a). Posamezna komponenta je definirana s spektralnimi parametri, kot so parameter urejenosti S, rotacijski korelacijski čas molekul τ_c, popravek zaradi polarnosti okolice p_A, prosti rotacijski prostor opletanja molekul

Ω, definiran s kotoma θ in φ, ipd (111). Slednjega smo uporabili pri analizi molekularne mobilnosti stranskih verig polimerov. Bolj podrobno razlago analize najdete v poglavju 5.1.

Za natančno karakterizacijo strukture in poroznosti nosilcev s konfokalno fluorescenčno mikroskopijo, smo stranske verige polimerov pred pripravo nosilca kovalentno označili s fluorescentnim označevalcem FITC (Slika 3b). Na podlagi dobrega kontrasta smo nato natančno okarakterizirali porazdelitev velikosti por in širine sten v strukturi. Podrobnejši opis najdete v poglavju 5.2. Mehanske lastnosti smo merili z več metodami: reometrijo, dinamično mehansko analizo (DMA) ter nanoindentacijo na mikroskopu na atomsko silo (AFM). Na ta način smo uporabili različne načine mehanskega stresa na različnih velikostnih skalah in tako dobili bolj pregledno informacijo o odziva materiala. Za analizo elastičnih modulov smo uporabili različne empirične modele (več v poglavju 5.3.).

Slika 3. Analiza molekularne mobilnosti stranskih verig polimerov z metodo spinskega označevanja in EPR spektroskopije (a); analiza strukture poroznosti nosilcev na mikrometrski skali z metodo fluorescenčnega označevanja in konfokalne fluorescenčne mikroskopije (b).

Lastnosti interakcije celic z nosilci

Za študij interakcije celic z nosilci in študij vpliva fizikalnih lastnosti nosilcev na odziv celic smo morali tako celice kot tudi nosilce ustrezno pripraviti. Izbrali smo celice mišjih fibroblastov (L929), ki so dober modelni sistem, saj igrajo pomembno vlogo v vezivnih tkivih in pri ohranjanju strukturne celovitosti izločajo proteine zunajceličnega matriksa. Odziv celic smo merili tako, da smo gosto suspenzijo najprej nanesli na površino steriliziranih nosilcev ustrezne dimenzije in nato v prvem tednu merili rast celic s fluorescenčno mikroskopijo in s testom viabilnosti. Za meritev rasti s fluorescenčno mikroskopijo na 10x povečavi smo celice na nosilcih najprej označili z membranskim fluorescenčnim označevalcem SPP158 (sodelovanje s Fakulteto za farmacijo, Univerza v Ljubljani) ter na podlagi svetlobnega kontrasta slike ocenili število celic na enoto površine nosilca (več v poglavjih 6.2. in 6.3.). Za meritev viabilnosti smo uporabili test presnovne aktivnosti celic.

Princip optične pincete in eksperimentalni sistem

Za meritve pritrjevanja celic na površino nosilcev v realnem času in pri kar se da fizioloških pogojih smo uporabili optično pinceto za manipulacijo (Tweez 200si, Aresis) in konfokalno fluorescenčno mikroskopijo za detekcijo na invertnem mikroskopu (Nikon Eclipse TE 2000-E). Eksperimentalni sistem z vsemi pomembnimi komponentami je shematsko prikazan na Slika 4b. Najprej pa na kratko razložimo princip delovanja optične pincete.

Kljub spoznanjem v 19. stoletju, da svetloba na delce deluje s silo, velja za očeta optične pincete Arthur Ashkin, ki je kot prvi leta 1970 natančno opisal tehniku ujetja mikrometrskih dielektričnih delcev v fokusiranem laserskem snopu ter jo v kasnejših letih uporabil za proučevanje bioloških sistemov (120). Metoda izkorišča razliko v lomnih količnikih ujetega dielektričnega delca in okoliškega medija, ki privede do loma fokusirane svetlobe. Zaradi ohranitve gibalne količine svetlobe in Gaussovega profila laserskega snopa rezultanta sil na delec vedno kaže v smeri gorišča (Slika 4a). Sila na delec je odvisna od moči laserja, razlike v lomnih količnikih, optike ter velikosti dielektričnega delca. Velikost delca pa tudi pogojuje režim interakcije. V primeru polmera delca $r >> \lambda$ sistem dobro opišemo z geometrijsko optiko, medtem ko pri $r << \lambda$ obravnavamo delec kot točkasti dipol. Vmesno področje velikosti, kamor spada tudi večina proučevanih bioloških sistemov, najbolje opišemo z ustrezno kombinacijo režimov in so za to potrebni natančni teoretični modeli (124,125). Več v poglavju 6.4.1.

Za kvantitativno meritev sil najprej potrebujemo kalibracijo optične pincete. Obstaja več metod in jih tu samo naštejemo. Maksimalno silo na delec po navadi merimo z *metodo izstopne sile* (126), kjer velja linearni zakon upora (Stokesov zakon). Konstanto elastičnosti pasti k_{past} pa lahko izmerimo z opazovanjem Brownovega gibanja delca v harmonskem potencialu pasti (88), preko energijskega spektra fluktuacij, ki tudi temelji na Brownovem gibanju (85) ali pa s hitrim sledenjem delca tekom prehoda v past (128).
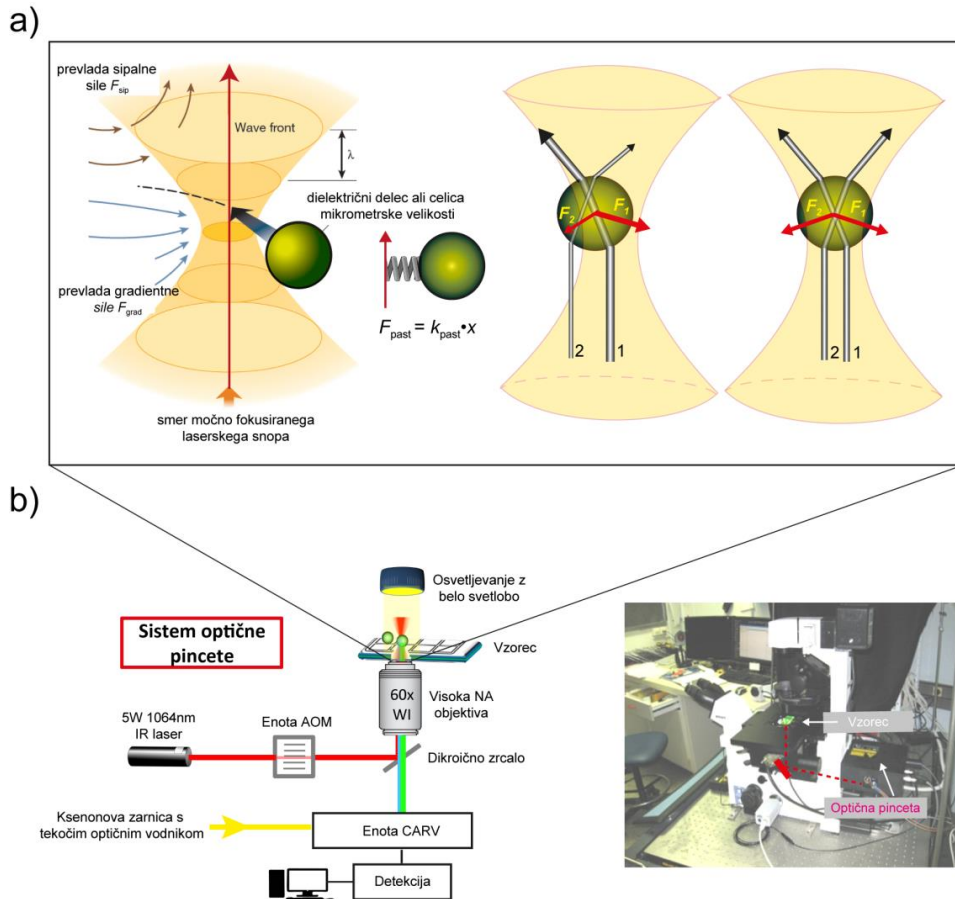
Slika 4. Shematski prikaz delovanja optične pincete, kjer blizu gorišča močno fokusiranega laserskega snopa prevlada gradientna sila nad sipalno silo, in se delec ujame v past (a). Ker ima laserski snop Gaussov profil, je intenziteta na mestu označenem z 1 večja od intenzitete na mestu 2 in rezultanta sil, kot posledica ohranitve gibalne količine svetlobe, vedno kaže v smeri gorišča. Shema optičnega sistema in postavitev na mikroskopu (b). Bistvene komponente sistema so IR laser, akustooptična modulacija laserja (AOM), dikroična zrcala, vodno-imerzijski objektiv z visoko numerično aperturo in detekcijski sistem.

Meritve pritrjevanja celic in profila optične sile na celico

Po suspendiranju celic v merilni bazenček z nosilcem, fiksiran na mikroskopu, smo posamezne celice ujeli v optično past in jih z AOD sistemom premika položaja pasti v 2D prepeljali do neposrednega stika s površino nosilca (Slika 5). S statično in dinamično manipulacijo smo nato merili pritrditev in hitrost pritrjevanja celic v realnem času. Moč pritrditve smo merili preko amplitude premika pritrjene celice, pod vplivom sile optične pincete v smeri površine nosilca. Tekom eksperimenta smo morali biti pozorni na omejitev maksimalne moči pincete zaradi močnega lokalnega segrevanja v fokusu in tako morebitne termične poškodbe celic (132). Pri moči laserja $P = 500$ mW nam je uspelo pomeriti sile vse do 200 pN in pri tem zaznati minimalen učinek termičnega stresa. Natančen premik pritrjene celice z resolucijo pod 100 nm smo zaznali preko fluorescenčne detekcije fluorescenčno označene celice. Bolj podrobno razlago najdete v poglavju 6.4.3.
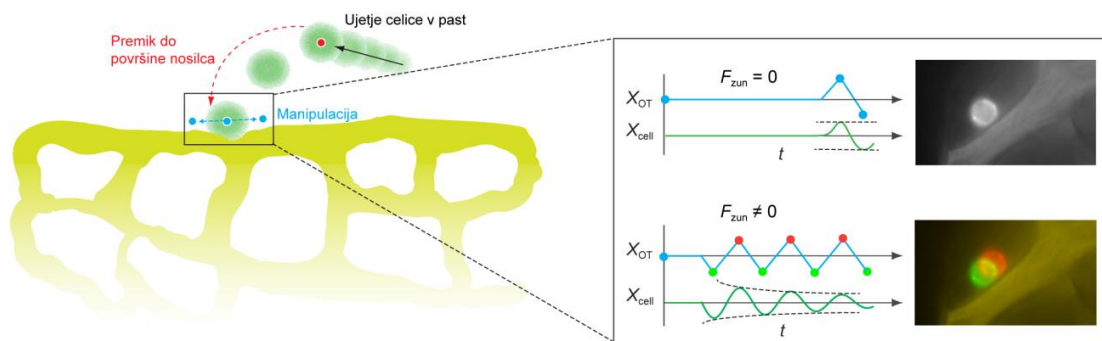
Slika 5. Shematski prikaz eksperimentalnega sistema študije pritrjevanja celic na površino nosilcev. Preko analize amplitude premika pritrjene celice pod vplivom sile optične pincete v smeri površine nosilca smo merili moč pritrditve po določenem času stika (zgoraj) in časovni potek pritrjevanja (spodaj).

Za kvantitativno analizo sil pri študiji pritrjevanja celic na površino nosilcev smo poleg izstopne sile merili tudi profil sile optične pincete pri prehodu skozi celico oz. elastično moč pasti k_{cel}. Uporabili smo več metod, od analize dinamike premika celice pod vplivom sekvenčne manipulacije z optično pinceto z uporabo natančne računalniške obdelave slik do analize premika celice v optično past. Natančno razlago najdete v poglavju 6.4.3.

Korelacija med fizikalnimi lastnostmi nosilcev in odzivom celic

V prvem delu doktorske študije smo raziskovali vpliv opisanih fizikalnih lastnosti želatinskih nosilcev na rast celic v prvih dneh. Najprej smo natančno okarakterizirali temperaturno odvisno molekularno mobilnost stranskih verig polimerov v strukturi različno pripravljenih nosilcev (med pripravo spreminjali pH in koncentracijo zamreževalca). Izmerili smo temperaturno območje faznega prehoda konformacijske dinamike polimerov $T_{f.pr.}$, to je oster prehod med anizotropnim in izotropnih gibanjem. Ugotovili smo, da $T_{f.pr.}$ narašča s koncentracijo zamreževalca in nižanjem pH v območju od pH 9.5 do pH 7.5. Zatem smo z opisano metodo konfokalne fluorescenčne mikroskopije natančno analizirali morfologijo nosilcev, kjer smo identificirali vpliv pH in koncentracije zamreževalca na velikost por in širino sten. Ugotovili smo, da pH močno vpliva na širino sten oz. na gostoto premreženja polimerov, medtem ko koncentracija zamreževalca bolj vpliva porazdelitev velikosti por. Nazadnje smo z reometrijo analizirali še mehanske lastnosti nosilcev, kjer smo merili viskoelastični strižni odziv na frekvenčno odvisen mehanski stres. Zaradi nehomogene strukture nosilca smo izmerili kompleksen odziv, ki smo ga ustrezno opisali z več-parametričnim generaliziranim Maxwellovim viskoelastičnim modelom (140). Več-parametrično analizo smo upravičili s tem, da smo vsak izračunan parameter relaksacijskega časa odziva materiala τ_i in pripadajočega strižnega modula G_i pripisali posamezni strukturni domeni v nehomogenem nosilcu. Ugotovili smo, da trdota nosilca, izmerjena preko G_i, narašča s koncentracijo zamreževalca, in da na mehanske lastnosti poleg morfologije vpliva tudi sama premreženost in strukturiranost mreže polimerov. Ta je odvisna od fizikalno-kemijskih procesov tekom priprave nosilca.

Izmerjene fizikalne lastnosti smo nazadnje uporabili za študij njihovega vpliva na rast celic. Na najmehkejšem nosilcu z največjo mobilnostjo stranskih verig polimerov smo izmerili nekajkrat slabšo rast kot na preostalih nosilcih (Slika 6). Natančneje smo analizirali korelacije in ugotovili, da je molekularna mobilnost stranskih verig tista fizikalna lastnost, ki najbolj vpliva na rast celic. Za dobro rast je morala biti povprečna mobilnost stranskih verig polimerov vsaj delno omejena (Ω_{povp} < 0.8), medtem ko pri bolj odprti strukturi (Ω_{povp} > 0.9), dobre rasti ni bilo zaznati (Ω_{max} = 1). Ker smo opazili razlike v rasti že tekom prvega dne, bi lahko na njih pomembno vplivalo pritrjevanje celic na nosilec. Na pritrjevanje pa bi lahko vplivala mobilnost polimerov, od katere je odvisno časovno okno za celice dostopnih prepoznanih vezavnih struktur ali konformacij polimerov na površini nosilca. Nadaljnjo študijo smo zato posvetili raziskavam dinamike pritrjevanja celic na površino različnih nosilcev v realnem času.
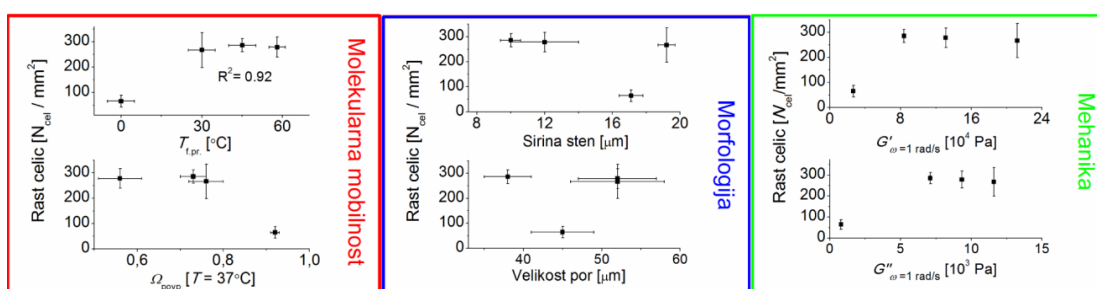
Slika 6. Iskanje korelacije med rastjo celic (*y* os) in različnimi fizikalnimi lastnostmi nosilcev *(x* os). *G'* in *G''* predstavljata elastični in plastični strižni modul pomerjen pri mehanskem stresu s frekvenco ω = 1 rad/s. Napaka na *y* osi je standardna deviacija rasti pomerjene na treh vzporednih vzorcih, medtem ko je napaka na *x* osi standardna deviacija treh (molekularna mobilnost) in 5-10 meritev (morfologija).

Ker smo opazili tudi korelacijo rasti celic z mehanskimi lastnostmi (Slika 6), smo pred študijo pritrjevanja celic nadaljnje raziskovali njihov vpliv. Uporabili smo nove metode karakterizacije: dinamično mehansko analizo in metodo nanoindentacije z mikroskopom na atomsko silo, ki meri trdoto materiala na manjši, mikroskopski skali, ki je bolj relevantna za celični odziv. Meritve smo izvedli na naravnih - želatinskih nosilcih ter na sintetičnih - poliuretanskih nosilcih. Pri meritvah nismo opazili signifikantne korelacije z rastjo celic. Podrobnejši opis najdete v poglavju 7.2.

Raziskava dinamike pritrjevanja celic na površino nosilcev z optično pinceto in detekcijo s fluorescenčno mikroskopijo

Cilj je bil bolje razumeti dinamiko pritrjevanja celic na tkivno inženirske polimerne materiale s kvantitativno analizo sil, ter kot nadaljevanje prejšnje študije razumeti vpliv mobilnosti polimerov na površini nosilca na pritrjevanje celic ter posredno na njihovo nadaljnjo rast. Za analizo smo uporabili sistem optične pincete in fluorescenčne detekcije.

Najprej smo izmerili mobilnost stranskih verig polimerov ter rast celic na različnih želatinskih nosilcih. Potrdili smo, da na rast celic mobilnost polimerov vpliva, kjer smo pri bolj ali manj odprti strukturi stranskih verig ($\Omega_{povp} > 0.9$) izmerili bistveno slabšo rast. Signifikantne razlike v rasti med različnimi nosilci smo opazili že tekom prvega dne, pri čemer je razmerje v rasti po enem tednu ostalo praktično nespremenjeno. To bi lahko potrjevalo našo hipotezo, da se največje razlike naredijo že tekom pritrjevanja celic na površino.

Načini pritrjevanja

Moč pritrditve smo merili z detekcijo amplitude premika pritrjene celice pod vplivom sile optične pincete vzdolž površine nosilca v različnih časih po stiku, od 1s pa do 20s. Preko analize premika celice v odvisnosti od sile, ki jo definira lega pincete glede na celico (Slika 7), smo razvrstili opažene načine pritrditve v tri razrede:

a) pri močni pritrditvi smo opazili le majhen premik celice pod vplivom največje sile pincete, $F_{OP} \sim 200$ pN, ko je ta na položaju blizu roba celice. Amplituda premika je sorazmerna z obratnim številom nastalih vezi N_{vezi} med celičnimi integrini in ligandi na površini. Primer analize močne pritrditve celice prikazujemo na spodnji shemi Slika 7. Natančen položaj optične pincete smo izmerili preko pojava dvofotonske absorpcije IR laserja in emisije v membranah vgrajenih fluorescenčnih molekul (bela pika), položaj celice pa preko optimiziranega slikovnega kontrasta;

b) pri šibki pritrditvi smo zaznali nekajkrat večji premik celice pod vplivom sile optične pincete. Prišlo je do cepitve manjšega skupnega števila nastalih vezi in nastanka novih, še preden bi celico uspeli odlepiti od površine. Amplituda premika je torej odvisna od obratne vrednosti hitrosti cepitve in nastajanja novih vezi;

c) pritrditev pa smo zaznali tudi preko membranskih tetrov izločenih iz zunanje celične membrane. Amplituda premika celice je v tem primeru odvisna od dolžine izločenih tetrov, ne pa toliko števila vezi. Prisotnost tetrov smo zaznali preko profila premika celice v odvisnosti od sile (vlečenje tetrov ima lastnost vzmeti (159)) ali preko fluorescence fluorescenčno označenih tetrov. Podroben opis izmerjenih načinov pritrditve najdete v poglavju 8.3.
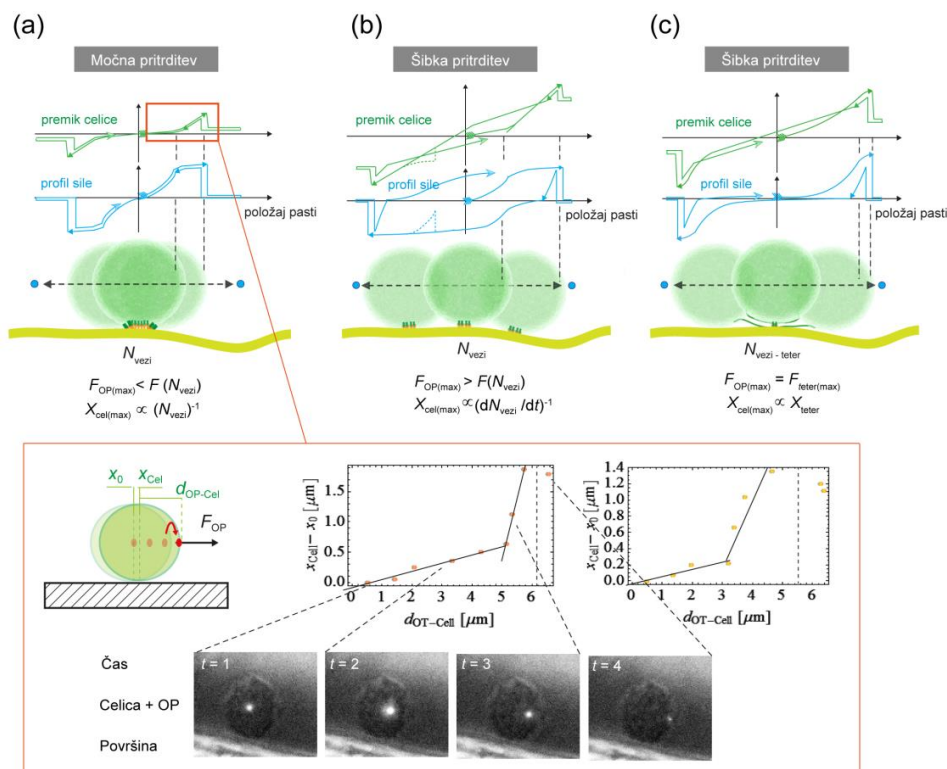
Slika 7. Izmerjeni načini pritrditve celice na površino nosilcev v času stika do 20s (a–c). Pri močni pritrditvi (a) smo zaznali le majhen premik celice (zelen graf) pod vplivom sile optične pincete (modra barva), ki je reda μm. Meritev in analizo premika močno pritrjene celice prikazuje spodnja shema. Pri šibki pritrditvi smo zaznali večji premik, kjer smo preko profila sile in profila premika ločili med dvema načinoma (b) in (c).

Vsako posamezno meritev pritrditve smo po moči razvrstili v 4 razrede (glej tabelo v poglavju 8.3.). Opisali smo jo z 2D Gaussovo funkcijo z variancama σ, ki ustrezata napaki meritve časa stika in moči pritrditve. S seštevkom vseh meritev in normalizacijo smo dobili verjetnostno porazdelitev moči pritrditve v odvisnosti od časa stika (Slika 8a). Takšna predstavitev rezultatov je najbolj ustrezna, saj zaradi kompleksnosti interakcije in uporabljene metode, ne moremo povsem ostro definirati moči pritrditve in tudi časa dejanskega stika.

Pritrjevanje celic korelira z rastjo celic

Moč pritrditve smo merili na različnih nosilcih in za analizo vpliva serumskih proteinov v različnih medijih: celičnem mediju DMEM obogatenim s serumom in PBS (Slika 8b). Izmerili smo, da pritrjevanje celic močno korelira z nadaljnjo rastjo celic, kjer smo na nosilcih z dobro rastjo (c in d) izmerili večjo povprečno moč pritrditve (označeno s puščicami), z bolj enakomerno porazdelitvijo. Porazdelitev moči pritrditve na površino manj biokompatibilnih nosilcev a in b je močno premaknjena proti nižjim vrednostim saj se velik delež celic v času stika ni uspel pritrditi oz. je bila sila optične pincete večja od sile pritrditve $F_{OP} > F(N_{vezi})$. Opazili smo, da se moč pritrditve v odvisnosti od časa stika ne razlikuje bistveno pri uporabi različnih medijev. Razlike med različnimi nosilci ostajajo praktično

nespremenjene. Serumski proteini tako ne vplivajo bistveno na pritrjevanje celic na želatinske nosilce.

Poleg meritve moči pritrditve celic po določenem času stika smo na nosilcih merili tudi dinamiko pritrjevanja. Po pritrditvi smo s periodično sekvenčno manipulacijo optične pincete na celico v smeri vzdolž površine nosilca v realnem času merili spremembo amplitude premika (Slika 5), ki je odvisna od števila vezi na samem stiku. Ocenili smo, da število vezi na biokompatibilnem nosilcu (c) v eni minuti povprečno naraste za 10 krat, medtem ko na manj biokompatibilnem nosilcu (b) do nastanka novih vezi ne pride. Pri takšnem načinu manipulacije, ki je analogen načinu pritrjevanja celic v strižnih tokovih *in vivo* sistemov (156,157), pomemben prispevek na dinamiko pritrjevanja poleg hitrosti nastajanja vezi k_{on} vpliva hitrost cepitve vezi k_{off} zaradi sile optične pincete (136,137). Ugotovili smo torej, da je na biokompatibilnih nosilcih pri izbranih pogojih, $k_{on} > k_{off,}$ medtem ko na preostalih, $k_{on} \leq k_{off}$. Bolj podrobno analizo najdete v poglavju 8.4.

Z razvito metodo analize pritrjevanja celic na površino nosilcev smo ugotovili, da:

- lahko v nekaj sekundah po stiku nastanejo mnogo močnejše vezi od 200 pN;
- porazdelitev in moč pritrditve v merjenem sekundnem času korelirata z nadaljnjo rastjo celic, kar bi lahko uporabili za uporaben test biokompatibilnosti polimernih nosilcev;
- so procesi na začetnem stiku odvisni tudi od molekularne mobilnosti stranskih verig polimerov na površini – ta zato vpliva na pritrjevanje in posledično na rast celic.
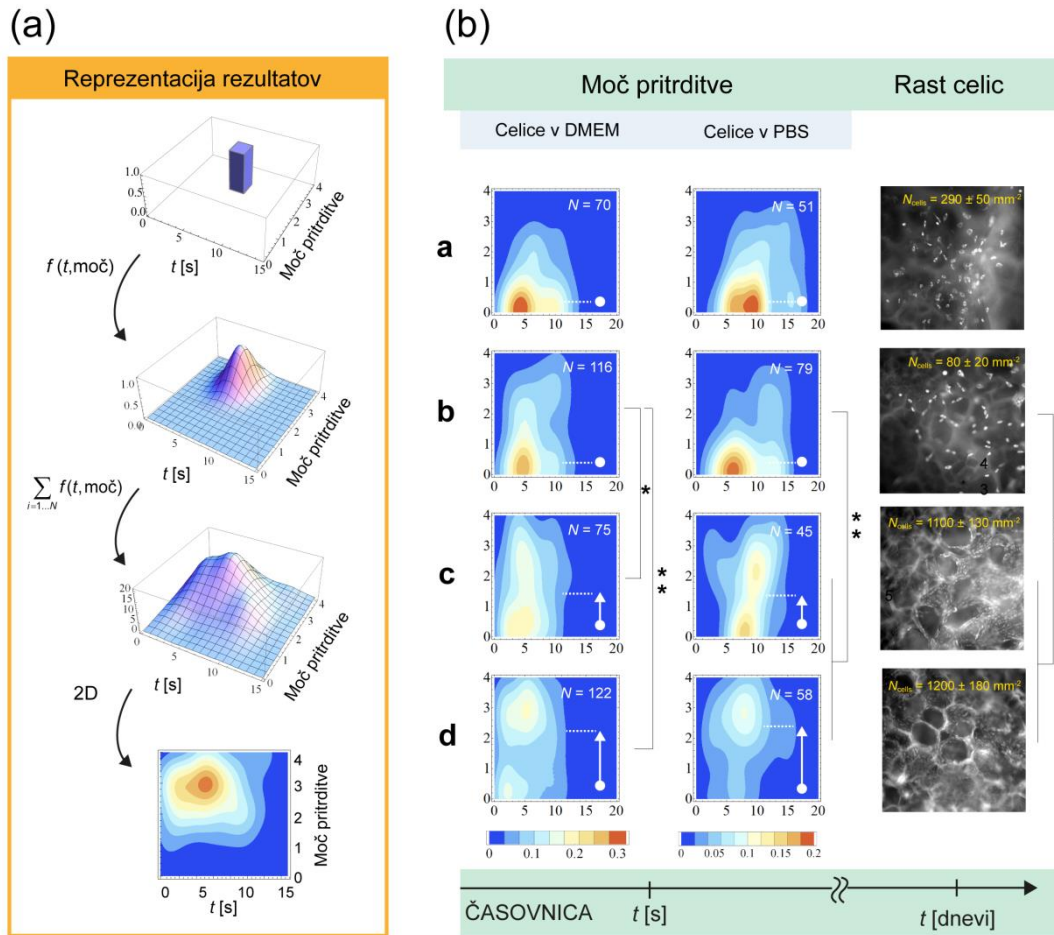
Slika 8. Shematski prikaz reprezentacije rezultatov (a), kjer f predstavlja 2D Gaussovo funkcijo in porazdelitev moči pritrditve v odvisnosti od časa stika na nosilcih z različno rastjo celic oz. biokompatibilnostjo (b). Pritrjevanje korelira z rastjo celic, kjer signifikantnost razlik predstavljamo s statističnim analizo, (*) $P = 0.01$ in (**) $P = 0.001$.

Appendix A   Measurement of microscope stage displacement

In order to characterize the forces on the cell-scaffold interface during the initial cell adhesion, the trapping potential of the cells trapped inside the optical tweezers field had to be measured. Important information was the cell escape force from an optical trap, where external force had to be applied. Hydrodynamic force was generated by moving the sample stage relative to the spatially fixed optical trap. To calculate hydrodynamic force by using Stokes equation, velocity of the fluid had to be measured. It was done by the measurement of microscope stage displacement i.e. its velocity profile (Figure A.1.).
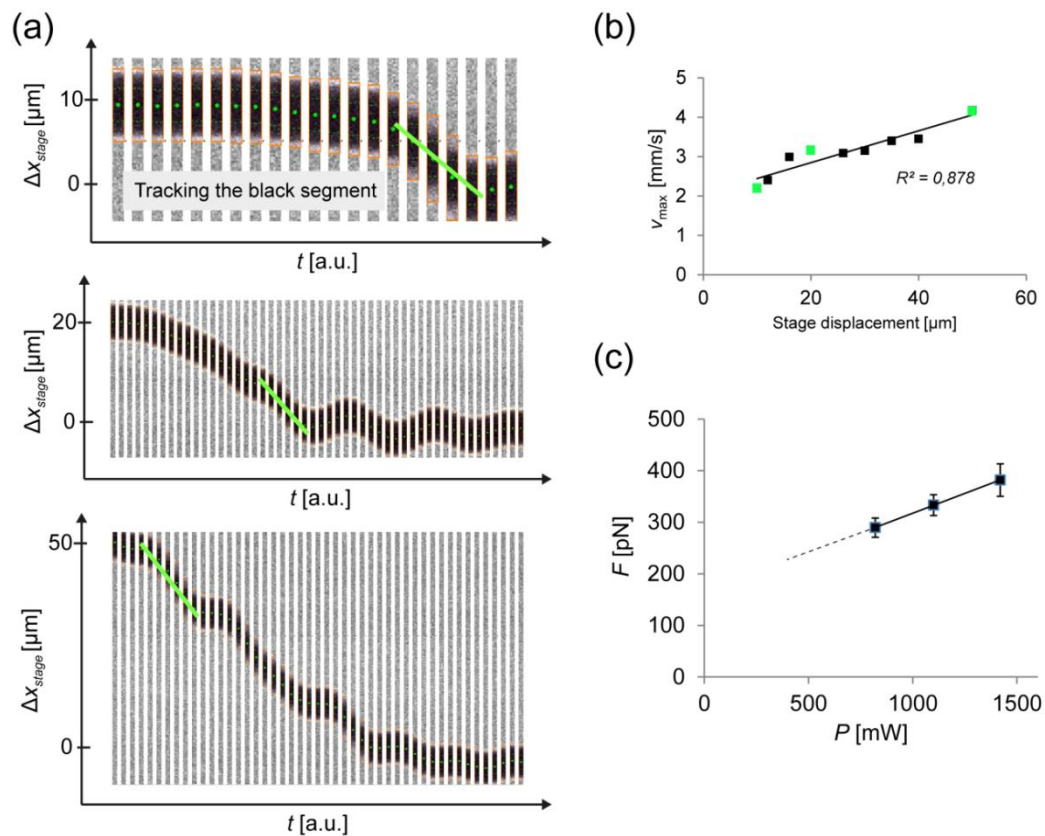
Figure A.1. Measurement of microscope stage displacement (a) and its velocity (b) needed for the characterization of the escape force of cell from an optical trap (c). Stage displacement was measured by tracking the stage-fixed highly contrasted spot. Maximum velocity, responsible for cell escape (green line) showed rough linear dependency with the amplitude of stage displacement. Escape force of cell from a trap was acquired using different optical tweezers powers. The error represents standard deviation of 5-8 measurements on different cells.

Appendix B Measurement of the calibration curve of cell viability assay
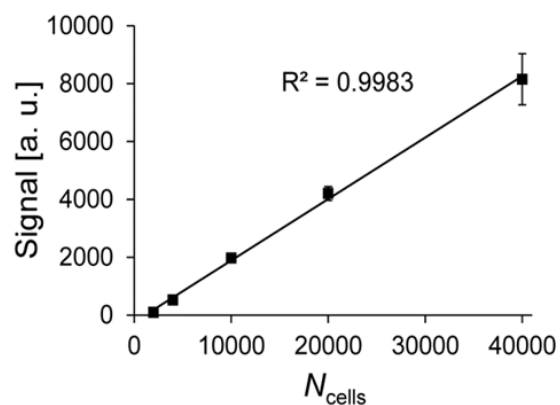
Figure B.1. Calibration curve of Resazurin viability assay for cell number characterization. It was done in triplicate with cells grown and counted in 96-well plates. Fluorescence was measured using excitation source of high power 300 W xenon Lambda LS arc-lamp (Sutter, Novato, CA, USA), CARV II spinning disk confocal module system (BD Biosciences, Franklin Lakes, NJ, USA) and Rolera MGi EMCCD camera detection (QImaging, Surrey, Canada).

References

1. Lysaght MJ. Product development in tissue engineering. *Tissue Eng.* 1995, **1**, 221–228.

2. Harrison RH, St-Pierre J-P, Stevens MM. Tissue engineering and regenerative medicine, a year in review. *Tissue Eng. Part B Rev.* 2014, **20**, 1–16.

3. Furth ME, Atala A, Van Dyke ME. Smart biomaterials design for tissue engineering and regenerative medicine. *Biomaterials* 2007, **28**, 5068–5073.

4. Owen SC, Shoichet MS. Design of three-dimensional biomimetic scaffolds. *J. Biomed. Mater. Res. A* 2010, **94**, 1321–1331.

5. Han J, Lazarovici P, Pomerantz C, Chen X, Wei Y, Lelkes PI. Co-electrospun blends of PLGA, gelatin, and elastin as potential nonthrombogenic scaffolds for vascular tissue engineering. *Biomacromolecules* 2011, **12**, 399–408.

6. Badylak SF, Freytes DO, Gilbert TW. Extracellular matrix as a biological scaffold material, Structure and function. *Acta Biomater.* 2009, 5, 1–13.

7. Yoon DM, Fisher JP. Natural and Synthetic Polymeric Scaffolds, In *Biomedical Materials*, Narayan R, ed. (Springer US, 2009), pp. 415–442.

8. Subia B, Kundu J, C. S. Biomaterial Scaffold Fabrication Techniques for Potential Tissue Engineering Applications. In *Tissue Engineering*, Eberli D, ed. (InTech, 2010)

9. Ma PX, Langer R, Fabrication of Biodegradable Polymer Foams for Cell Transplantation and Tissue Engineering, In *Tissue Engineering Methods and Protocols*, Morgan JR, Yarmush ML, eds. (Springer. Humana Press, 1999), pp. 47-56.

10. Nam YS, Park TG. Porous biodegradable polymeric scaffolds prepared by thermally induced phase separation. *J. Biomed. Mater. Res.* 1999, 47, 8–17.

11. Ren L, Tsuru K, Hayakawa S, Osaka A. Novel approach to fabricate porous gelatin–siloxane hybrids for bone tissue engineering. *Biomaterials* 2002, 23, 4765–4773.

12. Reneker DH, Chun I. Nanometre diameter fibres of polymer, produced by electrospinning. *Nanotechnology* 1996, 7, 216–223.

13. Yeong W-Y, Chua C-K, Leong K-F, Chandrasekaran M. Rapid prototyping in tissue engineering, challenges and potential. *Trends Biotechnol.* 2004, 22, 643–652.

14. Gauvin R, Chen Y-C, Lee JW, Soman P, Zorlutuna P, Nichol JW, et al. Microfabrication of complex porous tissue engineering scaffolds using 3D projection stereolithography. *Biomaterials* 2012, 33, 3824–3834.

15. Giannitelli SM, Accoto D, Trombetta M, Rainer A. Current trends in the design of scaffolds for computer-aided tissue engineering. *Acta Biomater.* 2014, 10, 580–594.

16. Sun J-Y, Zhao X, Illeperuma WRK, Chaudhuri O, Oh KH, Mooney DJ, et al. Highly stretchable and tough hydrogels. *Nature* 2012, 489, 133–136.

17. Bhat S, Tripathi A, Kumar A. Supermacroprous chitosan-agarose-gelatin cryogels, in vitro characterization and in vivo assessment for cartilage tissue engineering. *J. R. Soc. Interface* 2011, 8, 540–554.

18. Liu Q, Wang H. *Tissue Regeneration: Where Nano-Structure Meets Biology*, (WSPC, 2014).

19. Badylak SF, Taylor D, Uygun K. Whole-organ tissue engineering, decellularization and recellularization of three-dimensional matrix scaffolds. *Annu. Rev. Biomed. Eng.* 2011, 15, 27–53.

20. Williams DF. On the mechanisms of biocompatibility. *Biomaterials* 2008, 29, 2941–2953.

21. Radisic M, Euloth M, Yang L, Langer R, Freed LE, Vunjak-Novakovic G. High-density seeding of myocyte cells for cardiac tissue engineering. *Biotechnol. Bioeng.* 2003, 82, 403–414.

22. Atala A, Lanza R, Nerem RM, Thomson JA, (eds.) *Principles of Regenerative Medicine*, (Academic Press, 2011).

23. Griffith LG, Swartz MA. Capturing complex 3D tissue physiology in vitro. *Nat. Rev. Mol. Cell Biol.* 2006, 7, 211–224.

24. Sampson SL, Saraiva L, Gustafsson K, Jayasinghe SN, Robertson BD. Cell electrospinning, an in vitro and in vivo study. *Small Weinh. Bergstr. Ger.* 2014, 10, 78–82.

25. Sanz-Herrera JA, Reina-Romo E. Cell-Biomaterial Mechanical Interaction in the Framework of Tissue Engineering, Insights, Computational Modeling and Perspectives. *Int. J. Mol. Sci.* 2011, 12, 8217–8244.

26. Lee MH, Arcidiacono JA, Bilek AM, Wille JJ, Hamill CA, Wonnacott KM, et al. Considerations for tissue-engineered and regenerative medicine product development prior to clinical trials in the United States. *Tissue Eng. Part B Rev.* 2010, 16, 41–54.

27. O'Dea RD, Osborne JM, El Haj AJ, Byrne HM, Waters SL. The interplay between tissue growth and scaffold degradation in engineered tissue constructs. *J. Math. Biol.* 2013, 67, 1199–1225.

28. Kohane DS, Langer R. Biocompatibility and drug delivery systems. *Chem. Sci.* 2010, 1, 441–446.

29. Bhatia SK, (ed.) *Engineering Biomaterials for Regenerative Medicine, Novel Technologies for Clinical Applications*, (Springer, 2011).

30. Place ES, Evans ND, Stevens MM. Complexity in biomaterials for tissue engineering. *Nat. Mater.* 2009, 8, 457–470.

31. Kim TG, Shin H, Lim DW. Biomimetic Scaffolds for Tissue Engineering. *Adv. Funct. Mater.* 2012, 22, 2446–2468.

32. Laurencin CT, Nair LS, (eds.) *Nanotechnology and Tissue Engineering*, (CRC Press, 2008).

33. Romano NH, Sengupta D, Chung C, Heilshorn SC. Protein-engineered biomaterials, Nanoscale mimics of the extracellular matrix. *Biochim. Biophys. Acta. Bba.* 2011, 1810, 339–349.

34. Discher DE, Janmey P, Wang Y. Tissue Cells Feel and Respond to the Stiffness of Their Substrate. *Science* 2005, 310, 1139–1143.

35. Brandl F, Sommer F, Goepferich A. Rational design of hydrogels for tissue engineering, Impact of physical factors on cell behavior. *Biomaterials* 2007, 28, 134–146.

36. Schlie-Wolter S, Ngezahayo A, Chichkov BN. The selective role of ECM components on cell adhesion, morphology, proliferation and communication in vitro. *Exp. Cell Res.* 2013, 319, 1553–1561.

37. Oh SH, Kim TH, Im GI, Lee JH. Investigation of Pore Size Effect on Chondrogenic Differentiation of Adipose Stem Cells Using a Pore Size Gradient Scaffold. *Biomacromolecules* 2010, 11, 1948–1955.

38. Lien S-M, Ko L-Y, Huang T-J. Effect of pore size on ECM secretion and cell growth in gelatin scaffold for articular cartilage tissue engineering. *Acta Biomater.* 2009, 5, 670–679.

39. Oh SH, Park IK, Kim JM, Lee JH. In vitro and in vivo characteristics of PCL scaffolds with pore size gradient fabricated by a centrifugation method. *Biomaterials* 2007, 28, 1664–1671.

40. Harley BAC, Kim H-D, Zaman MH, Yannas IV, Lauffenburger DA, Gibson LJ. Microarchitecture of three-dimensional scaffolds influences cell migration behavior via junction interactions. *Biophys. J.* 2008, 95, 4013–4024.

41. Murphy CM, Haugh MG, O'Brien FJ. The effect of mean pore size on cell attachment, proliferation and migration in collagen-glycosaminoglycan scaffolds for bone tissue engineering. *Biomaterials* 2010, 31, 461–466.

42. Lee M, Wu BM, Dunn JCY. Effect of scaffold architecture and pore size on smooth muscle cell growth. *J. Biomed. Mater. Res. A.* 2008, 87, 1010–1016.

43. S Van Bael YCC. The effect of pore geometry on the in vitro biological behavior of human periosteum-derived cells seeded on selective laser-melted Ti6Al4V bone scaffolds. *Acta. Biomater.* 2012, 8, 2824–2834.

44. Sobral JM, Caridade SG, Sousa RA, Mano JF, Reis RL. Three-dimensional plotted scaffolds with controlled pore size gradients, Effect of scaffold geometry on mechanical performance and cell seeding efficiency. *Acta. Biomater.* 2011, 7, 1009–1018.

45. Griffon DJ, Sedighi MR, Schaeffer DV, Eurell JA, Johnson AL. Chitosan scaffolds, Interconnective pore size and cartilage engineering. *Acta. Biomater.* 2006, 2, 313–320.

46. Hadjipanayi E, Mudera V, Brown RA. Close dependence of fibroblast proliferation on collagen scaffold matrix stiffness. *J. Tissue Eng. Regen. Med.* 2009, 3, 77–84.

47. Haugh MG, Murphy CM, McKiernan RC, Altenbuchner C, O'Brien FJ. Crosslinking and mechanical properties significantly influence cell attachment, proliferation, and migration within collagen glycosaminoglycan scaffolds. *Tissue Eng. Part A.* 2011, 17, 1201–1208.

48. Ghosh K, Pan Z, Guan E, Ge S, Liu Y, Nakamura T, et al. Cell adaptation to a physiologically relevant ECM mimic with different viscoelastic properties. *Biomaterials* 2007, 28, 671–679.

49. Chen J, Irianto J, Inamdar S, Pravincumar P, Lee DA, Bader DL, et al. Cell mechanics, structure, and function are regulated by the stiffness of the three-dimensional microenvironment. *Biophys. J.* 2012, 103, 1188–1197.

50. Saha K, Keung AJ, Irwin EF, Li Y, Little L, Schaffer DV, et al. Substrate modulus directs neural stem cell behavior. *Biophys. J.* 2008, 95, 4426–4438.

51. Reinhart-King CA, Dembo M, Hammer DA. Cell-Cell Mechanical Communication through Compliant Substrates. *Biophys. J.* 2008, 95, 6044–6051.

52. Dikovsky D, Bianco-Peled H, Seliktar D. Defining the Role of Matrix Compliance and Proteolysis in Three-Dimensional Cell Spreading and Remodeling. *Biophys. J.* 2008, 94, 2914–2925.

53. Liu C, Abedian R, Meister R, Haasper C, Hurschler C, Krettek C, et al. Influence of perfusion and compression on the proliferation and differentiation of bone mesenchymal stromal cells seeded on polyurethane scaffolds. *Biomaterials* 2012, 33, 1052–1064.

54. Keselowsky BG, Collard DM, García AJ. Integrin binding specificity regulates biomaterial surface chemistry effects on cell differentiation. *Proc. Natl. Acad. Sci. U.S.A.* 2005, 102, 5953–5957.

55. Koo LY, Irvine DJ, Mayes AM, Lauffenburger DA, Griffith LG. Co-regulation of cell adhesion by nanoscale RGD organization and mechanical stimulus. *J. Cell Sci.* 2002, 115, 1423–1433.

56. Brown BN, Barnes CA, Kasick RT, Michel R, Gilbert TW, Beer-Stolz D, et al. Surface Characterization of Extracellular Matrix Scaffolds. *Biomaterials* 2010, 31, 428–437.

57. Kisiday J, Jin M, Kurz B, Hung H, Semino C, Zhang S, et al. Self-assembling peptide hydrogel fosters chondrocyte extracellular matrix production and cell division, Implications for cartilage tissue repair. *Proc. Natl. Acad. Sci. U. S. A.* 2002, 99, 9996–10001.

58. Ivirico JLE, Salmerón-Sánchez M, Ribelles JLG, Pradas MM, Soria JM, Gomes ME, et al. Proliferation and differentiation of goat bone marrow stromal cells in 3D scaffolds with tunable hydrophilicity. *J. Biomed. Mater. Res. B Appl. Biomater.* 2009, 91, 277–286.

59. Koh HS, Yong T, Chan CK, Ramakrishna S. Enhancement of neurite outgrowth using nano-structured scaffolds coupled with laminin. *Biomaterials* 2008, 29, 3574–3582.

60. Washburn NR, Yamada KM, Simon CG, Kennedy SB, Amis EJ. High-throughput investigation of osteoblast response to polymer crystallinity, influence of nanometer-scale roughness on proliferation. *Biomaterials* 2004, 25, 1215–1224.

61. Santos E, Hernández RM, Pedraz JL, Orive G. Novel advances in the design of three-dimensional bio-scaffolds to control cell fate, translation from 2D to 3D. *Trends Biotechnol.* 2012, 30, 331–341.

62. Van der Flier A, Sonnenberg A. Function and interactions of integrins. *Cell Tissue Res.* 2001, 305, 285–298.

63. Hynes RO. Integrins, Bidirectional, Allosteric Signaling Machines. *Cell* 2002, 110, 673–687.

64. Luo B-H, Carman CV, Springer TA. Structural basis of integrin regulation and signaling. *Annu. Rev. Immunol.* 2007, 25, 619–647.

65. Geiger B, Spatz JP, Bershadsky AD. Environmental sensing through focal adhesions. *Nat. Rev. Mol. Cell Biol.* 2009, 10, 21–33.

66. Schaller MD, Borgman CA, Cobb BS, Vines RR, Reynolds AB, Parsons JT. pp125FAK a structurally distinctive protein-tyrosine kinase associated with focal adhesions. *Proc. Natl. Acad. Sci. U. S. A.* 1992, 89, 5192–5196.

67. Wang HB, Dembo M, Hanks SK, Wang Y. Focal adhesion kinase is involved in mechanosensing during fibroblast migration. *Proc. Natl. Acad. Sci. U. S. A.* 2001, 98, 11295–11300.

68. Mofrad MR, Kamm RD, (eds.) *Cellular Mechanotransduction: Diverse Perspectives from Molecules to Tissues*, (Cambridge University Press, 2010).

69. Schwarz US, Safran SS. Physics of adherent cells. *Rev. Mod. Phys.* 2013, 85, 1327–1381.

70. Bausch AR, Schwarz US. Cellular mechanosensing, Sharing the force. *Nat. Mater.* 2013, 12, 948–949.

71. Hoffman BD, Grashoff C, Schwartz MA. Dynamic molecular processes mediate cellular mechanotransduction. *Nature.* 2011, 475, 316–323.

72. Jin G-Z, Kim H-W. Nanocomposite bioactive polymeric scaffold promotes adhesion, proliferation and osteogenesis of rat bone marrow stromal cells. *Tissue Eng. Regen. Med.* 2014, 11, 284–290.

73. Huang W-C, Liu K-H, Liu T-C, Liu D-M, Chen S-Y. Synergistic hierarchical silicone-modified polysaccharide hybrid as a soft scaffold to control cell adhesion and proliferation. *Acta Biomater.* 2014, 10, 3546–3556.

74. Collart-Dutilleul P-Y, Secret E, Panayotov I, Deville de Périère D, Martín-Palma RJ, Torres-Costa V, et al. Adhesion and Proliferation of Human Mesenchymal Stem Cells from Dental Pulp on Porous Silicon Scaffolds. *ACS Appl. Mater. Interfaces* 2014, 6, 1719–1728.

75. García AJ, Ducheyne P, Boettiger D. Quantification of cell adhesion using a spinning disc device and application to surface-reactive materials. *Biomaterials* 1997, 18, 1091–1098.

76. Lemmon CA, Sniadecki NJ, Ruiz SA, Tan JL, Romer LH, Chen CS. Shear Force at the Cell-Matrix Interface, Enhanced Analysis for Microfabricated Post Array Detectors. *Mech. Chem. Biosyst. Mcb.* 2005, 2, 1–16.

77. Nugiel DJ, Wood DJ, Sung KL. Quantification of adhesiveness of osteoblasts to titanium surfaces in vitro by the micropipette aspiration technique. *Tissue Eng.* 1996, 2, 127–140.

78. Reyes CD, García AJ. A centrifugation cell adhesion assay for high-throughput screening of biomaterial surfaces. *J. Biomed. Mater. Res. A.* 2003, 67, 328–333.

79. Helenius J, Heisenberg C-P, Gaub HE, Muller DJ. Single-cell force spectroscopy. *J. Cell Sci.* 2008, 121, 1785–1791.

80. Zhang H, Liu K-K. Optical tweezers for single cells. *J. R. Soc. Interface* 2008, 5, 671–690.

81. Taubenberger A, Cisneros DA, Friedrichs J, Puech P-H, Muller DJ, Franz CM. Revealing early steps of alpha2beta1 integrin-mediated adhesion to collagen type I by using single-cell force spectroscopy. *Mol. Biol. Cell* 2007, 18,1634–1644.

82. Thoumine O, Kocian P, Kottelat A, Meister JJ. Short-term binding of fibroblasts to fibronectin, optical tweezers experiments and probabilistic analysis. *Eur Biophys J* 2000, 29, 398–408.

83. Wang X, Ha T. Defining Single Molecular Forces Required to Activate Integrin and Notch Signaling. *Science* 2013, 340, 991–994.

84. Zhang Y, Ge C, Zhu C, Salaita K. DNA-based digital tension probes reveal integrin forces during early cell adhesion. *Nat. Commun.* 2014, 5:5167.

85. Capitanio M, Pavone FS. Interrogating Biology with Force, Single Molecule High-Resolution Measurements with Optical Tweezers. *Biophys. J.* 2013, 105, 1293–1303.

86. Difato F, Pinato G, Cojoc D. Cell Signaling Experiments Driven by Optical Manipulation. *Int. J. Mol. Sci.* 2013,14, 8963–8984.

87. Bustamante C, Macosko JC, Wuite GJL. Grabbing the cat by the tail, manipulating molecules one by one. *Nat. Rev. Mol. Cell Biol.* 2000, 1, 130–136.

88. Bowman RW, Padgett MJ. Optical trapping and binding. *Reports Prog. Phys.* 2013, 76, 026401.

89. Ashkin A. Optical trapping and manipulation of neutral particles using lasers. *Proc. Natl. Acad. Sci. U. S. A.* 1997, 94, 4853–4860.

90. Richardson AC, Reihani N, Oddershede LB. In *Combining confocal microscopy with precise force-scope optical tweezers*, Dholakia K, Spalding GC, eds. (SPIE. San Diego, 2006), pp. 632628–632637.

91. Comstock MJ, Ha T, Chemla YR. Ultrahigh-resolution optical trap with single-fluorophore sensitivity. *Nat. Methods* 2011, 8, 335–340.

92. Thoumine O, Bard L, Saint-Michel E, Dequidt C, Choquet D. Optical Tweezers and Fluorescence Recovery After Photo-Bleaching to Measure Molecular Interactions at the Cell Surface. *Cell. Mol. Bioeng.* 2008, 1, 301–311.

93. Andersson M, Madgavkar A, Stjerndahl M, Wu Y, Tan W, Duran R, et al. Using optical tweezers for measuring the interaction forces between human bone cells and implant surfaces, System design and force calibration. *Rev. Sci. Instrum.* 2007, 78, 074302.

94. Gou X, Han HC, Hu S, Leung AYH, Sun D. Applying combined optical tweezers and fluorescence microscopy technologies to manipulate cell adhesions for cell-to-cell interaction study. *IEEE Trans. Biomed. Eng.* 2013, 60, 2308–2315.

95. Zaman MH, Trapani LM, Sieminski AL, MacKellar D, Gong H, Kamm RD, et al. Migration of tumor cells in 3D matrices is governed by matrix stiffness along with cell-matrix adhesion and proteolysis. *Proc. Natl. Acad. Sci. U. S. A.* 2006, 103, 10889–10894.

96. Elosegui-Artola A, Bazellières E, Allen MD, Andreu I, Oria R, Sunyer R, et al. Rigidity sensing and adaptation through regulation of integrin types. *Nat. Mater.* 2014, 13, 631–637.

97. Pathak A, Kumar S. Independent regulation of tumor cell migration by matrix stiffness and confinement. *Proc. Natl. Acad. Sci. U. S. A.* 2012, 109, 10334–10339.

98. Hemminga MA, Berliner L, (eds.) *ESR Spectroscopy in Membrane Biophysics*, (Springer, US, 2007).

99. Stopar D, Štrancar J, Spruijt RB, Hemminga MA. Motional Restrictions of Membrane Proteins, A Site-Directed Spin Labeling Study. *Biophys. J.* 2006, 91, 3341–3348.

100. Podlipec R, Koklic T, Strancar J, Mravljak J, Sentjurc M. Influence of cancerostatic perifosine on membrane fluidity of liposomes and different cell lines as measured by electron paramagnetic resonance. *Croat. Med. J.* 2012, 53, 558–567.

101. Arsov Z, Urbančič I, Garvas M, Biglino D, Ljubetič A, Koklič T, et al. Fluorescence microspectroscopy as a tool to study mechanism of nanoparticles delivery into living cancer cells. *Biomed. Opt. Express* 2011, 2, 2083–2095.

102. Demchenko AP, Mély Y, Duportail G, Klymchenko AS. Monitoring Biophysical Properties of Lipid Membranes by Environment-Sensitive Fluorescent Probes. *Biophys. J.* 2009, 96, 3461–3470.

103. Gornall JL, Terentjev EM. Universal kinetics of helix-coil transition in gelatin. *Phys. Rev. E Stat. Nonlin. Soft Matter. Phys.* 2008, 77, 031908.

104. Mckinney RM, Spillane JT, Pearce GW. Factors Affecting the Rate of Reaction of Fluorescein Isothiocyanate with Serum Proteins. *J. Immunol.* 1964, 93, 232–242.

105. Griffith OH, McConnell HM. A NITROXIDE-MALEIMIDE SPIN LABEL*. *Proc. Natl. Acad. Sci. U. S. A.* 1966, 55, 8–11.

106. Plieva FM, Kumar A, Galaev IY, Mattiasson B. Design of Supermacroporous Biomaterials via Gelation at Subzero Temperatures—Cryogelation. In *Advanced Biomaterials*, Basu B, Katti DS, Kumar A, eds. (John Wiley & Sons, Inc., 2010), pp. 499–531.

107. Boffito M, Bernardi E, Sartori S, Ciardelli G, Sassi MP. A mechanical characterization of polymer scaffolds and films at the macroscale and nanoscale. *J. Biomed. Mater. Res. A.* 2015, 103, 162–169.

108. Sartori S, Boffito M, Serafini P, Caporale A, Silvestri A, Bernardi E, et al. Synthesis and structure–property relationship of polyester-urethanes and their evaluation for the regeneration of contractile tissues. *React. Funct. Polym.* 2013, 73, 1366–1376.

109. Klare JP, Steinhoff H-J. Spin labeling EPR. *Photosynth. Res.* 2009,102, 377–390.

110. Nesmelov YE, Thomas DD. Protein structural dynamics revealed by site-directed spin labeling and multifrequency EPR. *Biophys. Rev.* 2010, 2, 91–99.

111. Štrancar J. Advanced ESR Spectroscopy in Membrane Biophysics. In *ESR Spectroscopy in Membrane Biophysics*, (Springer US, 2007), pp. 49–93.

112. Štrancar J, Kavalenka A, Urbančič I, Ljubetič A, Hemminga MA. SDSL-ESR-based protein structure characterization. *Eur. Biophys. J.* 2010, 39, 499–511.

113. Kavalenka A, Urbančič I, Belle V, Rouger S, Costanzo S, Kure S, et al. Conformational Analysis of the Partially Disordered Measles Virus NTAIL-XD Complex by SDSL EPR Spectroscopy. *Biophys. J.* 2010, 98,1055–1064.

114. Ghosh K, Shu XZ, Mou R, Lombardi J, Prestwich GD, Rafailovich MH, et al. Rheological Characterization of in Situ Cross-Linkable Hyaluronan Hydrogels. *Biomacromolecules* 2005, 6, 2857–2865.

115. Aulova A, Emri I. Solving Inverse Problems in Viscoelasticity by Using Neural Network. SEMDOK conference, 2013.

116. Christensen R. (ed.) *Theory of Viscoelasticity, An Introduction*. (Elsevier, 2012).

117. Zhu Y, Dong Z, Wejinya UC, Jin S, Ye K. Determination of mechanical properties of soft tissue scaffolds by atomic force microscopy nanoindentation. *J. Biomech.* 2011, 44, 2356–2361.

118. Bilodeau GG. Regular Pyramid Punch Problem. *J. Appl. Mech.* 1992, 59, 519–523.

119. Macosko CW, (ed.) *Rheology, Principles, Measurements, and Applications*, (Wiley-VCH, 1994).

120. Ashkin A. (ed.) *Optical Trapping and Manipulation of Neutral Particles Using Lasers*, (World Scientific, 2006).

121. Grier DG. A revolution in optical manipulation. *Nature* 2003, 424, 810–816.

122. Mehta AD, Rief M, Spudich JA, Smith DA, Simmons RM. Single-Molecule Biomechanics with Optical Methods. *Science* 1999, 283, 1689–1695.

123. López-Quesada C, Fontaine A-S, Farré A, Joseph M, Selva J, Egea G, et al. Artificially-induced organelles are optimal targets for optical trapping experiments in living cells. *Biomed. Opt. Express.* 2014, 5, 1993–2008.

124. Tlusty T, Meller A, Bar-Ziv R. Optical Gradient Forces of Strongly Localized Fields. *Phys. Rev. Lett.* 1998, 81, 1738–1741.

125. Nieminen TA, Loke VLY, Stilgoe AB, Knöner G, Brańczyk AM, Heckenberg NR, et al. Optical tweezers computational toolbox. *J. Opt. Pure Appl. Opt.* 2007, 9, S196.

126. Neuman KC, Block SM. Optical trapping. *Rev. Sci. Instrum.* 2004, 75, 2787–2809.

127. Visscher K, Gross SP, Block SM. Construction of multiple-beam optical traps with nanometer-resolution position sensing. *IEEE J. Sel. Topics Quantum Electron.*, 1996, 2, 1066–1076.

128. Simmons RM, Finer JT, Chu S, Spudich JA. Quantitative measurements of force and displacement using an optical trap. *Biophys. J.* 1996, 70, 1813–1822.

129. Mellor CD, Sharp MA, Bain CD, Ward AD. Probing interactions between colloidal particles with oscillating optical tweezers. *J. Appl. Phys.* 2005, 97, 103114.

130. Chan JW. Recent advances in laser tweezers Raman spectroscopy (LTRS) for label-free analysis of single cells. *J. Biophotonics.* 2013, 6, 36–48.

131. Liu Y, Cheng DK, Sonek GJ, Berns MW, Chapman CF, Tromberg BJ. Evidence for localized cell heating induced by infrared optical tweezers. *Biophys. J.* 1995, 68, 2137–2144.

132. Ayano S, Wakamoto Y, Yamashita S, Yasuda K. Quantitative measurement of damage caused by 1064-nm wavelength optical trapping of Escherichia coli cells using on-chip single cell cultivation system. *Biochem. Biophys. Res. Commun.* 2006, 350, 678–684.

133. Urbancic I. Response of biomembrane domains to external stimuli. PhD Dissertation (University in Maribor, Slovenia, 2014).

134. Litvinov RI, Shuman H, Bennett JS, Weisel JW. Binding strength and activation state of single fibrinogen-integrin pairs on living cells. *Proc. Natl. Acad. Sci. U. S. A.* 2002, 99, 7426–7431.

135. Castelain M, Rouxhet PG, Pignon F, Magnin A, Piau J-M. Single-cell adhesion probed in-situ using optical tweezers, A case study with Saccharomyces cerevisiae. *J. Appl. Phys.* 2012, 111, 114701.

136. Evans EA, Calderwood DA. Forces and bond dynamics in cell adhesion. *Science* 2007, 316, 1148–1153.

137. Bell GI. Models for the specific adhesion of cells to cells. *Science* 1978, 200, 618–627.

138. Schwingel M, Bastmeyer M. Force Mapping during the Formation and Maturation of Cell Adhesion Sites with Multiple Optical Tweezers. *Plos One.* 2013, 8, e54850.

139. König K. Laser tweezers are sources of two-photon excitation. *Cell. Mol. Biol.* 1998, 44, 721–733.

140. H. T. Banks, S. Hu and Z. R. Kenz. A Brief Review of Elasticity and Viscoelasticity for Solids. *Adv. Appl. Math. Mech.* 2010, 1.

141. Page B, Page M, Noel C. A new fluorometric assay for cytotoxicity measurements in-vitro. *Int. J. Oncol.* 1993, 3, 473–476.

142. Lo CM, Wang HB, Dembo M, Wang YL. Cell movement is guided by the rigidity of the substrate. *Biophys. J.* 2000, 79, 144–152.

143. Baaijens FPT, Trickey WR, Laursen TA, Guilak F. Large deformation finite element analysis of micropipette aspiration to determine the mechanical properties of the chondrocyte. *Ann. Biomed. Eng.* 2005, 33, 494–501.

144. Guilak F, Tedrow JR, Burgkart R. Viscoelastic properties of the cell nucleus. *Biochem. Biophys. Res. Commun.* 2000, 269, 781–786.

145. Hochmuth RM. Micropipette aspiration of living cells. *J. Biomech.* 2000, 33, 15–22.

146. Darling EM, Zauscher S, Block JA, Guilak F. A Thin-Layer Model for Viscoelastic, Stress-Relaxation Testing of Cells Using Atomic Force Microscopy, Do Cell Properties Reflect Metastatic Potential? *Biophys. J.* 2007, 92, 1784–1791.

147. Cross SE, Jin Y-S, Rao J, Gimzewski JK. Nanomechanical analysis of cells from cancer patients. *Nat. Nanotechnol.* 2007, 2, 780–783.

148. Plodinec M, Loparic M, Monnier CA, Obermann EC, Zanetti-Dallenbach R, Oertle P, et al. The nanomechanical signature of breast cancer. *Nat. Nanotechnol.* 2012, 7, 757–765.

149. Mahaffy RE, Park S, Gerde E, Käs J, Shih CK. Quantitative Analysis of the Viscoelastic Properties of Thin Regions of Fibroblasts Using Atomic Force Microscopy. *Biophys. J.* 2004, 86, 1777–1793.

150. Shieh AC, Athanasiou KA. Biomechanics of single zonal chondrocytes. *J. Biomech.* 2006, 39, 1595–1602.

151. Ofek G, Natoli RM, Athanasiou KA. In situ mechanical properties of the chondrocyte cytoplasm and nucleus. *J. Biomech.* 2009, 42, 873–877.

152. Nguyen BV, Wang QG, Kuiper NJ, El Haj AJ, Thomas CR, Zhang Z. Biomechanical properties of single chondrocytes and chondrons determined by micromanipulation and finite-element modelling. *J. R. Soc. Interface* 2010, 7, 1723–1733.

153. Matthews BD, Overby DR, Mannix R, Ingber DE. Cellular adaptation to mechanical stress, role of integrins, Rho, cytoskeletal tension and mechanosensitive ion channels. *J. Cell. Sci.* 2006, 119, 508–518.

154. Gorelik J, Shevchuk AI, Frolenkov GI, Diakonov IA, Lab MJ, Kros CJ, et al. Dynamic assembly of surface structures in living cells. *Proc. Natl. Acad. Sci. U. S. A.* 2003, 100, 5819–5822.

155. Guck J, Ananthakrishnan R, Mahmood H, Moon TJ, Cunningham CC, Kas J. The optical stretcher, a novel laser tool to micromanipulate cells. *Biophys. J.* 2001, 81, 767–784.

156. Alon R, Hammer DA, Springer TA. Lifetime of the P-selectin-carbohydrate bond and its response to tensile force in hydrodynamic flow. *Nature.* 1995, 374, 539–542.

157. Dong C, Cao J, Struble EJ, Lipowsky HH. Mechanics of Leukocyte Deformation and Adhesion to Endothelium in Shear Flow. *Ann. Biomed. Eng.* 1999, 27, 298–312.

158. Spillmann CM, Lomakina E, Waugh RE. Neutrophil Adhesive Contact Dependence on Impingement Force. *Biophys. J.* 2004, 87, 4237–4245.

159. Schmitz J, Benoit M, Gottschalk K-E. The viscoelasticity of membrane tethers and its importance for cell adhesion. *Biophys. J.* 2008, 95, 1448–1459.

160. Schakenraad JM, Busscher HJ, Wildevuur CRH, Arends J. The influence of substratum surface free energy on growth and spreading of human fibroblasts in the presence and absence of serum proteins. *J. Biomed. Mater. Res.* 1986, 20, 773–784.

161. Dubruel P, Unger R, Van Vlierberghe S, Cnudde V, Jacobs PJS, Schacht E, et al. Porous Gelatin Hydrogels, 2. In Vitro Cell Interaction Study. *Biomacromolecules* 2007, 8, 338–344.

162. Dong C, Lei XX. Biomechanics of cell rolling, shear flow, cell-surface adhesion, and cell deformability. *J. Biomech.* 2000, 33, 35–43.

163. Murphy-Ullrich JE. The de-adhesive activity of matricellular proteins, is intermediate cell adhesion an adaptive state? *J. Clin. Invest.* 2001, 107, 785–790.

164. Curtis AS, Chandler C, Picton N. Cell surface lipids and adhesion. III. The effects on cell adhesion of changes in plasmalemmal lipids. *J. Cell Sci.* 1975, 18, 375–384.

165. Molitoris BA, Wagner MC. Surface membrane polarity of proximal tubular cells, Alterations as a basis for malfunction. *Kidney Int.* 1996, 49, 1592–1597.

166. Urbančič I, Arsov Z, Ljubetič A, Biglino D, Strancar J. Bleaching-corrected fluorescence microspectroscopy with nanometer peak position resolution. *Opt. Express.* 2013, 21, 25291–25306.

167. Arsov Z, Quaroni L. Direct interaction between cholesterol and phosphatidylcholines in hydrated membranes revealed by ATR-FTIR spectroscopy. *Chem. Phys. Lipids* 2007, 150, 35–48.

Professional curriculum vitae

PERSONAL INFORMATIONS

Date and place of birth: July 2, 1986, Jesenice, Slovenia

EDUCATION

2011 – 2015:	Ph. D. studies, Biophysics, Faculty of Natural Sciences and Mathematics, University of Maribor, Slovenia; PhD thesis: *The analysis of cell-biomaterial interaction by advanced experimental techniques as the basis for biocompatibility studies of polymers*
2005 – 2011:	B. Sc., Physics, Faculty of Mathematics and Physics, University of Ljubljana, Slovenia; Diploma thesis: *Studying the transport of alkylphospholipids through the membrane of malign breast cancer cells by electron paramagnetic resonance.*

ADDITIONAL EDUCATION

July 2015:	EBSA Congress Workshop 2015, *Spectroscopies in Biology*
January 2014:	XVIII School of Pure and Applied Biophysics, Venice, Italy: *Nanomechanics of biomolecular adhesion*
July 2008:	European Summer University, Strasbourg, France: *Physics Probes - Interface with Chemistry, Biology and Medicine*

EMPLOYEMENT

2015 – present:	Research associate in Laboratory of Biophysics, Institute "Jožef" Stefan, Ljubljana, Slovenia
2011 – 2014:	Research associate at Centre of Excellence NAMASTE, Ljubljana, Slovenia

RESEARCH EXPERIENCE

2015 – present: Development of the optical setup and detection of eye retina.

2012 – 2015:   Development of the optical tweezers technique for cell adhesion dynamics characterization on scaffolds surfaces suitable for biocompatibility testing studies.

2011 – 2014:   Mechanical, morphological and molecular characterization of 3D porous polymer scaffolds for tissue engineering.

2011 – 2014:   Fabrication of natural and synthetic 3D porous scaffolds using cryogelation and temperature induced phase separation (collaboration with Institute for Engineering Materials and Design, University of Maribor and Biomedical Lab, DIMEAS, Politecnico di Torino, Italy).

2011 – 2013:   Characterization of polymer molecular dynamics in tissue engineering scaffolds by electron paramagnetic resonance spectroscopy.

2008 – 2011:   Characterization of fatty acid membrane anticancer drug interaction with breast cancer cells

2008 – 2010:   Characterization of liposome-encapsulated drug delivery across a cell barrier

RESEARCH EXPERTISE

Optical tweezers, electron paramagnetic resonance (EPR) spectroscopy, UV-Vis spectroscopy, FTIR spectroscopy, atomic force spectroscopy (AFM), confocal fluorescence microscopy, fluorescence microspectroscopy, dynamic mechanical analysis (DMA), differential scanning calorimetry (DSC), gel permeation and size exclusion chromatography (GPC/SEC), working with cell tissues, preparation of liposomal formulations, scaffold surface modification with plasma grafting and protein treatment

TEACHING

2014:   Lecture at the Politecnico di Torino for students of Biomedical Engineering, *Introduction to Scanning Probe Microscopies and their applications in biomedical science*

SCIENTIFIC SOCIETIES

2011–present: Member of Slovenian Biophysical Society

Personal COBISS bibliography

1.01 Original scientific article

1. PODLIPEC, Rok, ŠTRANCAR, Janez. Cell-scaffold adhesion dynamics measured in first seconds predicts cell growth on days scale - optical tweezers study. *ACS applied materials & interfaces*, 2015, vol. 7, no. 12, str. 6782-6791, doi, 10.1021/acsami.5b00235. [COBISS.SI-ID 28541479]

2. TESTEN, Anže, PODLIPEC, Rok, MRAVLJAK, Janez, ORTHMANN, Andrea, ŠENTJURC, Marjeta, ZEISIG, Reiner, ŠTRANCAR, Janez, KOKLIČ, Tilen. How perifosine affects liposome-encapsulated drug delivery across a cell barrier. *Therapeutic delivery*, 2015, vol. 6, no. 4, str. 423-441, doi, 10.4155/tde.14.127. [COBISS.SI-ID 3863665]

3. PODLIPEC, Rok, GORGIEVA, Selestina, JURAŠIN, Darija, URBANČIČ, Iztok, KOKOL, Vanja, ŠTRANCAR, Janez. Molecular mobility of scaffolds' biopolymers influences cell growth. *ACS applied materials & interfaces*, 2014, vol. 6, iss. 18, str. 15980-15990, doi, 10.1021/am5037719. [COBISS.SI-ID 18043926]

4. PODLIPEC, Rok, KOKLIČ, Tilen, ŠTRANCAR, Janez, MRAVLJAK, Janez, ŠENTJURC, Marjeta. Influence of cancerostatic perifosine on membrane fluidity of liposomes and different cell lines as measured by electron paramagnetic resonance. *Croatian Medical Journal,* 2012, vol. 53, no. 6, str. 558-567, doi, 10.3325/cmj.2012.53.558. [COBISS.SI-ID 3377265]

1.08 Published scientific conference contribution

5. PODLIPEC, Rok, KOKLIČ, Tilen, ŠTRANCAR, Janez, ŠENTJURC, Marjeta. Interaction of cancerostatic perifosine with different cell lines. V, ZAKRZEWSKA, Joanna (ur.), ŽIVIĆ, Miroslav (ur.). *Proceedings, RBC 2012, Regional Biophysics Conference 2012, Kladovo-Beograd, Serbia,* str. 36-38. [COBISS.SI-ID 26065959]

6. KOKLIČ, Tilen, PODLIPEC, Rok, ORTHMANN, Andrea, ŠENTJURC, Marjeta, ŠTRANCAR, Janez, ZEISIG, Reiner. Perifosine containing, transcytosis efficient liposomes have higher content leakage and relative proportion of micelles. V, ZAKRZEWSKA, Joanna (ur.), ŽIVIĆ, Miroslav (ur.). *Proceedings, RBC 2012, Regional Biophysics Conference 2012, Kladovo-Beograd, Serbia,* str. 48-50. [COBISS.SI-ID 26066215]

7. GANTAR, Ana, DRNOVŠEK, Nataša, PODLIPEC, Rok, ŠTRANCAR, Janez, NOVAK, Saša. Bioactive-glass/collagen composite scaffollds for bone regeneration. V, 2nd Joint Meeting of the COST action MP1005 NAMABIO, 2012, Vienna, Austria. *Programme & book of abstracts*. 2012, str. 23. [COBISS.SI-ID 26115111]

1.10 Published scientific conference contribution abstract (invited lecture)

8. PODLIPEC, Rok, JURAŠIN, Darija, GORGIEVA, Selestina, KOKOL, Vanja, ŠTRANCAR, Janez. Can we tune biopolymer-scaffold's properties by correlating macro and molecular studies. V, *E-MRS 2012 fall meeting, Warsaw University of Technology*. [COBISS.SI-ID 16271638]

1.12 Published scientific conference contribution abstract

9. PODLIPEC, Rok, ŠTRANCAR, Janez. Scaffold biocompatibility with respect to biopolymer mobility and cell adhesion dynamics : [presented at 105th EBSA European Biophysics Congress, 18-22 July 2015, Dresden, Germany]. European biophysics journal, ISSN 0175-7571, 2015, vol. 44, suppl. 1, str. S134. [COBISS.SI-ID 28760615], [JCR, SNIP]

10. PODLIPEC, Rok, ŠTRANCAR, Janez. Scaffold biocompatibility with respect to biopolymer mobility and cell adhesion dynamics : [presented at 10th EBSA European Biophysics Congress, Dresden, Germany, 18-22 July, 2015]. European biophysics journal, ISSN 0175-7571, 2015, vol. 44, suppl. 1, str. S134. [COBISS.SI-ID 28786983], [JCR, SNIP]

11. PODLIPEC, Rok. Scaffold biocompatibility with respect to biopolymer mobility and cell adhesion dynamics. V, MALIČEV, Elvira (ur.), FRÖHLICH, Mirjam (ur.), RADOSAVLJEVIČ, Damjan (ur.). *Regenerative medicine, achievements and perspectives, [uredniki Elvira Maličev, Mirjam Fröhlich, Damjan Radosavljević].* Ljubljana, DCTIS, Društvo za celično in tkivno inženirstvo, 2015, str. 32. [COBISS.SI-ID 28542759]

12. GORGIEVA, Selestina, JURAŠIN, Darija, PODLIPEC, Rok, ŠTRANCAR, Janez, KOKOL, Vanja. Step towards understanding the cell-scaffold interactions. V, 25th European Conference on Biomaterials, ESB 2013, XXV Symposium of the European Society for Biomaterials, 8-12 September 2013, Madrid (Spain). *From the design to the application of biomaterials, book of abstracts*, 2013, 1 str. [COBISS.SI-ID 17166614]

13. KOKLIČ, Tilen, PODLIPEC, Rok, GARVAS, Maja, ORTHMANN, Andrea, ŠENTJURC, Marjeta, ZEISIG, Reiner, ŠTRANCAR, Janez. Perifosine containing liposomal nanocarriers - yet another drug delivery system across barrier forming cells. V, 7th Christmas Biophysics Workshop, XBW 2012, 17.-18.12.2012, Riegersburg, Austria. *Book of abstracts*. 2012, str. 18. [COBISS.SI-ID 26363175]

14. KAISERSBERGER VINCEK, Maja, GORGIEVA, Selestina, PODLIPEC, Rok, ŠTRANCAR, Janez, KOKOL, Vanja. Specific functionalization of protein materials (wool and gelatin) with [epsilon]-poly-L-lysine ([epsilon]-PL) for tunable antimicrobial properties. V, II International Conference on Antimicrobial Research (ICAR2012), Lisbon, Portugal, 21-23 November 2012. *Book of abstracts*. Formatex, 2012, str. 522. [COBISS.SI-ID 16468758]

15. ARSOV, Zoran, URBANČIČ, Iztok, GARVAS, Maja, BIGLINO, Daniele, LJUBETIČ, Ajasja, PODLIPEC, Rok, KOKLIČ, Tilen, ŠTRANCAR, Janez. Confocal fluorescence microspectroscopy , powerful biophysical tool to resolve molecular environment. V, Regional Biophysics Conference 2012, Kladovo-Beograd, Serbia, September 03-07, 2012. ZAKRZEWSKA, Joanna (ur.), ŽIVIĆ, Miroslav (ur.), ANDJUS, Pavle (ur.). *Book of abstracts*. Beograd, Društvo biofizičara Srbije, 2012, str. 41. [COBISS.SI-ID 26065191]

16. KOKLIČ, Tilen, ORTHMANN, Andrea, PODLIPEC, Rok, ŠENTJURC, Marjeta, ŠTRANCAR, Janez, ZEISIG, Reiner. Effect of perifosine on liposome membrane characteristics, transcytosis and liposome contents leakage. V, Regional Biophysics Conference 2012, Kladovo-Beograd, Serbia, September 03-07, 2012. ZAKRZEWSKA, Joanna (ur.), ŽIVIĆ, Miroslav (ur.), ANDJUS, Pavle (ur.). *Book of abstracts*. Beograd, Društvo biofizičara Srbije, 2012, str. 45. [COBISS.SI-ID 26065447]

17. PODLIPEC, Rok, KOKLIČ, Tilen, ŠTRANCAR, Janez, ŠENTJURC, Marjeta. Influence of cancerostatic perifosine on membrane fluidity of different cell lines. V, Regional Biophysics Conference 2012, Kladovo-Beograd, Serbia, September 03-07, 2012. ZAKRZEWSKA, Joanna (ur.), ŽIVIĆ, Miroslav (ur.), ANDJUS, Pavle (ur.). *Book of abstracts*. Beograd, Društvo biofizičara Srbije, 2012, str. 91. [COBISS.SI-ID 26065703]

18. KOKLIČ, Tilen, PODLIPEC, Rok, GARVAS, Maja, ORTHMANN, Andrea, ŠENTJURC, Marjeta, ZEISIG, Reiner, ŠTRANCAR, Janez. Perifosine containing liposomal nano carriers - yet another drug

delivery system across barrier forming cells. V, SLONANO 2012, 24-26 October 2012, Ljubljana, Slovenia. MIHAILOVIĆ, Dragan (ur.), et al. *Book of abstracts*. Ljubljana, Institut Jožef Stefan, 2012, str. 14. [COBISS.SI-ID 26409767]

19. KAISERSBERGER VINCEK, Maja, GORGIEVA, Selestina, PODLIPEC, Rok, ŠTRANCAR, Janez, KOKOL, Vanja. Functionalization of protein polymers with antimicrobial peptide (AMPs) for tuneable antimicrobial properties. V, *E-MRS 2012 fall meeting, September 17-21, Warsaw University of Technology.* Strasbourg, European Materials Research Society, 2012, [COBISS.SI-ID 16271126]

20. PODLIPEC, Rok, JURAŠIN, Darija, GORGIEVA, Selestina, KOKOL, Vanja, ŠTRANCAR, Janez. The study and experimental approaches of cell-scaffold contact. V, *E-MRS 2012 fall meeting, September 17-21, Warsaw University of Technology.* Strasbourg, European Materials Research Society, 2012, [COBISS.SI-ID 16271894]

21. KOKLIČ, Tilen, PODLIPEC, Rok, MRAVLJAK, Janez, ŠENTJURC, Marjeta, ZEISIG, Reiner. Interaction of alkylphospholipid liposomes with breast cancer cells, [presented at 8th EBSA European Biophysics Congress, August 23rd-27th 2011, Budapest, Hungary]. *European biophysics journal*, ISSN 0175-75710175-7571, 2011, vol. 40, suppl. 1, str. S79. [COBISS.SI-ID 24994855]

22. MRAVLJAK, Janez, PODLIPEC, Rok, KOKLIČ, Tilen, PEČAR, Slavko, ŠENTJURC, Marjeta. Interaction of spin-labeled derivatives of a cancerostatic alkylphospholipid, perifosine, with model and cell membranes. V, VIIIth International Workshop on EPR(ESR) in Biology and Medicine, October 4-7, 2010, Krakow, Poland. *Book ob abstracts*. [S. l., s. n.], 2010, str. 43. [COBISS.SI-ID 24379431]

23. PODLIPEC, Rok, ŠENTJURC, Marjeta, ZEISIG, Reiner, KOKLIČ, Tilen. Interaction of liposome carriers on epithelial cells as a model of drug transport across the blood brain barier. V, MIHAILOVIĆ, Dragan (ur.), DOMINKO, Robert (ur.), VILFAN, Mojca (ur.). *Book of abstracts , SLONANO 2009, 19-21 October 2009, Ljubljana.* Ljubljana, National Institute of Chemistry, 2009, str. 69. [COBISS.SI-ID 23043111]

1.16 Independent scientific component part or a chapter in a monograph

24. KOKLIČ, Tilen, PODLIPEC, Rok, MRAVLJAK, Janez, GARVAS, Maja, ŠENTJURC, Marjeta, ZEISIG, Reiner. Interaction of alkylphospholipid formulations with breast cancer cells in the context of anticancer drug development. V, GUNDUZ, Mehmet (ur.), GUNDUZ, Esra (ur.). *Breast cancer - focusing tumor microenvironment, stem cells and metastasis*. Rijeka, InTech, 2011, str. 361-384, doi, 10.5772/20584. [COBISS.SI-ID 3177329]

MONOGRAPHS AND OTHER COMPLETED WORKS

2.11 Undergraduate thesis

25. PODLIPEC, Rok. *Študij transporta alkilfosfolipidov skozi membrano malignih celic z elektronsko paramagnetno resonanco, diplomsko delo*. Ljubljana, [R. Podlipec], 2011. 69 str., graf. prikazi. [COBISS.SI-ID 2340964]

UNIVERZA V MARIBORU

Fakulteta za naravoslovje in matematiko

IZJAVA DOKTORSKEGA KANDIDATA

Podpisani **Rok Podlipec**, vpisna številka **N3000645**

izjavljam,

da je doktorska disertacija z naslovom **The analysis of cell-biomaterial interaction by advanced experimental techniques as the basis for biocompatibility studies of polymers**

in slovenskim prevodom **Raziskave interakcij med celicami in biopolimernimi materiali z naprednimi eksperimentalnimi metodami kot osnova za študij biokompatibilnosti polimerov**

- rezultat lastnega raziskovalnega dela,
- da predložena disertacija v celoti ali v delih ni bila predložena za pridobitev kakršnekoli izobrazbe po študijskem programu druge fakultete ali universe,
- da so rezultati korektno navedeni in
- da nisem kršil avtorskih pravic in intelektualne lastnine drugih.

Podpis dotorskega kandidata

V Ljubljani, dne 8.9.2015